

UNIVERSITÉ DU QUÉBEC

**ÉTUDE DU COUPLAGE CIRCULATION-PRODUCTION  
PLANCTONIQUE À MÉSO-ÉCHELLE DANS LE GOLFE DU SAINT-  
LAURENT (CANADA) VIA UNE APPROCHE PAR MODÉLISATION  
TRIDIMENSIONNELLE**

THÈSE

PRÉSENTÉE À

L'UNIVERSITÉ DU QUÉBEC À RIMOUSKI

comme exigence partielle

du programme de doctorat en océanographie

PAR

VINCENT LE FOUEST

Juin 2005

UNIVERSITÉ DU QUÉBEC À RIMOUSKI  
Service de la bibliothèque

Avertissement

La diffusion de ce mémoire ou de cette thèse se fait dans le respect des droits de son auteur, qui a signé le formulaire « *Autorisation de reproduire et de diffuser un rapport, un mémoire ou une thèse* ». En signant ce formulaire, l'auteur concède à l'Université du Québec à Rimouski une licence non exclusive d'utilisation et de publication de la totalité ou d'une partie importante de son travail de recherche pour des fins pédagogiques et non commerciales. Plus précisément, l'auteur autorise l'Université du Québec à Rimouski à reproduire, diffuser, prêter, distribuer ou vendre des copies de son travail de recherche à des fins non commerciales sur quelque support que ce soit, y compris l'Internet. Cette licence et cette autorisation n'entraînent pas une renonciation de la part de l'auteur à ses droits moraux ni à ses droits de propriété intellectuelle. Sauf entente contraire, l'auteur conserve la liberté de diffuser et de commercialiser ou non ce travail dont il possède un exemplaire.

## REMERCIEMENTS

Je tiens à remercier spécialement les personnes suivantes qui ont contribué au développement de ma thèse de doctorat :

Mon directeur de recherche, le Dr Bruno Zakardjian, pour sa disponibilité permanente et ses conseils constructifs, et dont l'entrain et la curiosité scientifique ont été très appréciés.

Mes co-directeurs de recherche, le Dr François Saucier et le Dr Michel Starr pour leur co-supervision et leurs précieux commentaires.

Le Dr Bjorn Sundby, président du jury d'évaluation et le Dr Jacques C. J. Nihoul, examinateur externe de ce mémoire pour avoir accepté de consacrer un peu de leur précieux temps à évaluer ce travail.

Les membres de mon comité de thèse, le Dr Michel Gosselin et le Dr Louis Prieur pour leur suivi attentif du cheminement de la thèse.

Le personnel administratif de l'ISMER.

Je remercie également l'ensemble du groupe de modélisation de l'ISMER et les nombreux stagiaires d'été. Une pensée spéciale aux personnes des premiers instants, James Caveen, François Roy et Simon Senneville.

Suzanne Roy, Stéphane Maritorenna, Servet Çizmeli, Mehmet Yayla pour leurs avis critiques et au combien constructifs sur les travaux menés durant cette thèse.

Pierre Larouche et André Gosselin pour l'accès aux données satellites de température.

Youssef Djibril Soubaneh et Patrick Poulin, les habitués du dimanche.

Une dernière pensée à un ami parti trop tôt, Guy-Juslin Bibimbou.

Et bien sûr, j'aimerais remercier spécialement et dédier cette thèse à mon épouse Maria Lorena Longhi pour son soutien moral et son aide tout au long de ce parcours. Mil gracias.

## RÉSUMÉ

La circulation à méso-échelle joue un rôle majeur sur la distribution, la structure et la productivité des écosystèmes planctoniques tant en milieu ouvert que côtier. Le golfe du Saint-Laurent est une mer côtière sub-arctique qui est caractérisée par des conditions hydrodynamiques hautement variables. Des processus à méso-échelle tels que des fronts, des tourbillons, des méandres et des résurgences côtières y génèrent une hétérogénéité spatiale de la productivité marine. Améliorer notre compréhension des liens entre la biologie et l'environnement physique est donc nécessaire afin d'évaluer les effets de la variabilité du climat sur la production planctonique du golfe.

Dans cette optique, l'objectif général de la thèse était d'étudier l'influence de la circulation à méso-échelle sur la dynamique de la production planctonique du golfe du Saint-Laurent. A cette fin, un modèle tridimensionnel (3-D) haute résolution couplé physique-biologie a été développé pour la première fois pour les eaux du Saint-Laurent. Le modèle d'écosystème planctonique est modérément complexe et prend en considération la compétition entre les chaînes trophiques herbivore et microbienne, caractéristiques du cycle de production planctonique du golfe. Le modèle biologique est couplé à un modèle prognostique couplé circulation-glace de mer gouverné par des forçages océaniques, atmosphériques et hydrologiques réalistes.

Afin de répondre à l'objectif général, trois objectifs spécifiques ont été fixés. Le premier objectif spécifique (chapitre II) consistait à vérifier la robustesse écologique du modèle couplé physique-biologie à l'échelle régionale et à décrire qualitativement et

quantitativement la variabilité sous-régionale du cycle saisonnier planctonique en réponse aux régimes hydrodynamiques variés qui caractérisent le système. Un cycle planctonique cohérent avec les observations rapportées dans le golfe a été produit par le modèle : (1) une floraison printanière dominée par le phytoplancton de grande taille, (2) la formation en été d'un maximum profond de chlorophylle *a* et une production primaire principalement régénérée, et (3) une augmentation de la proportion de la production nouvelle associée aux apports de nitrate dus au mélange automnal. La dynamique de la glace de mer est responsable de la variabilité sous-régionale du déclenchement de la floraison de printemps. Les champs de nitrate et de chlorophylle *a* simulés ont été validés avec succès à partir de mesures *in situ* coïncidentes dans le temps et l'espace obtenues dans le cadre du Programme de Monitoring Zonal Atlantique (PMZA). Le modèle a également mis en évidence le rôle majeur de l'activité à méso-échelle sur la production primaire annuelle qui montre une forte hétérogénéité spatiale ( $40-150 \text{ g C m}^{-2} \text{ an}^{-1}$ ). Il est apparu clairement que le golfe ne pouvait être considéré comme un système homogène. L'intensité de la floraison printanière étant similaire entre les sous-régions du GSL, la variabilité spatiale de la production primaire annuelle est due à des différences dans la production estivale associées à des conditions hydrodynamiques différentes. Le modèle a mis en lumière des zones de plus forte production associées à une plus forte activité de la chaîne trophique herbivore. Ce résultat suggère qu'en dehors de la période de floraison printanière, la production primaire soit localement du même ordre de grandeur que durant le printemps. En ce sens, la variabilité synoptique se compare en importance à la variabilité saisonnière.

Compte tenu de la limitation imposée par les observations *in situ* en terme de validation spatiale, le second objectif spécifique (chapitre III) visait à valider les solutions du modèle couplé à l'échelle régionale et synoptique à l'aide de données satellites de température de surface (AVHRR) et de couleur de l'eau (SeaWiFS). Une bonne correspondance qualitative et quantitative a été observée entre les valeurs de température de surface simulées et dérivées du radiomètre AVHRR. Une relation inversement linéaire reliant l'atténuation de la lumière due au matériel non-chlorophyllien à la salinité du modèle a été incorporée à la formulation du champ de lumière permettant ainsi de simuler explicitement la turbidité. La comparaison des valeurs de chlorophylle *a* simulées et dérivées des mesures du senseur SeaWiFS avec les valeurs mesurées *in situ* coïncidentes dans le temps et l'espace a révélé une surestimation substantielle par le senseur dans les eaux estuariennes, suggérant une contamination de ces valeurs par des composés optiques actifs (principalement de la matière organique colorée) présents dans l'eau. En revanche, les patrons spatiaux dérivés du senseur SeaWiFS ont montré une bonne correspondance avec les champs simulés de turbidité et ont ainsi permis de valider la variabilité saisonnière et synoptique de la circulation estuarienne.

Au regard de ces résultats, il est apparu important de quantifier l'impact de la turbidité associée au panache estuarien sur la dynamique planctonique de l'estuaire et du golfe, constituant ainsi le troisième et dernier objectif spécifique de la thèse (chapitre IV). La nouvelle formulation reliant le coefficient d'atténuation diffuse due au matériel non-chlorophyllien à la salinité du modèle a permis de mieux simuler le déclenchement de la floraison printanière dans l'estuaire, où l'influence de l'écoulement des eaux douces est la

plus marquée. De plus, les concentrations de nitrate simulées ont montré un meilleur accord avec les mesures *in situ* à deux stations fixes du nord-ouest du golfe fortement affectées par l'écoulement des eaux estuariennes. Les flux latéraux de nitrate dans la couche de surface ont été augmentés dans tout l'ouest du golfe pour se rapprocher des estimations rapportées dans la littérature, mais la production primaire dans les sous-régions influencées par le panache estuarien a été réduite, soulevant ainsi un paradoxe.

En conclusion, le modèle 3-D couplé physique-biologie a mis en lumière une variabilité à méso-échelle importante dans le golfe du Saint-Laurent qui devrait faire l'objet d'une attention particulière dans une perspective de prédire et d'évaluer les effets des changements climatiques sur la productivité du système. Des améliorations devront être apportées au modèle dans son aspect biogéochimique, avec une emphase particulière concernant la modélisation de la dynamique du phytoplancton dans les eaux estuariennes plus turbides dont l'importance au niveau régional s'avère majeure.

---

## TABLE DES MATIÈRES

REMERCIEMENTS.....	ii
RÉSUMÉ.....	iv
TABLE DES MATIÈRES.....	viii
LISTE DES FIGURES.....	x
LISTE DES TABLEAUX.....	xix
I. INTRODUCTION GÉNÉRALE.....	1
II. SEASONAL VERSUS SYNOPTIC VARIABILITY IN PLANKTONIC PRODUCTION IN A HIGH-LATITUDE MARGINAL SEA: THE GULF OF ST. LAWRENCE (CANADA).....	10
ABSTRACT.....	11
INTRODUCTION.....	12
MODEL FORMULATION.....	15
1. <i>The 3-D regional circulation model</i> .....	15
2. <i>The planktonic ecosystem model</i> .....	17
3. <i>Coupling with the 3-D regional circulation model</i> .....	19
RESULTS.....	25
1. <i>Mean seasonal biomass and production cycle</i> .....	25
2. <i>Sub-regional differences in planktonic production</i> .....	31
DISCUSSION.....	51
CONCLUSIONS.....	62
APPENDIX. PLANKTONIC ECOSYSTEM MODEL DESCRIPTION.....	64
III. APPLICATION OF REMOTELY SENSED SEA COLOR AND TEMPERATURE DATA FOR MESOSCALE AND REGIONAL VALIDATION OF A 3-D HIGH-RESOLUTION	

BIOLOGICAL-PHYSICAL COUPLED MODEL OF THE GULF OF ST. LAWRENCE (CANADA): THE CHALLENGE OF INLAND WATERS.....	70
ABSTRACT.....	71
INTRODUCTION.....	72
METHODS.....	75
1. <i>The 3-D physical-planktonic ecosystem model</i> .....	75
2. <i>Remotely sensed and in situ data</i> .....	78
RESULTS AND DISCUSSION.....	85
1. <i>Simulated and AVHRR-derived SST</i> .....	84
2. <i>Turbidity, simulated and SeaWiFS-derived surface Chl a</i> .....	97
3. <i>The CDOM hypothesis</i> .....	105
4. <i>Tracking the estuarine circulation and the associated mesoscale activity</i> .....	107
CONCLUSIONS.....	111
IV. THE IMPACT OF FRESHWATER-ASSOCIATED TURBIDITY ON PHYTOPLANKTON IN A HIGHLY DYNAMIC SHELF SEA: A MODELLING STUDY IN THE GULF OF ST. LAWRENCE (CANADA).....	114
ABSTRACT.....	115
INTRODUCTION.....	116
THE COUPLED MODEL.....	119
RESULTS.....	122
DISCUSSION.....	138
CONCLUSIONS.....	144
V. CONCLUSION GÉNÉRALE.....	146
VI. RÉFÉRENCES.....	155

## LISTE DES FIGURES

- Figure II-1. Map of the Estuary and Gulf of St. Lawrence. Bold lines delimit the numerical domain. Boxes indicate the studied subregions: Lower Estuary of St. Lawrence (LSLE), northwestern Gulf of St. Lawrence (NWG), Unguedo Strait (USt), Magdalen Shallow (MS), southern Laurentian Channel (SLC), northeastern Gulf of St. Lawrence (NEG) and Jacques Cartier Strait (JCS).....16
- Figure II-2. Conceptual planktonic ecosystem model including nitrate ( $\text{NO}_3$ ), ammonium ( $\text{NH}_4$ ), large phytoplankton (LP), small phytoplankton (SP), mesozooplankton (MEZ), microzooplankton (MIZ), particulate organic nitrogen (PON) and dissolved organic nitrogen (DON). Arrows represent nitrogen fluxes between the biological components.....18
- Figure II-3. Domain-averaged seasonal cycle of the (a) depth-integrated (0-45 m) biomass of plankton components with sea ice cover percentage, (b) depth-integrated (0-45 m) total primary production with the depth-averaged (0-45 m) f-ratio (ratio of the total new primary production over total primary production), (c) total Chl *a* and (d) nitrate. The horizontal line in panel b indicates a f-ratio of 0.5.....24

- Figure II-4. Vertical distribution of the domain-averaged concentrations of nitrate (solid line), large phytoplankton (dashed line), and small phytoplankton (dashed-dotted line) on July 15<sup>th</sup> .....27
- Figure II-5. Comparisons of modeled and observed data: (a) sampling locations in June (circles) and November (crosses) 1997; scatter plot of (b) nitrate and (c) total Chl *a*; profiles of modeled (solid line) and observed (dashed line) concentrations of (d) nitrate and (e) total Chl *a* in June and of (f) nitrate and (g) total Chl *a* in November. The bold line represents the spatially-averaged profile. The shaded area is delimited by the spatially-averaged profile  $\pm$  standard deviation (thin lines).....30
- Figure II-6. Mean seasonal cycle of total Chl *a* (integrated between 0-45 m) and sea ice cover percentage for the numerical domain and all subregions shown in Figure II-1. The shaded area is delimited by the spatially-averaged time series of total Chl *a* (bold line)  $\pm$  standard deviation (thin lines).....32
- Figure II-7. Regional overview of the depth-integrated (0-45 m) and yearly-cumulated total primary production with depth- and yearly-averaged (0-45 m) currents, depth- and yearly-averaged (0-45 m) f-ratio, depth-integrated (0-45 m) and yearly-cumulated total secondary production, and depth-integrated (0-45 m) and yearly-cumulated

fecal pellets production. Boxes on the upper left panel delimit the studied subregions.....	34
Figure II-8. May to October mean in the LSLE of sea temperature (5 m), salinity (5 m), nitrate (5 m), and depth-integrated (0-45 m) total Chl <i>a</i> . Mean currents (5 m) are overlaid in all panels.....	36
Figure II-9. Time series at a fixed station located in the upstream part of the LSLE (white box in Figure 8) of the (a) total primary production (PP), (b) total Chl <i>a</i> with the depth of the nitracline overlaid, and (c) density ( $\text{kg m}^{-3}$ ).....	37
Figure II-10. Snapshots of the depth-integrated (0-45 m) total Chl <i>a</i> ( $\text{mg m}^{-2}$ ) with depth-averaged (0-45 m) currents on May 25 <sup>th</sup> , June 25 <sup>th</sup> , July 22 <sup>nd</sup> , August 18 <sup>th</sup> , September 20 <sup>th</sup> , and October 22 <sup>nd</sup> over the LSLE, NWG and northern USt.....	40
Figure II-11. Time series at a fixed station located in the NWG (white box in Figure II-10) of the (a) total primary production (PP), (b) total Chl <i>a</i> with the depth of the nitracline overlaid, and (c) density ( $\text{kg m}^{-3}$ ). Vertical arrows at the top of each panel indicate each snapshot of Figure II-10.....	41

- Figure II-12. Snapshots of the depth-integrated (0–45 m) total Chl *a* with depth-averaged (0–45 m) currents and surface winds (bold arrows) on September 21<sup>st</sup>, September 24<sup>th</sup>, September 27<sup>th</sup>, and September 30<sup>th</sup> in the USt.....43
- Figure II-13. Time series at a fixed station located in the USt (white box in Figure II-12) of the (a) total primary production (PP), (b) surface winds, (c) total Chl *a* with the depth of the nitracline overlaid, and (d) density ( $\text{kg m}^{-3}$ ). The two vertical lines delimit the time periods (September 21<sup>st</sup> to 30<sup>th</sup>) of the upwelling events shown in Figure II-12.....44
- Figure II-14. Snapshots of the total Chl *a* (5 m) with sea temperature contours ( $^{\circ}\text{C}$ , 5 m) on September 27<sup>th</sup>, October 1<sup>st</sup>, and October 5<sup>th</sup>. A 4 days (September 27<sup>th</sup> to September 30<sup>th</sup>) SeaWiFS composite image is presented in the lower right panel.....46
- Figure II-15. Time series at a fixed station located in the NEG (white box in Figure II-14) of the (a) total primary production (PP), (b) total Chl *a* with the depth of the nitracline overlaid, (c) nitrate concentration at 25 m, (d) temperature and salinity at 25 m, and (e) net water transport across the Strait of Belle-Isle with its moving window-averaged (14 days) equivalent overlaid. The two vertical lines delimit the time periods (September 27<sup>th</sup> to October 5<sup>th</sup>) of the simulated events shown in Figure II-14.....47

Figure II-16. Vertical sections from the MS towards the Laurentian Channel illustrating the nitrate concentrations and NW-SE currents ( $\text{m s}^{-1}$ ) averaged over July-August. The dashed and solid lines represent the seaward and north-westward current, respectively. On each panel, a solid line on a map indicates the location of the transect.....49

Figure II-17. Time series of the depth-averaged (0-45 m) relative fraction of large phytoplankton (LP, bold solid line) averaged over the NWG, the NEG, and the MS. The shaded area is delimited by the mean  $\pm$  standard deviation (thin solid lines). The horizontal dashed line indicates a relative fraction of 50 %.....56

Figure III-1. Map of the Gulf of St. Lawrence and geographical appellations used in the paper. The bold lines indicate the boundaries of the 3-D coupled physical-biological model.....76

Figure III-2. Scatter plot showing the linear relationship between salinity and the attenuation coefficient due to non-chlorophyllous matter ( $k_p$ ) derived from *in situ* measurements. The linear regression gives the equation  $k_p = -0.0364 \text{ Salinity} + 1.1942$  with a correlation coefficient of  $r^2 = 0.71$ .....79

- Figure III-3. Positions of the (a) permanently moored thermometers, (b) sampling stations visited in 1998: AZMP cruises in June (squares) and November (triangles), the fixed AZMP stations (circles), and the SeaWIFS validation cruise in October-November (rhombuses).....82
- Figure III-4. Comparisons of satellite-derived fields of SST and surface Chl *a* to simulated SST (5 m), Chl *a* (depth-averaged 0-10 m), and attenuation coefficient due to non-chlorophyllous matter ( $k_p$ ) for the June 7<sup>th</sup>-11<sup>st</sup> period. The mean simulated fields of surface wind and depth-averaged (0-10 m) current are overlaid on the mean simulated SST and Chl *a* fields, respectively.....85
- Figure III-5. Same as Figure III-4 for the July 2<sup>nd</sup>-8<sup>th</sup> period.....86
- Figure III-6. Same as Figure III-5 for the August 3<sup>rd</sup>-6<sup>th</sup> period.....87
- Figure III-7. Same as Figure III-6 for the August 28<sup>th</sup>-September 2<sup>nd</sup> period.....88
- Figure III-8. Same as Figure III-7 for the October 6<sup>th</sup>-14<sup>th</sup> period.....89
- Figure III-9. Comparison of simulated SST with (a) AVHRR-derived SST and (b) *in situ* SST, and (c) comparison of *in situ* and simulated salinity. *In situ* data include measurements made in 1998 from the AZMP June and November cruises and

three fixed stations (see text). In panels (b) and (c), surface values are in red whereas deeper values are in black (the whole water column).....90

Figure III-10. Comparisons of *in situ* SST to (a) simulated SST and (b) AVHRR-derived SST.....94

Figure III-11. Time series of hourly temperature records from permanently moored thermometers (in blue) compared to simulated temperature at the corresponding layer (in red). The number of the instrument (see Figure III-3a) and the record depth appear on each panel.....96

Figure III-12. Comparison of simulated Chl *a* with (a) SeaWIFS-derived Chl *a* and (b) *in situ* Chl *a*, and (c) comparison of *in situ* and simulated nitrate. *In situ* data include the whole set of available measurements made in 1998 (AZMP June and November cruises and fixed stations, SeaWIFS validation cruise of October-November, see text). In panels (b) and (c), surface values are in red whereas deeper values are in black (above 50 m for Chl *a*) the whole water column for nitrate).....98

Figure III-13. Comparison of (a) simulated Chl *a* and (b) SeaWIFS-derived Chl *a* to *in situ* Chl *a* for the limited set of match-up points between SeaWIFS and *in situ* data.....102

- Figure IV-1. Annual mean of the depth-averaged (0-10 m) salinity (with currents overlaid) and  $k_p$  for the run using a variable  $k_p$ .....123
- Figure IV-2. Annual mean of the depth of the euphotic zone for the run using a fixed or a variable  $k_p$ .....123
- Figure IV-3. Yearly- and depth-integrated (0-45 m) new and regenerated primary production (PP) for the run using a fixed or a variable  $k_p$ .....125
- Figure IV-4. Annual mean of the depth-averaged (0-10 m) nitrate and ammonium, and depth-integrated (0-10 m) total Chl  $a$  for the run using a fixed or a variable  $k_p$ .....126
- Figure IV-5. Annual mean of the depth-averaged (0-10 m) growth rates of large and small phytoplankton (LP and SP, respectively) for the run using a fixed or a variable  $k_p$ . Because the two phytoplankton groups show the same response to light, only one panel is presented for both size classes.....127
- Figure IV-6. Mean seasonal cycle of total Chl  $a$  (integrated between 0-45 m) and sea ice concentration for the numerical domain as a whole and subregions of the GSL

cited in the text. The black and red lines correspond to the run using a fixed and variable  $k_p$ , respectively. ....129

Figure IV-7. Time series of the vertical distribution  $k_p$  ( $m^{-1}$ ). The nutricline from the run using a fixed  $k_p$  (black dashed line) and a variable  $k_p$  (black line) are overlaid.....131

Figure IV-8. Map of the Estuary and Gulf of St. Lawrence. Acronyms indicate the subregions cited in the text. The bold lines are the open boundaries of the coupled model. The thin lines indicate the transects used for nitrogen fluxes estimations. Circles show the location of the Gaspé (nearshore) and Anticosti (offshore) stations.....133

Figure IV-9. Ratios between simulated depth-integrated (0-30 m) *vs in situ* depth-integrated (0-30 m) nitrate concentrations at the a) Gaspé and b) Anticosti stations. The black and red circles correspond to the run using a fixed and variable  $k_p$ , respectively; time series of the c) depth-integrated (0-30 m) nitrate flux from the LSLE with a fixed  $k_p$  (in black) and variable  $k_p$  (in red) and d) depth-averaged (0-30 m)  $k_p$  at the Gaspé (black line) and Anticosti (black dashed line) stations.....136

## LISTE DES TABLEAUX

Table II-1. State variables and partial equations.....	20
Table II-2. Parameters used in the ecosystem model.....	21
Table III-1. Time periods and number of images used to build the AVHRR and SeaWiFS composites.....	81
Table III-2. Root mean square (RMS, °C) error and mean relative difference (MRD, %) calculated between the AVHRR-derived and simulated SST (n=50237). Coincident points for each time period are shown in parentheses.....	92
Table III-3. Root mean square (RMS) error and mean relative difference (MRD, %) calculated between the <i>in situ</i> (bottle measurements) and simulated temperature, salinity, nitrate and Chl <i>a</i> . Numbers of sampling are shown in parentheses.....	92
Table III-4. Root mean square (RMS, °C) error and mean relative difference (MRD, %) calculated between the <i>in situ</i> (moored thermometers) and simulated or AVHRR-derived SST (n = 42). Coincident points for each time period are shown in parentheses.....	95

Table III-5. Root mean square (RMS, mg Chl <i>a</i> m <sup>-3</sup> ) error and mean relative difference (MRD, %) calculated between the SeaWIFS-derived and simulated Chl <i>a</i> concentrations (n=48361). Coincident points for each time period are shown in parentheses.....	99
Table III-6. Root mean square (RMS, mg Chl <i>a</i> m <sup>-3</sup> ) error and mean relative difference (MRD, %) calculated between the <i>in situ</i> and simulated or SeaWIFS-derived Chl <i>a</i> concentrations for the GSL subregions (n=35). The number of match-up points for each subregion is displayed in parentheses.....	103
Table IV-1. Mean annual primary production of the GSL and its subregions (g C m <sup>-2</sup> yr <sup>-1</sup> ).....	130
Table IV-2. Ratio of the yearly- and depth-integrated (0–30 m) nitrate flux over the yearly- and depth-integrated (0–30 m) organic nitrogen flux.....	135
Table IV-3. Mean nitrate flux (0-30 m) in summer (in 10mol s <sup>-1</sup> ). Percentages in parentheses indicate the bias between the fluxes simulated using a fixed or a salinity-dependant $k_p$ and those provided by <i>Savenkoff et al.</i> [2001].....	139

## I. INTRODUCTION GÉNÉRALE

De par sa proximité et sa dynamique, le golfe du Saint-Laurent (GSL) est un bassin expérimental unique pour l'étude des interactions physique/biologie à méso-échelle. Une des plus grandes mers intérieures semi-fermée, le GSL fait la connexion entre les Grands Lacs, le fleuve Saint-Laurent et l'océan Atlantique Nord. Les eaux de surface estuariennes sont évacuées du GSL par le détroit de Cabot, alors que les eaux salées de l'océan Atlantique et de la mer du Labrador y pénètrent principalement par les détroits de Cabot et de Belle-Isle, respectivement. Les variations saisonnières des débits d'eau douce du fleuve Saint-Laurent et de la rivière Saguenay contribuent grandement au patron de circulation des eaux de surface estuariennes vers le GSL. La couverture saisonnière de glace de mer associée au climat sub-arctique s'étend de janvier à avril et atteint la limite des glaces de mer la plus au sud de l'hémisphère Nord. Les marées sont modérées à fortes et la variabilité du régime des vents très synoptique. Ces forçages hydrologiques, océaniques et atmosphériques, associés aux dimensions du golfe (226000 km<sup>2</sup>, 150 m de profondeur moyenne), génèrent une circulation complexe où les tourbillons, les résurgences côtières et les zones frontales se superposent à une circulation de type estuarienne [Koutitonsky et Budgen, 1991; Fuentes-Yaco et al., 1995; 1996; 1997ab; Saucier et al., 2003]. Cette dynamique à méso-échelle pourrait jouer un rôle important dans la dynamique de l'écosystème planctonique du Saint-Laurent. de Lafontaine et al. [1991] soulignent une certaine hétérogénéité spatiale dans le GSL illustrée par des différences dans le cycle saisonnier, la composition spécifique et la structure de taille du phytoplancton et du

zooplancton, et probablement par des réseaux trophiques différents. Les images satellites de température de surface (<http://www.osl.gc.ca/teledetection/fr/index.html>) et de couleur de l'eau [Fuentes-Yaco *et al.*, 1995; 1997a] suggèrent une forte variabilité hydrodynamique à méso-échelle dans le GSL, particulièrement au printemps et en automne, soit pendant les périodes de plus forte production. Des observations récentes confirment que la variabilité interannuelle des propriétés des masses d'eau du GSL [Saucier *et al.*, 2003], de la biomasse planctonique dans l'estuaire maritime du Saint-Laurent [EMSL; Starr *et Harvey*, 2000; Starr *et al.*, 2001], du recrutement des stocks de poisson [Runge *et al.*, 1999], des patrons d'agrégations du krill et des baleines à la tête du chenal laurentien [Simard *et Lavoie*, 1999; Lavoie *et al.*, 2000] est fortement liée à l'influence du climat et des apports d'eau douce sur les processus de mélange et la circulation.

Il apparaît nécessaire d'engager un plus grand nombre d'études afin de comprendre, quantifier et, éventuellement prédire, les effets de la variabilité des processus physiques sur la production planctonique marine. C'est de l'échelle locale (1-10 km) à moyenne (10–plusieurs centaines de km) que les interactions directes entre la dynamique des écoulements océaniques et la production des communautés planctoniques sont les plus importantes [Garçon *et al.*, 2001; Lévy *et al.*, 2001]. En effet, la dynamique de ces écoulements océaniques d'échelle locale à moyenne obéit à des échelles de temps caractéristiques (du jour à quelques mois), proches de celles des processus biologiques impliqués dans la production planctonique (de la journée pour la production primaire à quelques semaines pour la production secondaire). Ces structures de méso-échelle constituent une fraction importante de l'énergie cinétique des océans [Le Traon, 1991] et se singularisent par leur

dynamique dans l'espace et dans le temps. L'activité biogéochimique à l'échelle de ces structures est en étroite relation avec cet aspect dynamique. Les structures de méso-échelle sont impliquées dans l'enrichissement de la couche de surface en sels nutritifs *via* un transport horizontal [*Williams et Follows*, 1998] et vertical [*Martin et Richards*, 2001]. *McGillicuddy et al.* [1998] suggèrent que le déséquilibre entre les estimations de production primaire et la disponibilité en sels nutritifs dans les eaux oligotrophes de la mer des Sargasses pourrait être compensé par les apports verticaux de sels nutritifs au centre des tourbillons cycloniques de méso-échelle. Ces apports peuvent être équivalents à ceux engendrés par la convection hivernale de la colonne d'eau [*Siegel et al.*, 1999]. La dynamique de l'écosystème planctonique pélagique en zone frontale est également fortement liée aux processus de résurgence et de subduction des masses d'eau. Ces mouvements verticaux peuvent contribuer à augmenter la production primaire dans la zone euphotique tout en générant une hétérogénéité spatiale de cette production et de la biomasse phytoplanctonique [*Spall et Richards*, 2000] qui peuvent être découplés à l'échelle locale [*Zakardjian et Prieur*, 1998]. La plus forte production générée par cette dynamique frontale modifie la relation taille/abondance des cellules phytoplanctoniques et donc la structure trophique des communautés [*Rodríguez et al.*, 2001]. La variabilité de la structure et de la productivité de l'écosystème planctonique en zone frontale peut mener à des fluctuations de l'exportation de carbone vers les couches profondes [*Claustre et al.*, 1994; *Peinert et Miquel*, 1994; *Rodríguez et al.*, 2001]. Les flux de carbone sont donc fortement liés à la dynamique de méso-échelle. L'impact de cette dynamique sur la biogéochimie de la colonne d'eau est local mais peut s'étendre à l'échelle des bassins océaniques [*Lorentz et al.*,

1993; *Claustre et al.*, 1994; *McGillicuddy*, 2001]. Cette variabilité à méso-échelle n'est pas typiquement résolue dans les modèles de circulation à l'échelle globale [*Doney et al.*, 2001] mais les modèles de circulation à plus haute résolution apportent l'évidence qu'elle est fondamentale pour l'estimation de la productivité primaire et l'exportation de matière organique [*Mahadevan et Archer*, 2000; *Doney et al.*, 2001; *Lévy et al.*, 2001; *McGillicuddy*, 2001]. L'échelle temporelle associée à ces structures de méso-échelle dans l'océan ouvert est de quelques semaines à plusieurs mois. En milieu oligotrophe, comme dans la région du Gulf Stream, l'enrichissement en nitrate de la zone euphotique lié à la cinétique de tourbillons cycloniques est un processus clé pour la productivité du système. La durée de vie des structures de méso-échelle en milieu côtier est généralement plus courte, de quelques jours à plusieurs semaines, et ces dernières répondent à des forçages fortement synoptiques. À l'échelle régionale et locale, cette activité a des implications majeures sur la distribution spatiale du phytoplancton [*Pavelson et al.*, 1999], la production primaire [*Morán et al.*, 2001] et la structure des communautés planctonique [*Ressler et Jochens*, 2003].

Dans le Saint-Laurent, les structures de méso-échelle ont été principalement documentées dans l'EMSL et dans le nord-ouest du golfe. Dans l'EMSL, le fort hydrodynamisme lié aux apports saisonniers d'eau douce du fleuve Saint-Laurent influence fortement la distribution spatiale et temporelle du phytoplancton [*Therriault et Levasseur*, 1985]. Le patron de la circulation estuarienne dans l'EMSL se caractérise par la formation d'instabilités et de tourbillons [*Gratton et al.*, 1988; *Ingram et El-Sabh*, 1990; *Mertz et Gratton*, 1990] liée aux dimensions de l'EMSL. En effet, la largeur de l'EMSL peut

atteindre 50 km soit plusieurs rayons internes de Rossby (10 km; *Mertz et al.*, 1988), échelle caractéristique des mouvements baroclines. En dépit de conditions environnementales favorables (stratification, lumière, sels nutritifs), le déclenchement de la floraison phytoplanctonique dans l'EMSL a lieu deux mois plus tard [fin juin-début juillet; *Levasseur et al.*, 1984; *Roy et al.*, 1996] que dans le GSL [avril-mai; *Sévigny et al.*, 1979], soit en période de plus faible débit fluvial [*Therriault et al.*, 1986]. La communauté phytoplanctonique est largement dominée en été par les diatomées, les flagellés étant présents tout au long de l'année quoique plus abondants en juillet et septembre [*Roy et al.*, 1996; *Levasseur et al.*, 1984; *Savenkoff et al.*, 1998]. Ce schéma est atypique comparé aux eaux côtières de même latitude. Bien que les causes de la floraison tardive dans l'EMSL ne soient pas encore bien établies, la circulation des eaux estuariennes de surface est probablement un facteur majeur agissant de concert avec d'autres facteurs environnementaux tels que le régime de mélange turbulent, la turbidité de la colonne d'eau et la sédimentation des cellules phytoplanctoniques [*Therriault et Levasseur*, 1985; *Zakardjian et al.*, 2000]. Dans le cadre du programme COUPPB (COUplage des Processus Physiques et Biogéochimiques), *Gratton et Vézina* [1994] ont mis en évidence la formation de fronts de densité transitoires (3-5 jours) dans l'axe transversal de l'EMSL liée au passage de pulses d'eau douce en provenance de l'amont de l'estuaire. *Vézina et al.* [1995] ont montré que le déclenchement de la floraison estivale au large de Rimouski coïncidait avec la formation d'un tel front. À ce forçage s'ajoute l'effet du cycle de marée vive-eau/morte-eau sur le cycle de production primaire, phénomène dont l'importance dans l'EMSL a déjà été soulignée [*Sinclair*, 1978; *Legendre et Demers*, 1985]. Le fait que les concentrations en

sels nutritifs dans l'EMSL soient généralement élevées tout au long de l'année [Levasseur et al., 1984] supporte d'autant plus l'hypothèse que le cycle de production primaire soit principalement sous le contrôle de la dynamique de la circulation de méso-échelle, du cycle de marée et de la disponibilité en lumière.

Dans le nord-ouest du golfe, les deux structures majeures de la circulation sont le courant de Gaspé et le tourbillon d'Anticosti. Le courant de Gaspé est un courant côtier barocline principalement alimenté par l'écoulement des eaux de surface estuariennes. La dynamique du courant de Gaspé montre une variabilité synoptique importante [Koutitonsky et Budgen, 1991] illustrée par le développement de méandres et de tourbillons [Sheng, 2001] et par l'écartement de la rive sud de ce courant dessalé. Le tourbillon d'Anticosti, cyclonique et quasi-permanent [El Sabh, 1976; Koutitonsky et Budgen, 1991], est séparé du courant de Gaspé par un front de densité [Tang, 1980a]. Le fort gradient de vitesse et de densité entre le tourbillon d'Anticosti et le courant de Gaspé est à l'origine d'une circulation trans-frontale [Tang, 1980a] qui constitue une connexion entre ces deux structures hydrodynamiques. Les instabilités du courant de Gaspé peuvent aussi affecter une grande partie du nord-ouest du golfe et interagir directement avec le tourbillon. Cette dynamique de la circulation affecte l'écosystème planctonique du système tourbillon d'Anticosti/courant de Gaspé. Typiquement, les concentrations estivales en sels nutritifs dans le tourbillon sont limitantes pour la croissance des diatomées et, ainsi, l'écosystème pélagique est principalement dominé au cours de l'été par les flagellés et dinoflagellés lesquels peuvent constituer plus de 80 % de la biomasse phytoplanctonique [Sévigny et al., 1979 ; de Lafontaine et al., 1991; Levasseur et al., 1992]. Au contraire, la communauté

phytoplanctonique du courant de Gaspé est généralement dominée par les diatomées bien qu'accompagnées de petits flagellés abondants [Levasseur et al., 1992]. Levasseur et al. [1992] ont rapporté un transport de la biomasse phytoplanctonique produite dans le courant de Gaspé vers le tourbillon d'Anticosti. Quand l'écoulement des eaux de surface estuariennes est important, la biomasse phytoplanctonique à la surface du courant de Gaspé semble être transportée par mélange turbulent au-delà du front et diluée dans les eaux de surface du tourbillon [Levasseur et al., 1992]. En revanche, quand l'écoulement s'atténue (fin juillet) la biomasse phytoplanctonique, constituée principalement de diatomées, semble s'accumuler dans le front et à la base du courant [Sévigny et al., 1979; Levasseur et al., 1992]. De plus, Plourde et Runge [1993] suggèrent qu'une partie de la biomasse zooplanctonique du tourbillon n'ait pas une origine locale mais estuarienne [e.g., Vézina et al., 2000]. Le tourbillon d'Anticosti n'est donc pas une structure hydrodynamique isolée mais sa dynamique est au contraire influencée par la dynamique de méso-échelle de la circulation estuarienne.

Un troisième type de structure, plus faiblement documenté, est lié aux résurgences d'eau froide régulièrement observées dans le nord du golfe, sur la Basse Côte Nord [Koutitonsky et Budgen, 1991] et à l'extrémité ouest du détroit Jacques Cartier où le mélange tidal entre les eaux intermédiaires et les eaux de surface est intense [Pingree et Griffiths, 1980]. Au sud de l'île d'Anticosti, ces résurgences d'eau côtière sont plus probablement générées par les vents de nord-ouest ou le mélange tidal [Koutitonsky et Budgen, 1991]. Les images satellites de température de surface indiquent la présence de résurgences d'eau froide dans cette zone en été comme en automne

(<http://www.osl.gc.ca/teledetection/fr/index.html>). Ce type de résurgences est généralement associé à une plus forte production primaire liée à l'apport en surface d'eau intermédiaire riche en sels nutritifs. La côte sud de l'île d'Anticosti n'ayant jamais fait l'objet de programme d'échantillonnage, aucune donnée concernant la production planctonique n'est actuellement disponible. Toutefois, des estimations de concentration de chlorophylle *a* obtenues à l'aide d'images du capteur CZCS (Coastal Zone Color Scanner) ont permis à *Fuentes-Yaco et al.* [1995; 1997ab] de mettre en évidence des épisodes de plus forte biomasse phytoplanctonique sur la rive sud de l'île d'Anticosti. Certaines images satellites de couleur de l'eau montrent des filaments riches en chlorophylle *a* qui partent de la zone de plus forte biomasse et envahissent le nord du plateau madelinien. Ces structures laissent supposer qu'une fraction de la biomasse phytoplanctonique produite dans la zone de résurgence au sud d'Anticosti pourrait être exportée *via* la circulation à méso-échelle vers le reste du GSL [*Fuentes-Yaco et al.*, 1995; 1996].

Au regard de cette revue de littérature non-exhaustive sur le couplage physique-biologie à méso-échelle, le GSL se pose comme un système complexe et riche en processus susceptibles d'influencer le cycle annuel de production planctonique. L'objectif général de la thèse est de quantifier l'effet de cette circulation à méso-échelle sur la dynamique de la production planctonique du Saint-Laurent. Pour atteindre cet objectif, le premier modèle d'écosystème planctonique couplé au modèle prognostique de circulation du GSL [e.g., *Saucier et al.*, 2003] a été développé au cours de cette thèse afin de pleinement capturer la variabilité du système. L'atout majeur de cette approche réside dans la possibilité d'atteindre la résolution temporelle, tidale à saisonnière, caractéristique des processus

hydrodynamiques du Saint-Laurent. Trois objectifs spécifiques sont fixés afin de répondre à l'objectif général. Le premier objectif spécifique (chapitre II) consiste à vérifier la robustesse écologique du modèle couplé physique-biologie à l'échelle régionale et à décrire qualitativement et quantitativement la variabilité sous-régionale du cycle saisonnier planctonique en réponse à des régimes hydrodynamiques variés qui caractérisent le système. Les observations *in situ* seules peuvent difficilement rendre compte de l'effet de la variabilité à méso-échelle sur la dynamique du phytoplancton. En revanche, les données satellites de température de surface et de couleur de l'eau y contribuent en apportant une information à haute résolution temporelle (jusqu'à quelques heures) et spatiale (jusqu'à un kilomètre). Le second objectif spécifique (chapitre III) vise ainsi à valider les solutions du modèle couplé à l'échelle régionale et synoptique à l'aide de données satellites de température de surface (advanced very high resolution radiometer) et de couleur de l'eau (Sea-viewing Wide Field-of-view Sensor). Le troisième et dernier objectif spécifique de la thèse (chapitre IV) se place dans la continuité des résultats obtenus dans le troisième chapitre, notamment en ce qui concerne l'importance des eaux turbides estuariennes dans le Saint-Laurent. Il vise à quantifier l'impact de la turbidité des eaux continentales, particulièrement du panache estuarien, sur la dynamique planctonique du GSL.

Le corps de cette thèse est constitué de trois chapitres rédigés en anglais sous forme d'articles scientifiques ainsi que d'une introduction et conclusion générale en français. Le second chapitre est publié dans la revue *Journal of Geophysical Research (Ocean)*. Le troisième chapitre est en révision après soumission à la revue *Journal of Marine Systems*. Le quatrième chapitre sera soumis à une revue internationale pour publication.

**II. SEASONAL VERSUS SYNOPTIC VARIABILITY IN  
PLANKTONIC PRODUCTION IN A HIGH-LATITUDE MARGINAL  
SEA: THE GULF OF ST. LAWRENCE (CANADA)**

## ABSTRACT

The Gulf of St. Lawrence (Canada) is a subarctic marginal sea characterized by highly variable hydrodynamic conditions that generate a spatial heterogeneity in the marine production. A better understanding of physical-biological linkages is needed to improve our ability to evaluate the effects of climate variability and change on the gulf's planktonic production. We develop a three-dimensional (3-D) eddy-permitting resolution physical-biological coupled model of plankton dynamics in the Gulf of St. Lawrence. The planktonic ecosystem model accounts for the competition between simplified herbivorous and microbial food webs that characterize bloom and post-bloom conditions, respectively, as generally observed in temperate and subarctic coastal waters. It is driven by a fully prognostic 3-D sea ice-ocean model with realistic tidal, atmospheric and hydrological forcing. The simulation shows a consistent seasonal primary production cycle, and highlights the importance of local sea ice dynamics for the timing of the vernal bloom and the strong influence of the mesoscale circulation on planktonic production patterns at subregional scales.

## INTRODUCTION

General circulation models generally predict that global climate change associated with increased greenhouse gas concentrations in the atmosphere will lead to an amplified warming in the Arctic and its adjacent seas over the next century (5-8°C in 2070; e.g., *Holland and Bitz, 2003*). Among those, the Gulf of St. Lawrence (GSL) is a large semi-enclosed sea of 226 000 km<sup>2</sup> that connects the Great Lakes and the St. Lawrence River with the North Atlantic Ocean [e.g., *Koutitonsky and Bugden, 1991*]. Runoff from the St. Lawrence watershed is the second most important source of freshwater from North America into the North Atlantic Ocean [e.g., *Bourgault and Koutitonsky, 1999*]. The GSL exhibits a subarctic climate with a seasonal sea ice cover present between January and April, and sheds the southernmost extent of sea ice in the northern hemisphere. Freshwater runoff, large to moderate tides, and highly synoptic winds drive the gulf's circulation. These physical forcing, coupled with the relatively large dimensions of the gulf (several internal Rossby deformation radii) and an average depth of 150 m, generate a complex hydrodynamics with eddies, coastal upwellings, and fronts superimposed on a mean estuarine-like circulation [e.g., *Koutitonsky and Bugden, 1991; Saucier et al., 2003*]. These hydrodynamic conditions have been shown to have a marked effect on summer primary production in the northwestern Gulf [*Levasseur et al., 1992; Fuentes-Yaco et al., 1995, 1996, 1997ab; Tremblay et al., 1997*], and are thought to generate a spatial heterogeneity in the marine production of the GSL [e.g., *de Lafontaine et al., 1991*]. *Savenkoff et al. [2001]* also suggest that the GSL can be subdivided into distinct subregions on the basis of specific

hydrodynamic regimes that affect the nutrient transport and the resulting planktonic production. Recent observations confirm that the high interannual variability in plankton biomass in the Lower Estuary [*Starr and Harvey, 2000; Starr, 2001*], the recruitment of fish stocks in the southern gulf [*Runge et al., 1999*], the aggregation of krill and whales at the head of the Laurentian Channel [*Simard and Lavoie, 1999; Lavoie et al., 2000*], and the water masses properties of the GSL [*Saucier et al., 2003*] are strongly linked to the influence of climate and freshwater inputs on the mixing and circulation processes. However, it has not yet been possible to quantify together the detailed circulation and the response of the planktonic ecosystem.

Prior to any attempt to predict the effects of global climate variability and changes on the GSL system, we must first acquire a better knowledge of the links between the physical environment and the short-term to interannual variations in planktonic production. In order to improve our capability to predict these responses, we need to develop models that reproduce the spatio-temporal variability of the primary and secondary production cycles. Modelling of planktonic production in the St. Lawrence marine system has been limited to one-dimensional (1-D) models of the carbon cycle in the northwestern [*Tian et al., 2000*] and northeastern [*Tian et al., 2001*] GSL, to a 2-D modelling study of the phytoplankton production in the Lower Estuary [*Zakardjian et al., 2000*], and to 3-D modelling of copepods population dynamics [*Zakardjian et al., 2003*]. This paper aims at describing and quantifying the circulation-planktonic production coupling in the GSL using a detailed 3-D physical-biological model. The coupled model includes both simplified herbivorous and microbial food webs typical of bloom and post-bloom conditions respectively, as generally

observed in temperate and subarctic coastal waters. It is driven by a 3-D high resolution primitive equations ocean-sea ice regional model [*Saucier et al.*, 2003] with realistic tidal, atmospheric and hydrologic forcing.

In the present paper, we focus on the ecological robustness of the coupled model performances at the regional scale and the subregional variability of the seasonal plankton cycle in response to varied hydrodynamic conditions. These first results demonstrate that the coupled model predicts realistic levels of biomass and a seasonal cycle of planktonic production dominated by the spring phytoplankton bloom, as observed in the GSL. In addition, the model generates a large synoptic and spatial variability in planktonic production in response to the buoyancy-driven circulation, tidal mixing, and wind events. As a consequence, primary production can locally be as important as during the spring bloom.

## MODEL FORMULATION

### 1. *The 3-D regional circulation model*

A detailed description of the deterministic sea ice-ocean coupled model is presented in *Saucier et al.* [2003], and the characteristics are briefly reviewed here. The ocean model is governed by the shallow water equations solved by a finite difference scheme. It incorporates a level 2.5 turbulent kinetic energy equation [*Mellor and Yamada*, 1974, 1982] and diagnostic master length scales. A thermodynamic and dynamic sea ice model [*Semtner*, 1976; *Flato*, 1993] is coupled with the ocean model. Bulk aerodynamic exchange formulas govern the heat and momentum fluxes between the ocean, sea ice and atmosphere. The model domain covers the Estuary and the Gulf of St. Lawrence and is delimited by three open boundaries at the Cabot Strait, the Strait of Belle-Isle, and the upper limit of the tidal influence near Montreal (Figure II-1). The grid resolution is 5 km on the horizontal and ranges from 5 to 20 m in the vertical, with free surface and bottom layers adjusted to topography. The model is fully deterministic and tracer conserving [e.g., *Saucier et al.*, 2003], driven by a detailed atmospheric forcing (three-hourly winds, light, precipitation), daily river runoff data from the St. Lawrence river and the 28 most important tributaries, hourly water levels (co-oscillating tides) and monthly mean temperature and salinity profiles at the Strait of Belle-Isle and Cabot Strait. The model accounts for the variations of sea ice, tides, momentum, heat and salt fluxes, and river discharges with a time step of 300 s and reproduces the high frequency to interannual variations of the circulation, water mass properties, and sea ice cover. Simulations for 1996-1997 [*Saucier et al.*, 2003] and recently

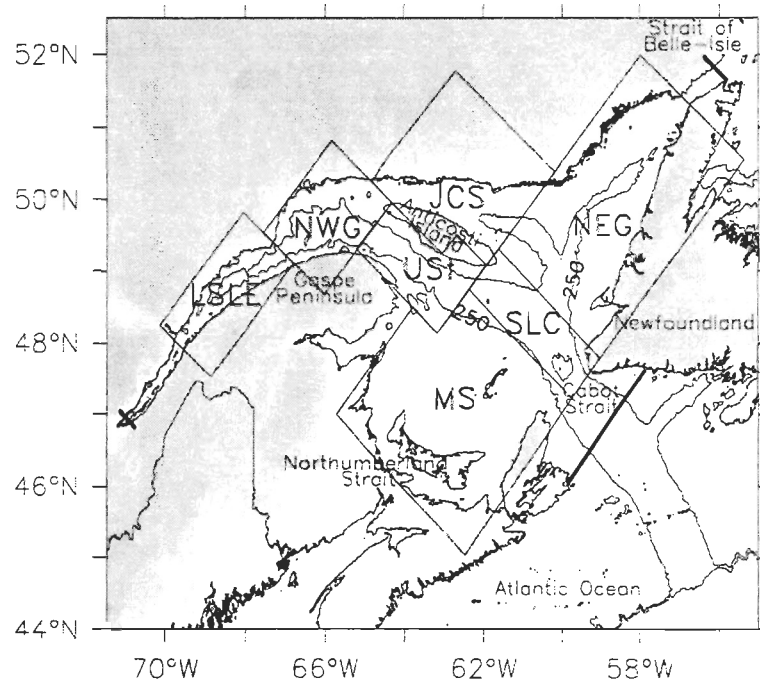


**Figure II-1. Map of the Estuary and Gulf of St. Lawrence. Bold lines delimit the numerical domain. Boxes indicate the studied subregions: Lower Estuary of St. Lawrence (LSLE), northwestern Gulf of St. Lawrence (NWG), Unguedo Strait (USt), Magdalen Shallow (MS), southern Laurentian Channel (SLC), northeastern Gulf of St. Lawrence (NEG) and Jacques Cartier Strait (JCS).**

through 2003 [Saucier *et al.*, 2005, in prep.] have been successfully compared to temperature and salinity data, the sea ice cover, water levels, and past analyses of transport in the Lower Estuary and GSL. In particular, the model reproduces the main well-known circulation features and their seasonal variations. Those include the year-round cyclonic gyre over the northwestern GSL known as the Anticosti Gyre, the Gaspé Current, an unstable buoyancy-driven baroclinic coastal jet, and the southeastward outflow through western Cabot Strait.

## 2. *The planktonic ecosystem model*

The planktonic ecosystem model (Figure II-2) was developed in a moderately complex way in order to limit the number of transfer functions and parameters, and to allow an easier interpretation of the biological response to the high frequency to seasonal variations of environmental conditions generated by the physical model. Primary producers are size-fractionated into large ( $>5 \mu\text{m}$ ) and small ( $<5 \mu\text{m}$ ) phytoplankton (LP and SP, respectively) both growing on nitrate ( $\text{NO}_3$ ) and ammonium ( $\text{NH}_4$ ). Similarly, the secondary producers are divided in mesozooplankton (200-2000  $\mu\text{m}$ , MEZ) and microzooplankton (20-200  $\mu\text{m}$ , MIZ). Two detrital compartments close the cycling of nitrogen, namely particulate and dissolved organic nitrogen (PON and DON, respectively). A close coupling between small phytoplankton and microzooplankton dynamics, autochthonous nitrogen release and DON ammonification is assumed to represent the dynamic of the microbial food web. State variables and partial differential equations are listed in Table II-1 and detailed in the Appendix, and parameters definition and values are

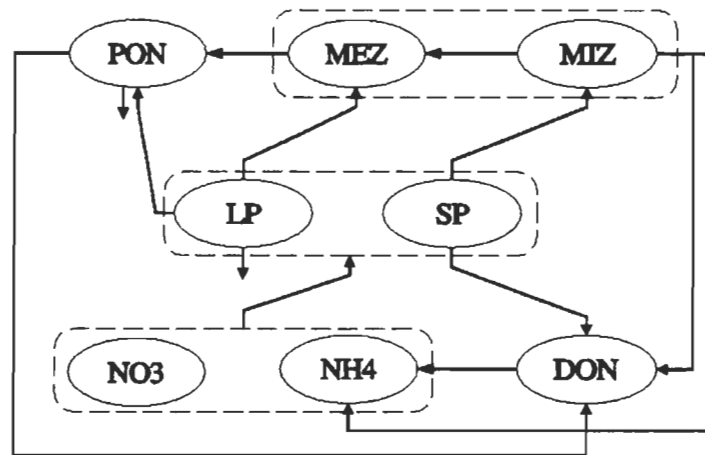


Figure II-2. Conceptual planktonic ecosystem model including nitrate (NO<sub>3</sub>), ammonium (NH<sub>4</sub>), large phytoplankton (LP), small phytoplankton (SP), mesozooplankton (MEZ), microzooplankton (MIZ), particulate organic nitrogen (PON) and dissolved organic nitrogen (DON). Arrows represent nitrogen fluxes between the biological components.

given in Table II-2.

### 3. *Coupling with the 3-D regional circulation model*

The partial differential equation used to compute the evolution of a simulated scalar (here C) is of the form:

$$\frac{\partial C}{\partial t} + u \frac{\partial C}{\partial x} + v \frac{\partial C}{\partial y} + w \frac{\partial C}{\partial z} = \frac{\partial}{\partial x} \left( K_x \frac{\partial C}{\partial x} \right) + \frac{\partial}{\partial y} \left( K_y \frac{\partial C}{\partial y} \right) + \frac{\partial}{\partial z} \left( K_z \frac{\partial C}{\partial z} \right) + \text{sources} - \text{sinks}.$$

where t is time, x, y, z are the spatial coordinates, u, v, w are the current velocities in the x, y, z directions, respectively;  $K_x$ ,  $K_y$  and  $K_z$  are the horizontal and vertical eddy diffusion coefficients, respectively; the sinks and sources are described in Table II-1. At each time step, the transport of each biological variable is performed by the advection-diffusion routine of the physical model while the sink and source terms are explicitly computed afterwards.

The present simulation covers the 1997 one year period. This year was chosen because the atmospheric and runoff conditions were close to their respective climatology. The physical and biological models are initialized with observations acquired during November and December 1996 throughout the GSL from the Atlantic Zone Monitoring Program [AZMP; Therriault *et al.*, 1998]. In order to initialize the biological model with a dynamically balanced physical ocean, the circulation model starts in November 1996 with observed temperature-salinity profiles interpolated to each model layer. It runs until January 1<sup>st</sup> 1997 at which time the profiles of nitrate and chlorophyll *a* (Chl *a*) from the

Table II-1. State variables and partial equations

Symbol	Meaning
NO3	Nitrate
NH4	Ammonium
LP	Large phytoplankton
SP	Small phytoplankton
MEZ	Mesozooplankton
MIZ	Microzooplankton
PON	Particulate organic nitrogen
DON	Dissolved organic nitrogen

$$\frac{dNO3}{dt} = -\mu_{LP} \cdot NuNO3_{LP} \cdot LP - \mu_{SP} \cdot NuNO3_{SP} \cdot SP$$

$$\frac{dNH4}{dt} = -\mu_{LP} \cdot NuNH4_{LP} \cdot LP - \mu_{SP} \cdot NuNH4_{SP} \cdot SP + ex \cdot MEZ + gz_{MIZ} \cdot (1 - eg) \cdot (1 - ass_{MIZ}) \cdot MIZ + rem \cdot DON$$

$$\frac{dLP}{dt} = (\mu_{LP} - m_{LP}) \cdot LP - gz_{MEZ} \cdot \left( \frac{LP}{LP + MIZ} \right) \cdot MEZ - sed_{LP} \cdot \frac{\partial LP}{\partial z}$$

$$\frac{dSP}{dt} = (\mu_{SP} - m_{SP}) \cdot SP - gz_{MIZ} \cdot MIZ$$

$$\frac{dMEZ}{dt} = gz_{MEZ} \cdot ass_{MEZ} \cdot MEZ - m_{MEZ} \cdot MEZ^2 - ex \cdot MEZ$$

$$\frac{dMIZ}{dt} = gz_{MIZ} \cdot ass_{MIZ} \cdot MIZ - m_{MIZ} \cdot MIZ - gz_{MEZ} \cdot \left( \frac{MIZ}{LP + MIZ} \right) \cdot MEZ$$

$$\frac{dPON}{dt} = gz_{MEZ} \cdot (1 - ass_{MEZ}) \cdot MEZ - m_{LP} \cdot LP - fg \cdot PON - sed_{PON} \cdot \frac{\partial PON}{\partial z}$$

$$\frac{dDON}{dt} = gz_{MIZ} \cdot eg \cdot (1 - ass_{MIZ}) \cdot MIZ + m_{MIZ} \cdot MIZ + m_{MIZ} \cdot MIZ - rem \cdot DON$$

Table II-2. Parameters used in the ecosystem model

Symbol	Meaning	Value and unit	Reference
<b>Light field</b>			
$k_w$	Pure seawater attenuation coefficient	0.04 m <sup>-1</sup>	<i>Morel</i> [1988]
$k_p$	Nonchlorophyllous matter-associated attenuation coefficient	0.04 m <sup>-1</sup>	fitted
<b>Phytoplankton</b>			
$k_{3LP}$	LP half-saturation constant for NO <sub>3</sub> uptake	1 mmol N m <sup>-3</sup>	<i>Parsons et al.</i> [1984]
$k_{4LP}$	LP half-saturation constant for NH <sub>4</sub> uptake	0.5 mmol N m <sup>-3</sup>	
$k_{3SP}$	SP half-saturation constant for NO <sub>3</sub> uptake	1 mmol N m <sup>-3</sup>	<i>Kiefer and Mitchell</i> [1983]
$k_{4SP}$	SP half-saturation constant for NH <sub>4</sub> uptake	0.1 mmol N m <sup>-3</sup>	
$k_e$	LP and SP half-saturation constant for light use	10 Ein m <sup>-2</sup> d <sup>-1</sup>	<i>Zakardjian et al.</i> [2000]
$dt_{min}$	LP and SP minimum doubling time	0.5 d	fitted
$m_{LP,SP}$	LP and SP mortality	0.02 d <sup>-1</sup>	<i>Smayda</i> [1970]
$sed_{LP}$	LP sinking rate	1 m d <sup>-1</sup>	
<b>Zooplankton</b>			
$g_{max_{MEZ}}$	MEZ maximum grazing rate	0.2 d <sup>-1</sup>	fitted
$g_{max_{MIZ}}$	MIZ maximum grazing rate	2 d <sup>-1</sup>	<i>Strom et al.</i> [2001]
$iv_{MEZ}$	Ivlev parameter of MEZ grazing formulation	0.8 (mmol N m <sup>-3</sup> ) <sup>-1</sup>	<i>Frost</i> [1972]
$k_{MIZ}$	half-saturation constant for MIZ grazing	0.8 mmol N m <sup>-3</sup>	fitted
$ass_{MEZ}$	MEZ assimilation efficiency	70 %	<i>Kiorbøe et al.</i> [1985]
$ass_{MIZ}$	MIZ growth efficiency	30 %	<i>Riegman et al.</i> [1993]
$m_{MEZ}$	MEZ mortality	0.05 (mmol N m <sup>-3</sup> d <sup>-1</sup> ) <sup>-1</sup>	fitted

$m_{\text{MIZ}}$	MIZ mortality	$0.02 \text{ d}^{-1}$	fitted
ex	NH <sub>4</sub> excretion by MEZ	$0.05 \text{ d}^{-1}$	<i>Safz and Alcaraz [1992]</i>
eg	DON egestion by MIZ	30 %	<i>Lehrter et al. [1999]</i>
<hr/>			
Detritus			
$\text{sed}_{\text{PON}}$	PON sinking rate	$100 \text{ m d}^{-1}$	<i>Turner [2002]</i>
fg	PON fragmentation rate	$0.05 \text{ d}^{-1}$	<i>Fasham et al. [1990]</i>
rem	DON remineralization rate	$0.4 \text{ d}^{-1}$	<i>Packard et al. [2001]</i>
<hr/>			

November-December 1996 observations are in turn interpolated and merged into the simulation. Equal concentrations of large and small phytoplankton were assumed to initiate the run. Because of the lack of data for the remaining biological scalars for the same period, idealized profiles were used. Values of  $1 \text{ mmol m}^{-3}$  for ammonium [e.g., *Levasseur et al.*, 1990; *Tremblay et al.*, 2000; *Zakardjian et al.*, 2000],  $0.05 \text{ mmol m}^{-3}$  for DON and  $0.005 \text{ mmol m}^{-3}$  for PON were assigned to each depth interval from the surface to the last active layer. Concentrations for mesozooplankton and microzooplankton were set to  $0.4 \text{ mmol N m}^{-3}$  [e.g., *Sime-Ngando et al.*, 1995; *Roy et al.*, 2000; *Savenkoff et al.*, 2000] in the upper 25 m and to 0 below this depth. Laterally homogenous initial conditions for the biological scalars were assigned to each grid point. At the open boundaries of the domain, the concentrations are maintained constant through time and are the same than those used for the initial conditions. Both chemical and biological variables are set to zero in the inflowing rivers. A dynamic equilibrium is reached after two to three weeks in January, mostly affecting the mesozooplankton and nitrate fields (seen in Figure II-3ac). Sea ice and winter mixing maintain the biological variables in a slowly-varying state until the spring bloom onset.

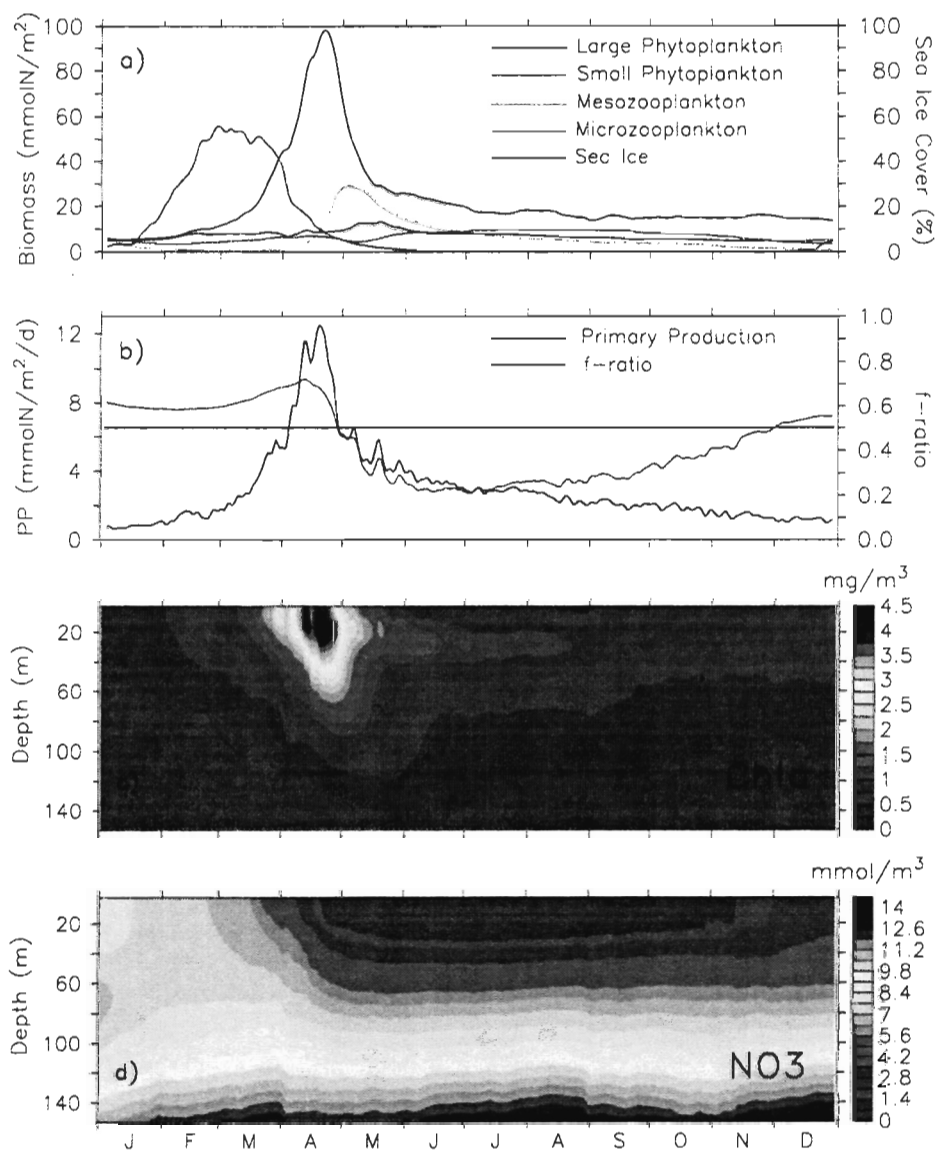


Figure II-3. Domain-averaged seasonal cycle of the (a) depth-integrated (0-45 m) biomass of plankton components with sea ice cover, (b) depth-integrated (0-45 m) total primary production with the depth-averaged (0-45 m) f-ratio (ratio of the total new primary production over total primary production), (c) total Chl *a* and (d) nitrate. The horizontal line in panel b indicates a f-ratio of 0.5.

## RESULTS

### 1. *Mean seasonal biomass and production cycle*

The coupled model produces a strong spatial and temporal variability of planktonic production due to the sea ice dynamics, freshwater runoff, tidal and wind-induced circulation and mixing. In order to facilitate the interpretation of the model results we examine the domain-averaged time series over the simulation period (Figure II-3). After a relatively low production winter period due to low light intensity and the sea ice cover (January to March), the diatom-dominated vernal bloom occurs in the second half of April following sea ice melt (Figure II-3a), and increasing light levels and stratification. The simulated timing of the bloom is consistent with previous observations, occurring generally from the end of March to the end of April [*de Lafontaine et al.*, 1991]. The mean depth-integrated (0-45 m) phytoplankton concentration during the peak of the spring bloom, 151 mg Chl *a* m<sup>-2</sup> (Figure II-3a), is of the same order of magnitude than observations, with maximum values ranging from 130 mg Chl *a* m<sup>-2</sup> [*Savenkoff et al.*, 2000] to 215 mg Chl *a* m<sup>-2</sup> [*de Lafontaine et al.*, 1991]. The coincident peak of primary production is mainly nitrate-based (f-ratio of 0.72, Figure II-3b) and reaches 1 g C m<sup>-2</sup> d<sup>-1</sup>, a spatially-averaged value that is near the lower bound of reported estimates of 1.6-5.7 g C m<sup>-2</sup> d<sup>-1</sup> in April [*Tremblay et al.*, 2000]. It reflects the time-differential onset of the spring bloom because maximum values of primary production ranging between 1.4 and 2.2 g C m<sup>-2</sup> d<sup>-1</sup> are found over 65 % of the GSL in April.

During the development phase of the bloom, the relative contributions of mesozooplankton grazing pressure on large phytoplankton biomass in the euphotic zone, senescence and sinking of viable cells out of the euphotic zone were similar. At the peak of the bloom, the grazing impact raised to 44 %, while senescence and cell sedimentation represented 28.6 % and 27.5 %, respectively. The decline of the vernal bloom was coincident with the nitrate depletion in the euphotic zone and an increasing grazing pressure from mesozooplankton. Approximately 11 days after the maximum phytoplankton biomass is reached, the model generates a peak of mesozooplankton biomass with a maximum of  $2.3 \text{ g C m}^{-2}$  (Figure II-3a), a reasonable value considering that reported mesozooplankton biomass are generally less than  $5 \text{ g C m}^{-2}$  in the GSL [Roy *et al.*, 2000]. This peak of mesozooplankton biomass in May leads to a higher grazing on microzooplankton and then a relaxation of the predation on small phytoplankton, as illustrated by a slight increase of its biomass (Figure II-3a).

Following the bloom and the nutrient depletion in the upper layer (Figure II-3d), a deep maximum of the phytoplankton biomass develops in the vicinity of the nitracline near 35 m (Figure II-3c), as classically observed during the stratified season in the GSL [e.g., Vandeveld *et al.*, 1987; Levasseur *et al.*, 1992; Ohman and Runge, 1994; Runge and de Lafontaine, 1996] and in other shelf seas [e.g., Holligan *et al.*, 1984]. The simulated deep maximum of phytoplankton biomass is mainly formed by large phytoplankton whereas small phytoplankton is confined to the upper layer (Figure II-4). During summer and fall, the large phytoplankton and mesozooplankton biomass gradually decreases to values near

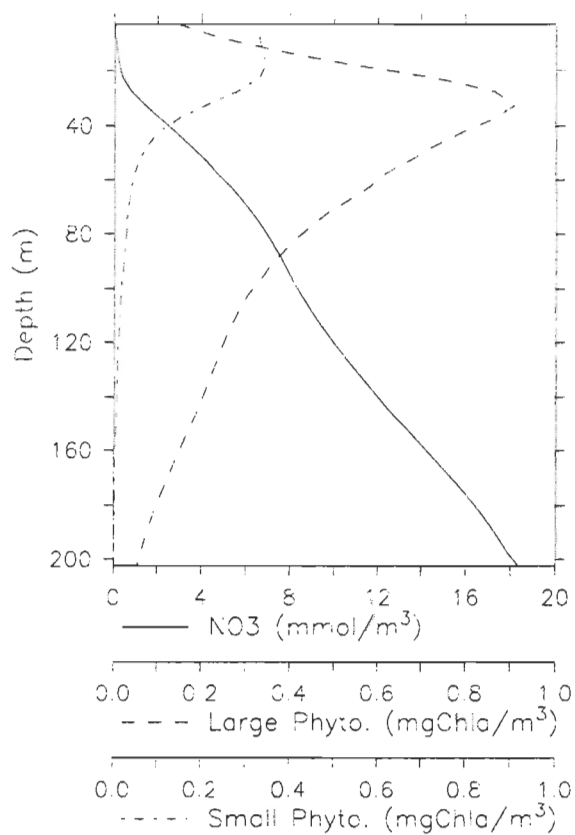


Figure II-4. Vertical distribution of the domain-averaged concentrations of nitrate (solid line), large phytoplankton (dashed line), and small phytoplankton (dashed-dotted line) on July 15<sup>th</sup>.

those simulated in the preceding winter (February). In contrast, the small phytoplankton and microzooplankton biomass shows only slight variations throughout the year, which is typical in the GSL [Savenkoff *et al.*, 2000]. During summer and fall, the mean domain-averaged biomass of 542 mg C m<sup>-2</sup> for small phytoplankton is comparable to the mean value previously reported for the GSL [636 mg C m<sup>-2</sup>; Savenkoff *et al.*, 2000]. In the same way, the yearly-averaged biomass of microzooplankton (0.5 g C m<sup>-2</sup>) compares well with seasonal means previously reported for the Lower Estuary [0.55 g C m<sup>-2</sup> in summer; Sime-*Ngando et al.*, 1995] and the GSL [0.53 g C m<sup>-2</sup> and 0.48 g C m<sup>-2</sup> in winter/spring and summer/fall, respectively; Savenkoff *et al.*, 2000].

Concomitantly with the phytoplankton biomass, the primary production gradually decreases during summer and fall (Figure II-3b). The mean summer primary production is 197 mg C m<sup>-2</sup> d<sup>-1</sup>, corresponding to the lower bound previously reported in the GSL [180-504 mg C m<sup>-2</sup> d<sup>-1</sup>; Tremblay *et al.*, 2000]. However, the primary production can locally reach values as high as 2.3 g C m<sup>-2</sup> d<sup>-1</sup> and 2.6 g C m<sup>-2</sup> d<sup>-1</sup> in the GSL and Lower St. Lawrence Estuary (LSLE), respectively. On average, regenerated production prevails in summer (0.21 < f-ratio < 0.30) while the fraction of new production continuously increases in fall (0.30 < f-ratio < 0.55) due to the nitrate replenishment of the euphotic zone from depth (Figure II-3b) associated to fall and winter wind-driven mixing. These results compare well with the relative contribution of nitrate to primary production calculated by Tremblay *et al.* [2000] for spring (73 %), summer (27 %) and fall (10-41 %).

The simulated Chl *a* and nitrate concentrations have been compared with *in situ* measurements from AZMP monitoring cruises made in June and November 1997.

Simulated data have been sampled in the model for the same dates and geographical positions (Figure II-5a) and interpolated to the bottles depth levels. The scatter plots compare measured vs simulated values and show the ability of the model to produce the correct order of magnitude of nitrate and Chl *a* concentrations for the two time periods (Figure II-5bc). Regarding Chl *a*, the differences between simulated and observed values are mainly within the range of uncertainty due to the use of fixed C/N and C/Chl *a* known to be highly variable in response to light conditions and nutrient availability. The simulated Chl *a* profiles are within or close to the range of variation of the observed vertical profiles and follow the observed seasonal evolution of the vertical distribution of Chl *a* (Figure II-5eg), despite a tendency to overestimate Chl *a* below the euphotic zone in both time periods. This tendency is mainly due to relatively low transfer rate from sinking LP to PON through natural mortality at depth in the model. Simulated and observed nitrate fields are in good agreement near the surface and at depth (Figure II-5df) with a tendency for lower simulated nitrate concentration at mid-depth (50-200 m) at the end of the simulation (November). Two hypotheses could account for this tendency. The first one involves the oversimplification of nutrient recycling at depth in the model. Respiratory activity in the intermediate and deep layers is not considered while it has been recognized as a key process in nutrient dynamics in the GSL [Savenkoff *et al.*, 2001]. A second hypothesis concerns inflowing Labrador Shelf cold waters that spread at mid-depth (50-120 m) along the north coast and leak in the northwestern gulf (NWG) and LSLE in less than a year [Saucier *et al.*, 2003]. The intermediate nitrate gradient would then be sensitive to the nitrate concentrations imposed at the Strait of Belle-Isle which are assumed time invariant

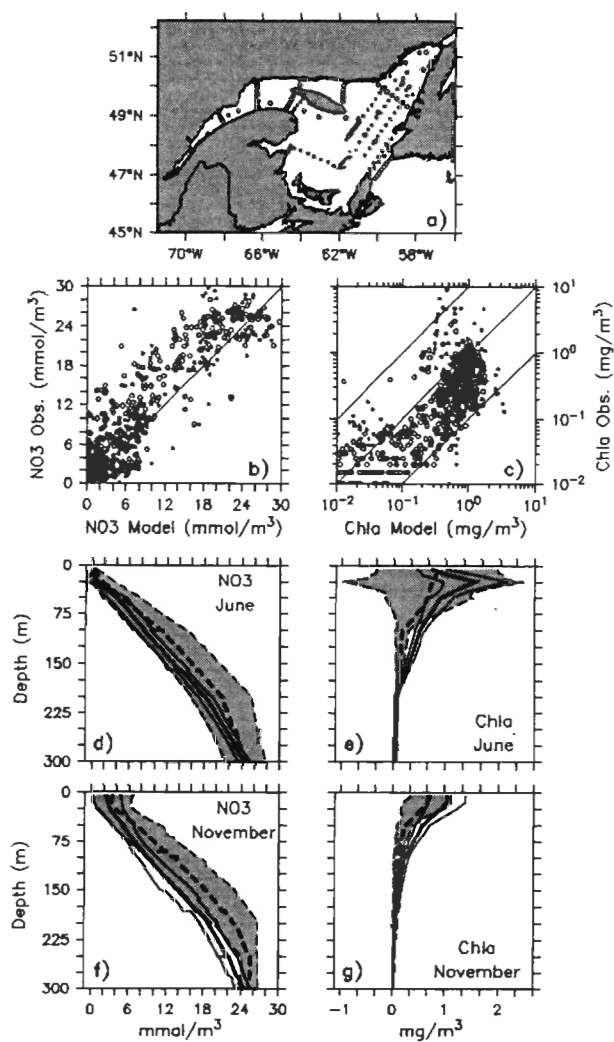


Figure II-5. Comparisons of simulated and observed data: (a) sampling locations in June (circles) and November (crosses) 1997; scatter plot of (b) nitrate and (c) total Chl *a*; profiles of simulated (solid line) and observed (dashed line) concentrations of (d) nitrate and (e) total Chl *a* in June and of (f) nitrate and (g) total Chl *a* in November. The bold line represents the spatially-averaged profile. The shaded area is delimited by the spatially-averaged profile  $\pm$  standard deviation (thin lines).

in this first version. The inflow of Labrador Shelf cold waters is more marked in fall [*Petrie et al.*, 1988; *Saucier et al.*, 2003] and nitrate boundary conditions may also play an important role in the preconditioning of the next year's bloom. Conditions at the Strait of Belle-Isle are generally not well monitored, and limit the precision of both physical and biological models. However, considering the overall agreement between simulated and observed nitrate concentrations in the upper 50 m, we are confident that the model reasonably captures the seasonal cycle of primary production in the GSL.

## 2. *Sub-regional differences in planktonic production*

Superimposed on the mean annual cycle, the model shows marked differences in the seasonal phytoplankton dynamics among and throughout the subregions of the GSL, as depicted by the mean algal biomass and associated standard deviations. The timing of the phytoplankton spring bloom does not appear to be synchronous with maximum values of phytoplankton biomass occurring from the beginning to the end of April (Figure II-6). This spatial variability of the spring bloom timing is mainly due to subregional differences in sea ice distribution, the later sea ice melt being associated to the later blooms, as on the Magdalen Shallow (MS) and northeastern gulf (NEG), a result that is consistent with observations [e.g., *de Lafontaine et al.*, 1991; *Koutitonsky and Bugden*, 1991]. Note that limited sea ice cover in winter (< 60 %) permits substantial increase of phytoplankton biomass in late February-early March, as in the southern Laurentian Channel (SLC) and NEG (Figure II-6), suggesting that light conditions are not limiting during this

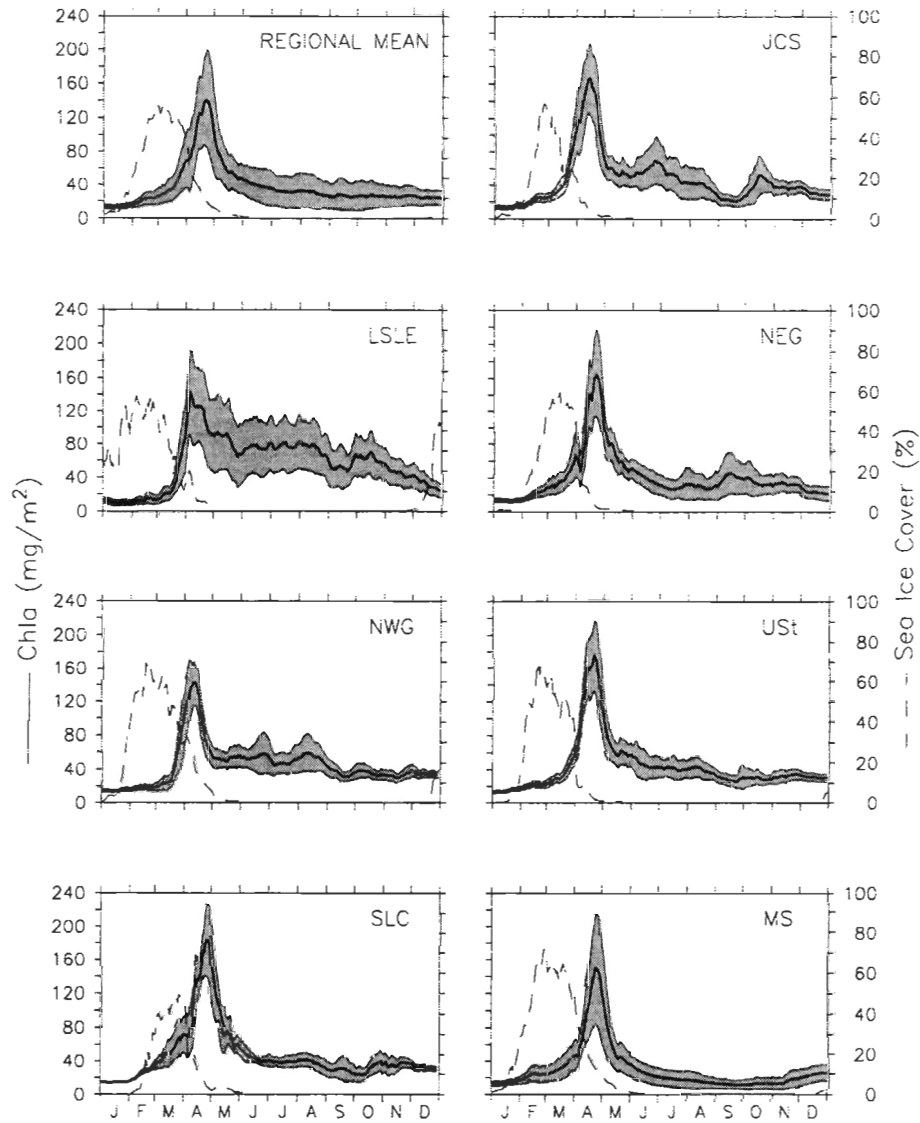


Figure II-6. Mean seasonal cycle of total Chl *a* (integrated between 0-45 m) and sea ice cover for the numerical domain and all subregions shown in Figure II-1. The shaded area is delimited by the spatially-averaged time series of total Chl *a* (bold line)  $\pm$  standard deviation (thin lines).

period. This result is consistent with the substantial levels of phytoplankton biomass reported in the GSL in late fall-early winter (CJGOFS cruises [e.g., *Roy et al.*, 2000; *Tremblay et al.*, 2000]) and late winter [*Hargrave et al.*, 1985] as well as with the bloom timing in conterminous shelf seas (Narragansett Bay [*Hitchcock and Smayda*, 1977]).

The LSLE, NWG, Jacques Cartier Strait (JCS) and Unguedo Strait (USt) subregions show marked deviations from the mean seasonal cycle, mainly through a higher summer primary production, as illustrated in Figure II-6 with the phytoplankton biomass. On an annual basis, these subregions are more productive than the MS, SLC and NEG (Figure II-7). The yearly simulated primary production averaged over both the LSLE and GSL is  $84 \text{ g C m}^{-2} \text{ yr}^{-1}$ , with local values ranging from less than  $50 \text{ g C m}^{-2} \text{ yr}^{-1}$  in the Northumberland Strait to more than  $150 \text{ g C m}^{-2} \text{ yr}^{-1}$  in the LSLE and JCS. The primary production in the MS is generally below the mean value ( $< 75 \text{ g C m}^{-2} \text{ yr}^{-1}$ ) while that of the NWG, USt and north coast is above the mean with local values greater than  $120 \text{ g C m}^{-2} \text{ yr}^{-1}$ . The high planktonic production in northeastern Cabot Strait is rather due to the continuous input of nitrate related to open boundary conditions. The inflow of Atlantic waters in this area continuously brings nutrient-rich surface waters in the model and generates an artificial area of high planktonic production. Nevertheless, this effect has a limited spatial extent and does not affect the results further into the GSL. The inflow of Atlantic waters is greater at depth but in a depth range (100-300 m) for which thermohaline and biogeochemical properties are poorly or even unaffected by the seasonal variability (by contrast with sea surface properties).

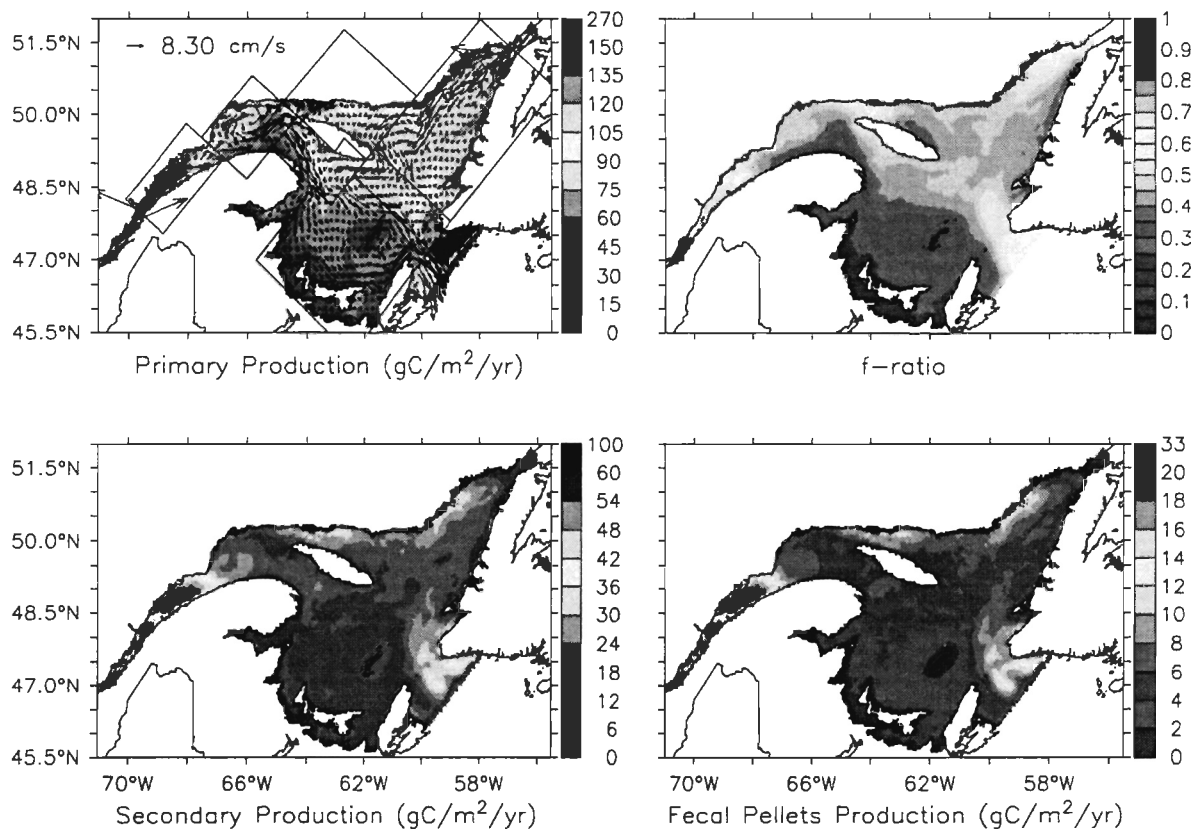


Figure II-7. Regional overview of the yearly- and depth-integrated (0-45 m) total primary production with depth- and yearly-averaged (0-45 m) currents, yearly- and depth-averaged (0-45 m) f-ratio, yearly- and depth-integrated (0-45 m) total secondary production, and yearly- and depth-integrated (0-45 m) fecal pellets production. Boxes on the upper left panel delimit the studied subregions.

Highest values of total primary production and f-ratio (Figure II-7) are found in subregions where the euphotic zone encounters higher nitrate concentrations. It indicates that increased summer primary production is first controlled by upward transport and turbulent diffusion of nitrate driven by the physical model. Similarly, the lowest nitrate concentrations and primary production rates are produced in the very shallow areas like in the Northumberland Strait and around the Magdalen islands. Since these areas are not nitrate-repleted after its exhaustion during the spring bloom, regenerated production prevails most of the year, as illustrated by the very low annual f-ratio values (about 0.2-0.3). Such spatial variations of primary production are mirrored on the annual secondary and fecal pellets production (Figure II-7), showing that increased primary production drives the herbivorous food web first in the model.

The more productive subregion is the LSLE, known to be strongly influenced by tidal upwellings of cold nutrient-rich intermediate waters occurring at the head of the Laurentian Channel [Steven, 1974; Greisman and Ingram, 1977; Gratton *et al.*, 1988; Saucier and Chassé, 2000]. This so-called “nutrient pump” supports high phytoplankton biomass throughout summer similar to bloom values [Levasseur *et al.*, 1984; Therriault and Levasseur, 1985; Plourde *et al.*, 2001], a result well reproduced in the model (Figure II-8). The resulting cold sea surface anomaly at the head of the deep through along with higher nitrate concentrations (Figure II-8) are clearly evidenced even on a summer mean in the model. Figure II-9bc illustrates the effect of the neap-to-spring tidal cycle on the nutrient replenishment of the upper layer through the shoaling of the nitracline and isopycnals.

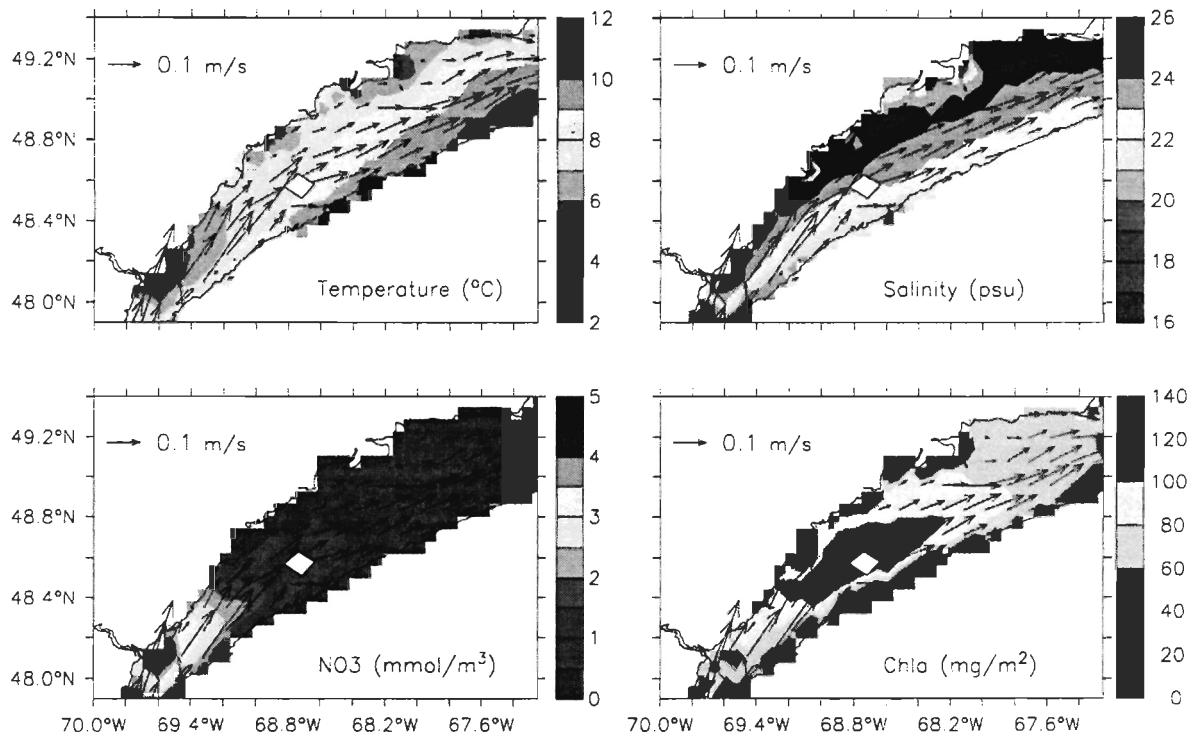


Figure II-8. May to October mean in the LSLE of sea temperature (5 m), salinity (5 m), nitrate (5 m), and depth-integrated (0-45 m) total Chl *a*. Mean summer currents (5 m) are overlaid in all panels.

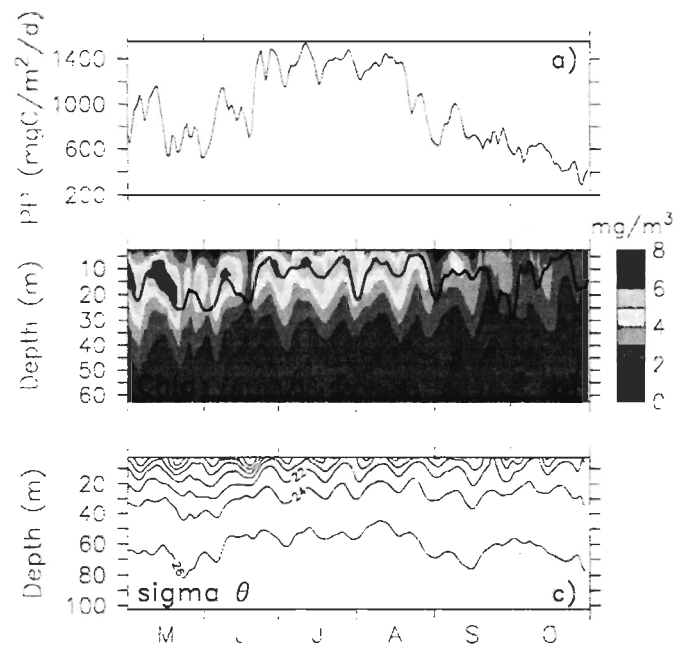


Figure II-9. Time series at a fixed station located in the upstream part of the LSLE (white box in Figure II-8) of the (a) total primary production (PP), (b) total Chl *a* with the depth of the nitracline overlaid, and (c) density ( $\text{kg m}^{-3}$ ).

Surface outcrop of low temperature and nutrient-rich waters from the cold intermediate layer is more important during fortnightly spring tides, and results in cyclic increases of phytoplankton biomass [Sinclair, 1978; Demers *et al.*, 1986]. In summer, the LSLE assumes one quarter of the total (i.e., the entire numerical domain) vertical advective and diffusive fluxes of nitrate at the bottom of the euphotic zone. These periodic inputs of nitrate considerably enhance primary production that reaches levels close to bloom values throughout the summer (Figure II-9a). Figure II-8 also illustrates the mean circulation over the summer in the LSLE with the preferential outflow of freshwater on the south coast and the spatial uncoupling between maximum phytoplankton and nitrate concentrations. This spatial uncoupling results from the rapid transport of phytoplankton biomass out of the high nitrate assimilation area (i.e., primary production), as previously described by Zakardjian *et al.* [2000]. However, the model generates a bloom at the beginning of April (Figure II-6) in the LSLE, at least two months earlier than generally reported [Sinclair, 1978; Levasseur *et al.*, 1984; Therriault and Levasseur, 1985; Sime-Ngando *et al.*, 1995; Roy *et al.*, 1996; Plourde *et al.*, 2001]. The late bloom in the LSLE is thought to be due to a combination of turbidity-induced light limitation and flushing related to the freshwater runoff [Therriault and Levasseur, 1985; Zakardjian *et al.*, 2000]. The light field formulation does not include the freshwater-induced turbidity due to nonchlorophyllous material drained by the rivers during the freshet. Consequently, the maximum depth of the simulated euphotic zone in the LSLE is similar to that of the GSL (40 m), i.e., that is twice deeper than generally observed in the estuary [15-20 m; Therriault and Levasseur, 1985; Sime-Ngando *et al.*, 1995].

Hence, the simulated early bloom in the LSLE is due to unrealistic light conditions in spring.

The NWG is characterized by a marked mesoscale variability that manifests through instabilities of the Gaspé Current and the occurrence of fronts and eddies generated by buoyancy and wind forcing [*Benoit et al.*, 1985; *Mertz et al.*, 1988; *Koutitonsky and Budgen*, 1991; *Sheng*, 2001]. Figure II-10 illustrates such a strong mesoscale variability of the circulation (depth-averaged currents from the surface to 45 m) and its impact on phytoplankton biomass (depth-integrated Chl *a* from the surface to 45 m) from spring to fall. In May, the currents show a typical situation characterized by a well established cyclonic Anticosti Gyre and a Gaspé Current close to the south shore [e.g., *El-Sabh*, 1976], where the phytoplankton biomass is twice higher than in the adjacent waters (80-90 mg Chl *a* m<sup>-2</sup> vs 40 mg Chl *a* m<sup>-2</sup>). A dipole-like structure is generated in August with a downstream anticyclonic gyre linked to a slow-growing instability of the Gaspé Current starting in late June in the model, a known feature of the NWG circulation [*Mertz et al.*, 1988; *Benoit et al.*, 1985; *Sheng*, 2001]. Later in fall (September and October), the anticyclonic gyre weakens, leading to the prevailing of the cyclonic gyre with consistently higher phytoplankton biomass in its center and in the Gaspé Current. Figure II-11 shows the spring to fall local variability of the density stratification, nitracline depth and vertical distribution of Chl *a* in the center of the Anticosti Gyre. Higher Chl *a* concentrations and primary production levels are associated to the uplifting of the nitracline and isopycnals in response to vertical motions governed by this mesoscale activity that hence controls the phytoplankton development in summer (Figure II-11).

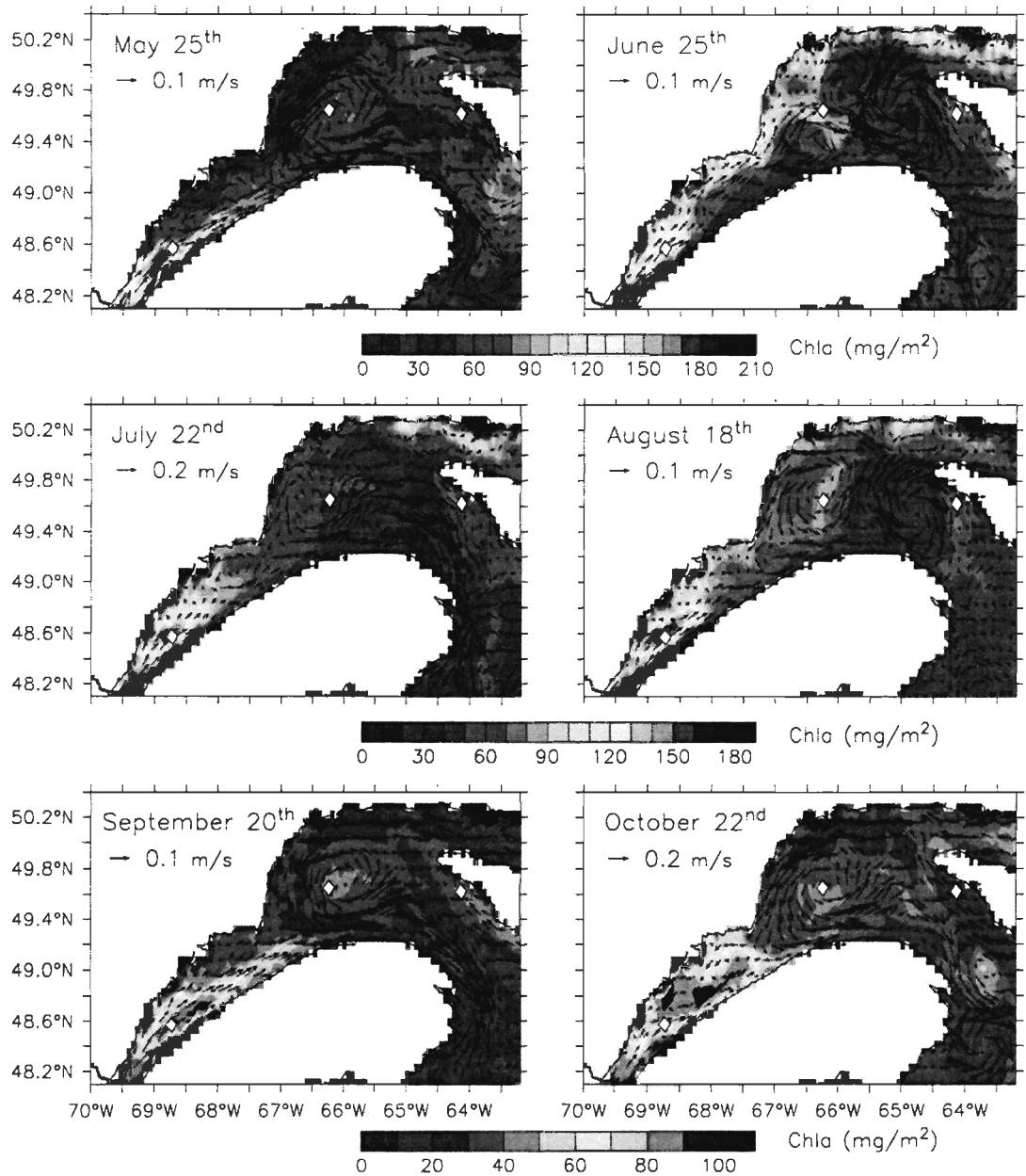


Figure II-10. Snapshots of the depth-integrated (0-45 m) total Chl *a* (mg m<sup>-2</sup>) with depth-averaged (0-45 m) currents on May 25<sup>th</sup>, June 25<sup>th</sup>, July 22<sup>nd</sup>, August 18<sup>th</sup>, September 20<sup>th</sup>, and October 22<sup>nd</sup> over the LSLE, NWG and northern USSt.

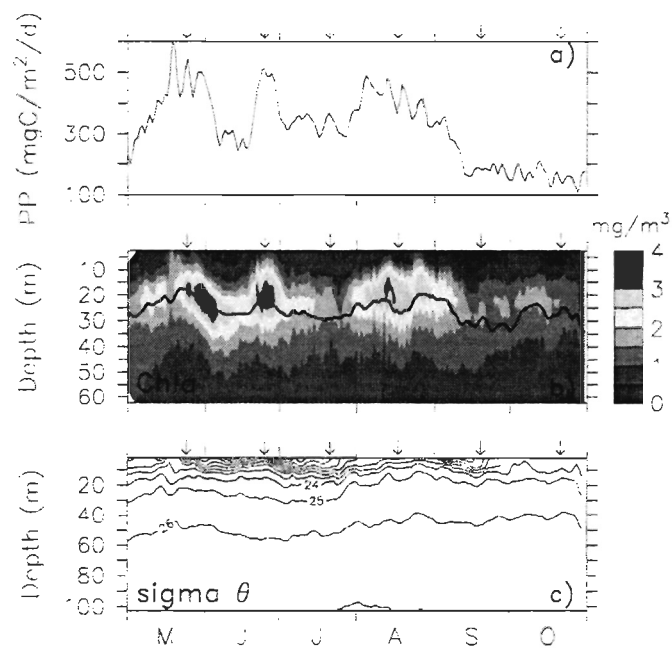


Figure II-11. Time series at a fixed station located in the NWG (white box in Figure II-10) of the (a) total primary production (PP), (b) total Chl *a* with the depth of the nitracline overlaid, and (c) density ( $\text{kg m}^{-3}$ ). Vertical arrows at the top of each panel indicate each snapshot of Figure II-10.

The model simulates higher production values mainly mediated by the herbivorous food web (see Figure II-7) along the southern Anticosti Island and the north coast, two areas subject to wind-induced upwellings [*Fuentes-Yaco et al.*, 1995, 1996, 1997ab; *Rose and Leggett*, 1988; *Saucier et al.*, 2003]. In the shallow western JCS, this higher productivity is reinforced by tidal mixing that characterizes this area [e.g., *Koutitonsky and Budgen*, 1991]. The higher productivity of the USt due to wind-induced upwelling activity along the southern Anticosti Island has already been highlighted by annual and seasonal composites and daily CZCS (Coastal Zone Colour Scanner) images of pigment concentration [*Fuentes-Yaco et al.*, 1995, 1996, 1997a]. Nevertheless, the USt is also strongly influenced by the Gaspé Current outflow [*Mertz et al.*, 1988] and the interaction of wind-induced upwellings with the Gaspé Current variability leads to a more complex situation than previously qualified in this region [e.g., *Fuentes et al.*, 1996, 1997a; see Figure II-10]. Figure II-12 illustrates such a simulated upwelling events occurring along the northwestern Anticosti Island on September 21<sup>st</sup> where a patch of high phytoplankton, mainly dominated by large algae (not shown), develops following a north-westerly wind events. In the following days, the wind-induced phytoplankton patch spreads in the USt due to transport by the Gaspé Current and circulation along Anticosti Island. The strong current shear induced by this complex circulation locally uplifts the nitracline and isopycnals leading to an increase of the phytoplankton biomass and production (Figure II-12 and II-13). Such an offshore transport of phytoplankton pigments, from the west coast of the Anticosti Island toward the MS, was reported by *Fuentes-Yaco et al.* [1995, 1996]. Figure

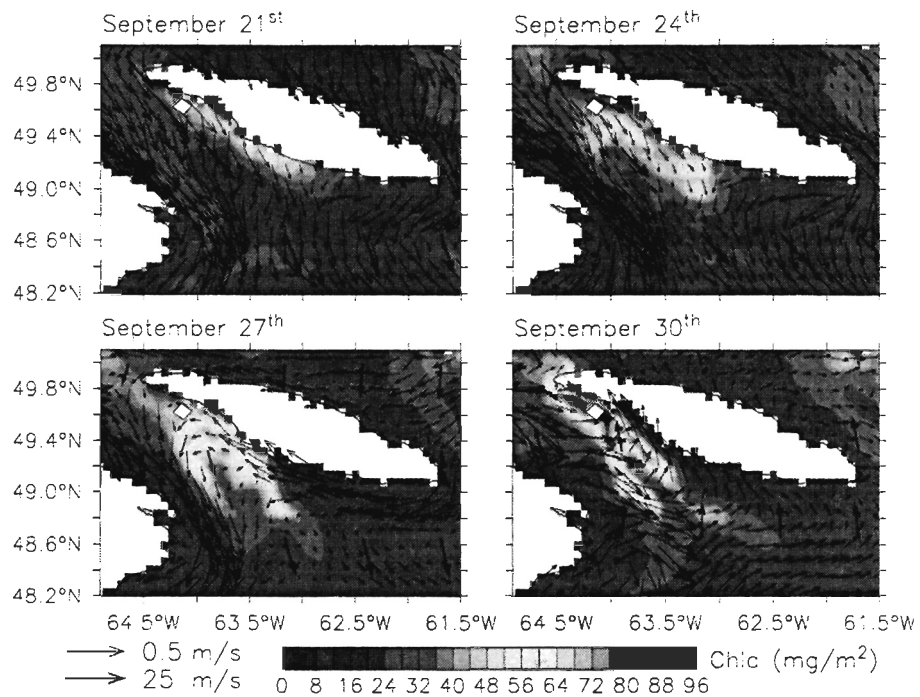


Figure II-12. Snapshots of the depth-integrated (0-45 m) total Chl *a* with depth-averaged (0-45 m) currents and surface winds (bold arrows) on September 21<sup>st</sup>, September 24<sup>th</sup>, September 27<sup>th</sup>, and September 30<sup>th</sup> in the US.

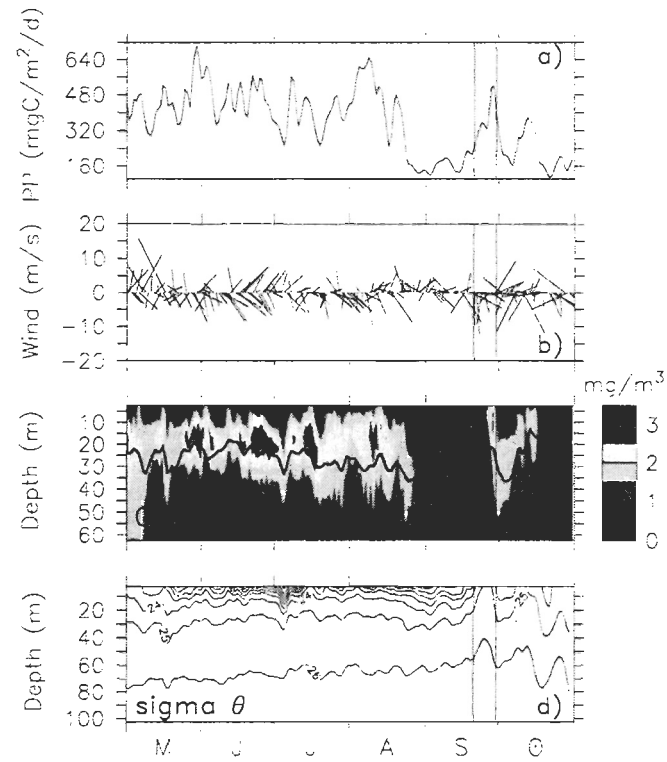


Figure II-13. Time series at a fixed station located in the USt (white box in Figure II-12) of the (a) total primary production (PP), (b) surface winds, (c) total Chl *a* with the depth of the nitracline overlaid, and (d) density ( $\text{kg m}^{-3}$ ). The two vertical lines delimit the time periods (September 21<sup>st</sup> to 30<sup>th</sup>) of the upwelling events shown in Figure II-12.

II-13 shows that these episodic inputs of nitrate in the euphotic zone frequently occur throughout the summer at the synoptic scale similar to that of wind events. In addition to the relatively well-known features described above, the model reveals patterns of higher planktonic production associated with Labrador Shelf waters entering the GSL through the Strait of Belle-Isle in late summer and fall. Labrador Shelf water inflows, with mean simulated transport rates between 0.2 Sv (summer and spring) and 0.4 Sv (fall and winter, see also *Petrie et al.*, 1988), are pulsed-like and spread along the north coast of the GSL. Such an event, occurring in late September-early October, is illustrated in Figure II-14 by a westward migrating sea surface temperature anomaly and an associated phytoplankton patch. The Chl *a* patterns closely follow the isolines of temperature as the cold surface waters spread westward. Figure II-14 also presents a 4 days (September 27<sup>th</sup> to 30<sup>th</sup>) SeaWiFS (Sea-viewing Wide Field-of-view Sensor) composite image that reveals a very similar patch of Chl *a*. The surface Chl *a* concentrations produced by the model are within 2-3 mg m<sup>-3</sup> of the SeaWiFS-derived values and, while the observed and simulated patches are not strictly coincident in time, they have similar spatial structures. Depth-integrated (0-45 m) phytoplankton biomass in the patch reaches bloom-like values (>100 mg Chl *a* m<sup>-2</sup>) contrasting with the lower level in the surrounding waters (20-40 mg Chl *a* m<sup>-2</sup>). The significant increase in algal biomass appearing on the mean seasonal cycle of the NEG and JCS (Figure II-6) in September and October, respectively, is due to this feature. The occurrence of such episodic events in summer and fall (see Figure II-15) is linked to Labrador Shelf water inflows, as shown by the moving window-averaged (14 days) time series on which high frequency perturbations and spring-neap tides are removed (Figure II-

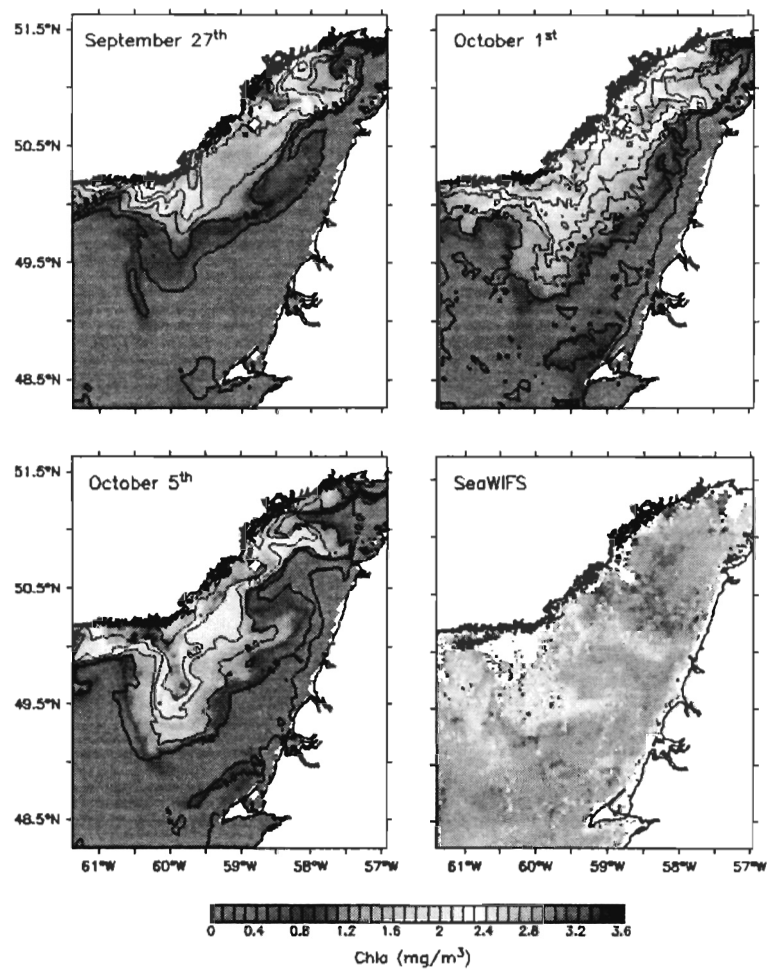


Figure II-14. Snapshots of the total Chl *a* (5 m) with sea temperature contours (°C, 5 m) on September 27<sup>th</sup>, October 1<sup>st</sup>, and October 5<sup>th</sup>. A 4 days (September 27<sup>th</sup> to September 30<sup>th</sup>) SeaWiFS composite image is presented in the lower right panel.

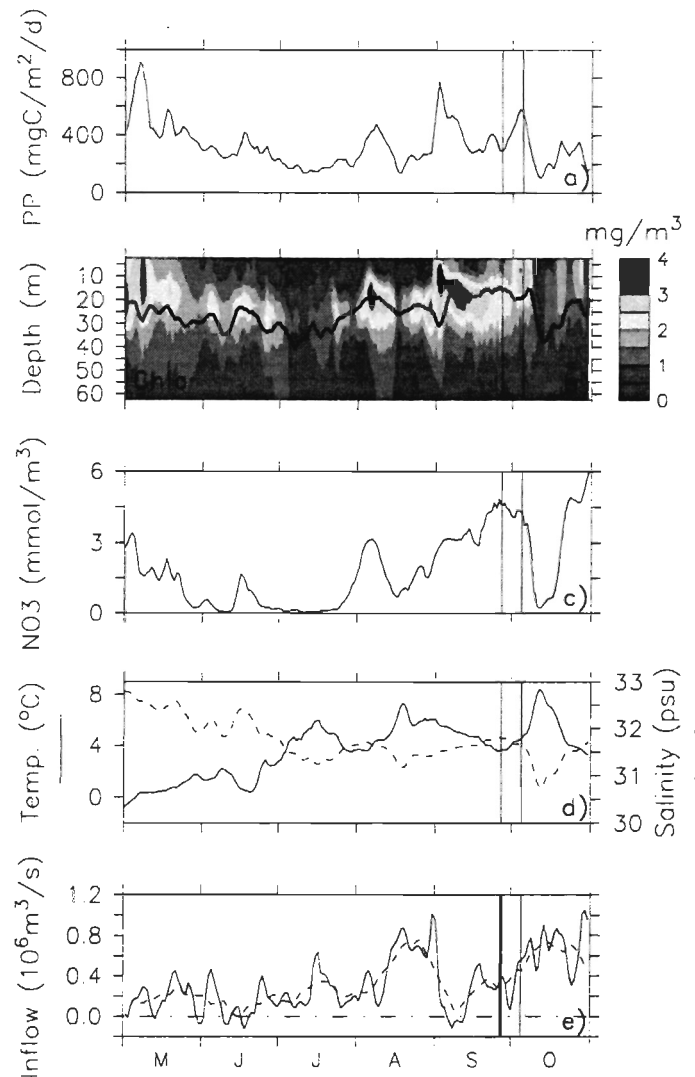


Figure II-15. Time series at a fixed station located in the NEG (white box in Figure II-14) of the (a) total primary production (PP), (b) total Chl *a* with the depth of the nitracline overlaid, (c) nitrate concentration at 25 m, (d) temperature and salinity at 25 m, and (e) net water transport across the Strait of Belle-Isle with its moving window-averaged (14 days) equivalent overlaid. The two vertical lines delimit the time periods (September 27<sup>th</sup> to October 5<sup>th</sup>) of the simulated events shown in Figure II-14.

15e). A pulse of water is associated with a time lag of 3-4 weeks to a surface outcrop of Labrador water through the euphotic zone due to wind-driven mixing, complex topography in this area, and local hydrodynamic processes related to the spreading of the pulse (7-10  $\text{cm s}^{-1}$ ). The uplifted waters are colder, saltier and nutrient-rich and substantially enhance algal biomass and primary production (Figure II-15a to d).

In the MS, SLC and NEG, the summer phytoplankton biomass is low in comparison to the subregions described above. The low production on the MS is related to the rapid nutrient depletion in spring, the strong thermocline and higher surface stratification in summer that limit the nitrate replenishment of the euphotic zone from depth [e.g., *Hargrave et al.*, 1985]. In summer, inputs of allochthonous nutrients on the MS can only originate from advective transport from the SLC and NWG through the two branches of the mean freshwater seaward circulation (Figure II-7a). Figure II-16 illustrates the mean nitrate concentrations and horizontal currents in summer along a SW-NE transect across the MS and the Laurentian Channel. When leaving the USt, the Gaspé Current outflow (Figure II-16a) forms two main branches of freshwater seaward circulation, one inshore and another at the shallow edge of the MS (Figure II-16bc), characterized by surface velocities ranging from 8  $\text{cm s}^{-1}$  to 18  $\text{cm s}^{-1}$ . The model shows that the nutrient transport through the seaward circulation does not significantly affect the southern MS primary production given the low nitrate concentration in the transported waters.

While the peak of primary production is similar to the more productive subregions, and even higher in the SLC, annual planktonic production in the NEG and SLC is low due to low summer production (Figure II-7). The spring bloom intensity is mainly dependant on

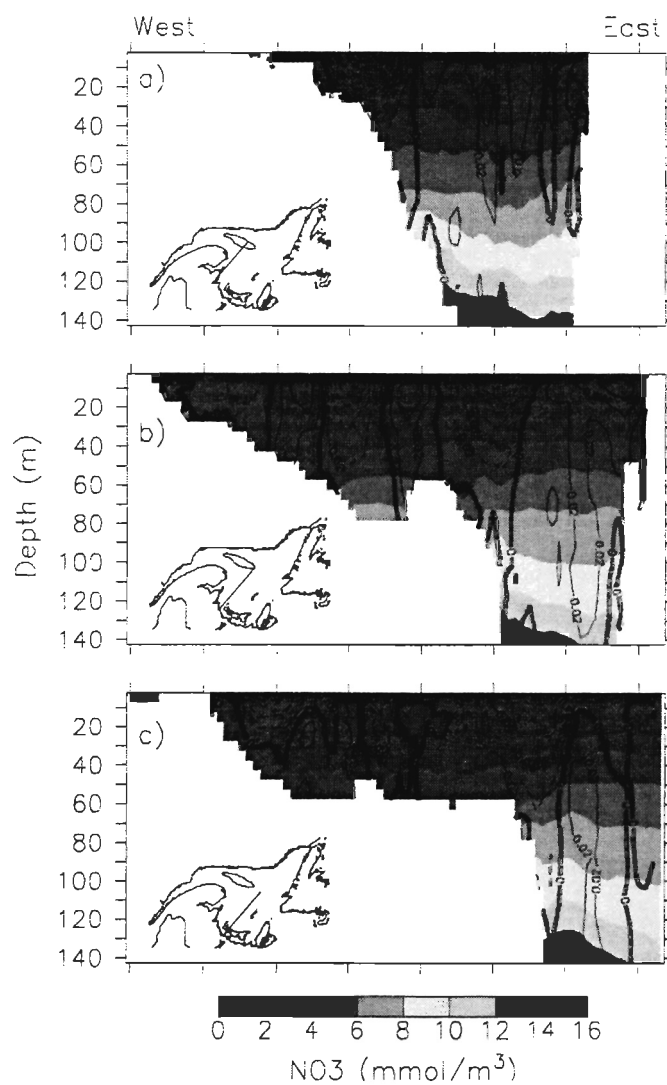


Figure II-16. Vertical sections from the MS towards the Laurentian Channel illustrating the nitrate concentrations and NW-SE currents ( $\text{m s}^{-1}$ ) averaged over July-August. The dashed and solid lines represent the seaward and northwestward current, respectively. On each panel, the location of the transect is indicated on the map.

nitrate replenishment from depth associated with winter mixing. This process may be higher in the SLC (Figure II-6) where deep mixing occurs due to sea ice formation and winds. Wind-driven mixing is the main process allowing nutrient replenishment of the euphotic zone in summer in these subregions where relatively low mesoscale activity prevails. The persistent pigment minimum reported along the west coast of Newfoundland [*Fuentes-Yaco et al.*, 1997a], where southerlies would drive a downwelling circulation [*Gilbert and Pettigrew*, 1993], is well reproduced by the model (see Figure II-7).

## DISCUSSION

The present model was developed to gain a better understanding of the effect of the climatic and oceanographic conditions on planktonic production in the Gulf of St. Lawrence. Given the richness of the physical processes in this coastal oceanographic system, described by *Koutitonsky and Bugden* [1991] and simulated by *Saucier et al.* [2003], we chose to use a moderately complex planktonic ecosystem model to approximate the biological response to the high frequency to seasonal variations of environmental conditions generated by the sea ice-ocean model. While the planktonic ecosystem model is more simple than the biogeochemical model of *Tian et al.* [2000, 2001], solutions produced by the coupled model at the regional and subregional scale are overall in agreement with historical data. It produces a mean (i.e., spatially-averaged over the numerical domain) seasonal cycle dominated by a large phytoplankton spring bloom followed by the development of a deep maximum of phytoplankton biomass persistent in summer and the prevailing of regenerated production, as classically described in the region [e.g., *de Lafontaine et al.*, 1991; *Savenkoff et al.*, 2000; *Tremblay et al.*, 2000; *Tian et al.*, 2000, 2001].

The model does not generate any significant fall bloom at the regional scale but reveals fall blooms related to local environmental conditions such as pulsed inflows of Labrador Shelf water along the north coast (Figure II-6). The fall bloom is a well known feature of the primary production cycle in temperate coastal seas. It is induced by increased wind-driven turbulent mixing during autumn storms that erode the summer stratification,

favouring the nutrient replenishment of the impoverished surface layer and hence phytoplankton growth until light availability becomes limiting in early winter. The absence of a regional fall bloom in the simulation may come from the low wind regime in fall 1997: while the wind forcing database used to drive the physical model presents strong wind events in fall 1997 (up to  $20 \text{ m s}^{-1}$ ), those do not generate any significant mixing events at the regional scale. This result is supported by biweekly composite SeaWiFS images for 1997. Preliminary runs made for 1998 and 1999 with the same model configuration generate marked fall bloom underlining the strong interannual variability of the GSL physical conditions in fall.

Superimposed to the mean annual cycle, the model generates a marked heterogeneity of summer planktonic production in the Lower Estuary and the Gulf of St. Lawrence. Different physical processes - tidal mixing, buoyancy-driven circulation, wind-induced coastal upwelling - drive the nutrient availability for phytoplankton, and consequently primary production events with different time and space scales. The model reproduces the high summer planktonic production in the LSLE, which is largely due to nutrient fluxes driven by the high tidal mixing in this subregion [*Levasseur et al.*, 1984; *Therriault and Levasseur*, 1985; *Levasseur and Therriault*, 1987]. It also generates coastal upwellings along the north coast of the GSL and the western Anticosti Island which are shown to increase the algal biomass, dominated by large phytoplankton, and planktonic production. Widely distributed year-round, wind-induced coastal upwellings are known to have a marked effect on oceanic heat fluxes [*Saucier et al.*, 2003] and phytoplankton pigments [*Fuentes-Yaco et al.*, 1995, 1996, 1997ab] in the GSL. The buoyancy-driven circulation

induced by the runoff of the St. Lawrence Estuary shows a typical mesoscale variability acting on a weekly to seasonal time scale that leads to a higher productivity in the NWG. The very high phytoplankton biomass regularly observed in the Gaspé Current [Sévigny *et al.*, 1979; Levasseur *et al.*, 1992] was not always clearly reproduced by the model, particularly in spring and fall. Levasseur *et al.* [1992] suggested that the high phytoplankton biomass in the Gaspé Current in spring may result from the advection of high biomass from the estuarine waters (see Figure II-10). The fact that the model does not include the higher turbidity of estuarine waters and overestimates the nitrate consumption in the LSLE explains the low nutrient concentration and phytoplankton biomass in the Gaspé Current in spring. Summer observations in the Gaspé Current have revealed nutrient-impooverished and low phytoplankton conditions in the jet while secondary circulation may increase nutrient availability and primary production in the frontal zone between the estuarine and gulf waters [Levasseur *et al.*, 1992]. These observations are more coherent with our simulation but this frontal-induced higher productivity may be underestimated in the model. The spatial resolution of the model being half to one third of the baroclinic Rossby radius of deformation in this subregion (10-15 km), the model is able to generate mesoscale features but frontal-induced increased phytoplanktonic production often results of submesoscale processes [e.g., Woods, 1988; Zakardjian and Prieur, 1998] which may not be resolved with the present resolution. Mahadevan and Archer [2000] and Lévy *et al.* [2001] examined the effect of model resolution on resolving vertical motions, nutrients flux and primary production in mesoscale and frontal structures and have shown that regional primary production increases with the model resolution. The simulated NWG production

and its impact on downstream areas may thus be underestimated. Nevertheless, it is clearly evidenced that the mesoscale variability associated to the buoyancy-driven circulation in the LSLE, NWG and USt plays a fundamental role in the dynamics of planktonic production in these subregions of the GSL.

The model also simulates the effect of hydrodynamics on the competition between the herbivorous and microbial food webs, a prerequisite for estimating carbon flux as it is known that the ecosystem structure drives the carbon flux at depth [e.g., *Longhurst and Harrison, 1989; Legendre and Le Fèvre, 1995; Legendre and Michaud, 1998; Legendre and Rivkin, 2002*]. Highest variations of biomass in the mean seasonal cycle concern the herbivorous food web while the simplified microbial food web constitutes a background of biomass with only slight variations throughout the year, as previously reported in the GSL [*Tremblay et al., 1997; Doyon et al., 2000*] and on the Scotian Shelf [*Mousseau et al., 1996; Dauchez et al., 1996*]. Large phytoplankton biomass and production were found to be favoured in summer in the frontal zone of the Gaspé Current, which is known to be a highly productive system [*Fortier et al., 1992; Levasseur et al., 1992; Tremblay et al., 1997*]. In response to tidal mixing, wind-induced coastal upwellings, buoyancy-driven gyres, frontal zones and eddies, the model generates higher large phytoplankton production and biomass that stimulates the activity of the herbivorous food web (Figure II-7) compared to less dynamic subregions. The increased activity of the herbivorous food web in response to mesoscale circulation is a well known feature in oceanic environments [e.g., *Thibault et al., 1994; Peinert and Miquel, 1994; Ressler and Jochens, 2003*]. The dominance of small phytoplankton biomass on the bulk of Chl *a* in summer [*Sévigny et al., 1979; Ohman and*

*Runge, 1994; Claereboudt et al., 1995; Tamigneaux et al., 1997, 1999; Tremblay et al., 1997, 2000*] is not evidenced on the mean seasonal cycle (Figure II-3a) but is more obvious at smaller scales: less productive subregions show a decrease of the large vs total phytoplankton ratio in summer comparatively to more productive ones, as illustrated in Figure II-17. By comparison with the NWG always clearly dominated by diatoms, the higher standard deviation in July and August in the NEG indicates that small phytoplankton can locally constitute 60-70 % of the bulk of the algal biomass. In less productive subregions, such as the MS, the small phytoplankton dominates the bulk of Chl *a* throughout summer. These results highlight the variability that prevails at different scales in the GSL and shows that the model produces the correct trend.

The mean annual primary production computed for the whole Estuary and Gulf ( $84 \text{ g C m}^{-2} \text{ yr}^{-1}$ ), resulting from this high resolution physically-driven numerical experiment, is low in comparison with previous estimates of  $212 \text{ g C m}^{-2} \text{ yr}^{-1}$  [*Steven, 1974*] and  $288 \text{ g C m}^{-2} \text{ yr}^{-1}$  [*Roy et al., 2000*]. The overall agreement between observed and simulated nitrate concentrations tends to support the order of magnitude of our simulated new primary production but, regarding summer primary production, a key process probably oversimplified in the model concerns nitrogen recycling mediated through microbial trophic pathways. It would be particularly important in the shallow southern MS where a rapid turnover of the organic matter in the euphotic zone, rather than nutrients diffusion from depth, is thought to drive most of the summer primary production [*Hargrave et al., 1985*]. A microbial activity is implicitly included in the planktonic ecosystem model by way of constant transfer rates governing the breakdown of PON into DON and subsequent

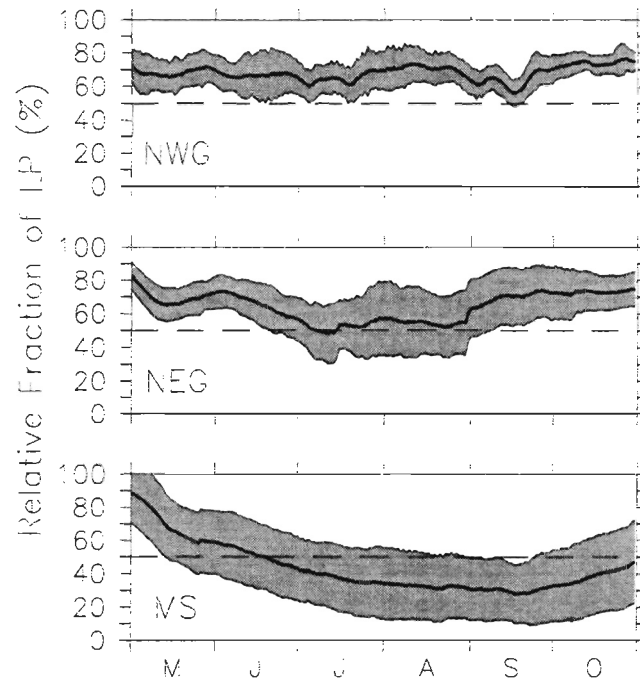


Figure II-17. Time series of the depth-averaged (0-45 m) relative fraction of large phytoplankton (LP) averaged over the NWG, the NEG, and the MS (bold line). The shaded area is delimited by the mean  $\pm$  standard deviation (thin lines). The horizontal dashed line indicates a relative fraction of 50 %.

DON ammonification. This parameterization assumes a constant bacterial activity throughout the year while it has been reported to double from the winter-spring to the summer-fall period in the GSL [Savenkoff *et al.*, 2000]. In addition, there is some evidence about the temperature control of bacterial activity in cold coastal waters [Pomeroy and Deibel, 1986]. The inclusion in the model of a bacterial component with temperature-dependent biological rates would delay the DON ammonification with a subsequent increase of regenerated production later in summer [e.g., Tian *et al.*, 2001] but is not expected to produce a twofold increase of annual primary production. PON residence time in the euphotic zone is also a critical parameter in regard to regenerated primary production shown to increase as the sinking rate decreases [Ducklow and Fasham, 1992; Crise *et al.*, 1999]. In the model, the PON flux at the bottom of the euphotic zone summed over the April-May period is equivalent to  $11.6 \text{ g C m}^{-2}$  (using a C/N ratio of 6.625) and its regeneration in the euphotic zone would represent an increase of 14 % of our annual estimate of primary production.

Primary production is tightly linked to zooplankton dynamics through nutrient recycling and top-down control and the lack of pertinent zooplankton data, that are greatly more time expensive to acquire than primary production related variables, is often a weakness of NPZD modelling [e.g., Franks, 2002; Runge *et al.*, 2005]. While we do not have sufficient data to validate zooplankton results, it is important to discuss here the robustness of the model in view of the general knowledge on grazers' dynamics in the GSL and more generally in temperate and high latitude coastal seas. The simulated annual secondary production of mesozooplankton averaged over the domain reaches  $12.6 \text{ g C m}^{-2}$

and  $16 \text{ g C m}^{-2}$  when integrated over the euphotic zone and the entire water column, respectively. Such values are within the range given by *Koski et al.* [1999] in the southwestern coast of Finland, i.e.,  $10.5\text{-}28.1 \text{ g C m}^{-2}$ . Concerning microzooplankton, we do not report in the literature any annual production estimate in coastal waters. Nonetheless, *Levinsen and Nielsen* [2002] estimate to 20-60 % the annual primary production processed by ciliates in high-latitude coastal environments. In regard to that study, the fraction of small phytoplankton primary production transferred to microzooplankton biomass calculated by the model (26.7 %) is consistent, considering that microzooplankton only grazes on small phytoplankton. On an annual basis, 24.2 % of the simulated total primary production is channelled towards the total secondary production, an estimate that fits in the range (20-30 %) given by *Legendre and Rassoulzadegan* [1999]. It can be assumed that, on an annual basis, the coupled model simulates a grazer dynamics consistent with general findings on planktonic production in temperate and high latitude seas.

Note finally that the simulated primary production is calculated from nitrogen uptake using a fixed Redfield C/N ratio thus assuming that carbon and nitrogen dynamics are coupled, an assumption still in debate for mid- and high-latitude regions [e.g., *Sambrotto et al.*, 1993; *Daly et al.*, 1999]. Carbon and nitrogen metabolisms can be temporally uncoupled, especially during nitrogen depletion, with dissolved inorganic carbon uptake that can exceed nitrogen uptake [*Dubinsky and Berman-Frank*, 2001; *Engel et al.*, 2002]. Hence, the simulated primary production derived from the Redfield ratio may represent a lower bound. Using an algal C/N ratio of 8.5 [e.g., *Grégoire and Beckers*, 2004], the

simulated primary production reaches  $108 \text{ g C m}^{-2} \text{ yr}^{-1}$  (an increase of 28%). When summed to the PON flux ( $15 \text{ g C m}^{-2} \text{ yr}^{-1}$  with a C/N ratio of 8.5), it gives an estimate that is 46% higher ( $123 \text{ g C m}^{-2} \text{ yr}^{-1}$ ) than the primary production obtained when using a Redfield-type C/N ratio ( $84 \text{ g C m}^{-2} \text{ yr}^{-1}$ ). Nevertheless, this new estimate of the maximum expected annual primary production remains half those estimated by *Steven* [1974] and *Roy et al.* [2000].

The mean annual primary production computed by the model is the first estimate in the GSL that integrates hourly to seasonal fluctuations of both physical and biological processes concomitantly with a high spatial resolution and complete evenly-weighted spatio-temporal coverage. Given the overall agreement between simulated and observed nitrate and Chl *a* concentrations (Figure II-5), the model reasonably captures the natural variability of nitrate and Chl *a* vertical distribution. Moreover, the striking agreement between the simulated and SeaWiFS-derived surface Chl *a* concentrations in late September in the NEG (Figure II-14) demonstrates the ability of the model to generate local transient events that can hardly be evidenced at sea with usual sampling scheme. Lately, local daily primary production rates computed by the model are well in the range of measured values in the GSL. We suggest that the low mean annual primary production given by the coupled model comes from the weight of the less productive subregions (MS and NEG) in the spatial averaging as the locally computed annual primary production rates (Figure II-9) are close to reported values in highly productive subregions, as the LSLE [ $104 \text{ g C m}^{-2} \text{ yr}^{-1}$ ; *Levasseur and Therriault*, 1985]. The *Steven* [1974] estimate of the gulf mean annual primary production was derived from an extensive data sets covering the GSL and

the main production period (May-September) by extrapolating hourly production rates (among the highest reported for the GSL) on the basis of monthly mean light period and, consequently, tends to be overestimated (M. Gosselin, personal communication, 2004). Annual primary production estimated by *Steven* [1974] for the LSLE ( $508 \text{ g C m}^{-2} \text{ yr}^{-1}$ ) is 5-folds higher than the value given by *Therriault and Levasseur* ( $104 \text{ g C m}^{-2} \text{ yr}^{-1}$ , 1985) which is closer to the model solution ( $154 \text{ g C m}^{-2} \text{ yr}^{-1}$ ). The CJGOFS estimate of  $288 \text{ g C m}^{-2} \text{ yr}^{-1}$  from *Roy et al.*, [2000] results from a limited set of observations (5 stations visited 2-6 times between 1992 and 1994) that is far from the spatio-temporal resolution of the model. The annual estimate was made by extrapolation of two seasonal means of daily primary production (winter-spring and summer-fall; see *Savenkoff et al.*, 2000), the winter-spring mean ( $1358 \text{ mg C m}^{-2} \text{ d}^{-1}$ , *Savenkoff et al.*, 2000) taking into account the spring bloom and relatively high but punctual winter values. Extrapolated over the winter-spring period (157 days), it results an estimate ( $213 \text{ g C m}^{-2} \text{ yr}^{-1}$ ) similar to the Steven's annual primary production ( $212 \text{ g C m}^{-2} \text{ yr}^{-1}$ ) that largely overestimates the winter production. Time resolution being a key parameter in estimating primary production [*Wiggert et al.*, 1994], it is clear that extrapolation of sparse measurements over an annual estimate would be imprecise in a highly dynamic system like the GSL.

In addition, the nitrate stocks exhibit a strong interannual variability in the GSL related to winter convection [*Plourde and Therriault*, 2004] to which the magnitude of primary production is strongly dependant. In early spring, nitrate concentrations in the surface mixed layer were up to  $5 \text{ mmol m}^{-3}$  lower in 1997 ( $7 \text{ mmol m}^{-3}$ ) than during the CJGOFS sampling years [ $9\text{-}12 \text{ mmol m}^{-3}$ ; *Plourde and Therriault*, 2004]. Figure II-3 shows

that the model reproduces nitrate concentrations ( $6.3\text{-}7.7 \text{ mmol m}^{-3}$  in February-March) very close to the value given by *Plourde and Therriault* [2004] for the year 1997. This suggests that interannual variability can also contribute to explain the apparent discrepancy between our estimate of the mean annual production and the *in situ* estimate of *Roy et al.* [2000]. Our simulated GSL mean annual primary production is finally in the range of reported estimates for shelf seas at moderate to high latitudes, such as the Central North Sea [ $90\text{-}97 \text{ g C m}^{-2} \text{ yr}^{-1}$ ; *Skogen and Moll*, 2000], the Scotian Shelf [ $62\text{-}102 \text{ g C m}^{-2} \text{ yr}^{-1}$ ; *Mousseau et al.*, 1996] and the Black Sea [ $101 \text{ g C m}^{-2} \text{ yr}^{-1}$  with a C/N ratio of 6.625; *Grégoire and Beckers*, 2004].

## CONCLUSIONS

Given the richness of the physical and biological conditions that are evidenced by the coupled model, it appears clearly that the Gulf of St. Lawrence cannot be considered as a single homogeneous entity. The strong variability that prevails in the GSL should be accounted for in the perspective to predict and evaluate the effects of climate change on high latitude marginal seas productivity. The spring bloom intensity being almost similar in all subregions of the GSL (Figure II-6), the spatial variability of yearly-integrated primary production (Figure II-7) results from differences in summer primary production generated by different physical regimes. This suggests that, outside the spring bloom period, primary production is locally of the same order of magnitude than during the spring bloom. Hence synoptic variability may be as important as the seasonal variability. The buoyancy-driven circulation in the NWG is influenced by the hydrographic and wind regimes [*Tang, 1980a; Mertz et al., 1988; Mertz et al., 1991; Koutitonsky and Bugden, 1991*] and thus subject to interannual variability. Upwelling events are linked to the synoptic wind variability which is typically 3-9 days in Eastern Canada [e.g., *Koutitonsky and Bugden, 1991*] but their frequency and duration may vary from year to year. Considering their impact on planktonic productivity at the subregional scale, the interannual variability of wind and hydrologic regimes can play a significant role in the interannual variability of the GSL planktonic production. This strengthens the need for an intensive monitoring program in the GSL like the Atlantic Zone Monitoring Program [*Therriault et al., 1998*] which, in conjunction with the present model, will allow a better understanding of the interannual variability in the

planktonic production. The present study highlights the abilities and limitations of the coupled model. The next step will be to run a refined version of the model for 1997 to 2003 to be analyzed with respect to the Atlantic Zone Monitoring Program database. Refinements would include a more accurate formulation of light conditions in estuarine waters, necessary to achieve a more realistic planktonic dynamics in the LSLE and western GSL, an improved formulation of nitrogen recycling in the whole water column and, finally, the use of year-specific seasonally varying boundary conditions of nitrate and Chl *a* at Cabot Strait and the Strait of Belle-Isle.

## APPENDIX. PLANKTONIC ECOSYSTEM MODEL DESCRIPTION

All variables are expressed in units of  $\text{mmol N m}^{-3}$ , considering that nitrogen is the main limiting nutrient for phytoplankton growth. Silicate limitation is not considered in the model and is not expected to greatly influence the competition between both size fractions because the Si/N03 ratio is generally near 1/1 in the gulf waters [Tremblay *et al.*, 1997]. In the same way, phosphate was not found to limit phytoplankton growth [Levasseur and Therriault, 1987] and trace metals limitation is unlikely due to their substantial concentrations in the coastal waters [e.g., Yeats, 1990]. In order to compare numerical solutions with historical data, primary production and phytoplankton biomass were converted in usual units using a molar C/N ratio of 106/16 [Redfield *et al.*, 1963] and a C/chlorophyll *a* mass ratio of 55 [Rivkin *et al.*, 1996; Sinclair, 1978].

The phytoplankton growth rate ( $\mu$ ) is a function of both light and nitrogen availability. It is computed following the Liebig's law of the minimum from nutrients-based ( $\text{dtn}_{\text{LP,SP}}$ ) or light-based ( $\text{dte}$ ) doubling time of the biomass [Eqs. 1-3, e.g., Prieur and Legendre, 1988; Zakardjian and Prieur, 1994, 1998; Zakardjian *et al.*, 2000]. The formulation is the same for the two size fractions of phytoplankton with parameters shown in Table II-2. It gives for large phytoplankton (LP):

$$\mu_{\text{LP}} = \frac{\ln(2)}{\max(\text{dtn}_{\text{LP}}, \text{dte})}, \quad (1)$$

With

$$\text{dte} = \text{dtmin} \cdot \left(1 + \frac{\text{ke}}{E}\right), \quad (2)$$

$$dtn_{LP} = \frac{dtmin}{f(N)_{LP}}, \quad (3)$$

where  $f(N)_{LP}$  is the total nutrient uptake (described below) and  $dtmin$  the minimum doubling time of the biomass. The same value of  $dtmin$  (0.5 d) is assigned in terms of carbon and nitrogen for both large and small phytoplankton to obtain light-based and nutrient-based maximum growth rates consistent with growth rate estimates in the GSL [e.g., *Tian et al.*, 2000; *Tamigneaux et al.*, 1997; *Sévigny et al.*, 1979]. The growth rate is set to 0 if one of the two doubling times exceeds 8.4 days [*Richardson et al.*, 1983]. Photosynthesis is described by a hyperbolic saturation curve [*Kiefer and Mitchell*, 1983] where  $E$  is the photosynthetically available radiation (PAR) experienced by phytoplankton. We assume that both phytoplankton size classes show the same response to light. The light field in the water column is computed through the classical Beer's law:

$$\text{Surface } z \text{ layer: } E = 0.45.(1 - IC).SW.[\exp^{-(k_w + k_p + k_{chla}).dz}], \quad (4)$$

$$\text{Subjacent } z \text{ layers: } E = E_{z-1}.[\exp^{-(k_w + k_p + k_{chla}).dz}], \quad (5)$$

With

$$k_{chla} = 0.0518.(CHLA^{-0.572}), \quad (6)$$

where  $IC$  is the seasonal sea ice cover percentage and  $SW$  the incident short wavelength irradiance at the sea surface used in the sea ice-ocean model. PAR representing about 40-50 % of the total incoming radiation at the sea surface [*Strickland*, 1958; *Morel*, 1988; *Kirk*, 1983], we assume the PAR to be 45 % of  $SW$ . Pure seawater properties ( $k_w$ ), nonchlorophyllous matter ( $k_p$ ) and phytoplankton self-shading ( $k_{chla}$ ) attenuate the PAR through depth. The self-shading attenuation coefficient is calculated from  $Chl\ a$

concentration following Morel's formulation [Morel, 1988] (Eqs. 5-6). At this stage, freshwater-induced turbidity due to transported nonchlorophyllous matter, known to affect light conditions in the LSLE [e.g., Sinclair, 1978; Nieke *et al.*, 1997], is not considered. Hence,  $k_p$  is set constant and adjusted to produce a maximum depth of the productive layer consistent with measured depths of the euphotic zone in the GSL [mostly 40-50 m; Doyon *et al.*, 2000].

The dissolved inorganic nitrogen uptake is computed using the substitutable model of O'Neill *et al.* [1989] for the two size classes of phytoplankton. It gives for large phytoplankton:

$$f(N)_{LP} = \frac{k_{4_{LP}} \cdot NO_3 + k_{3_{LP}} \cdot NH_4}{k_{4_{LP}} \cdot NO_3 + k_{3_{LP}} \cdot NH_4 + k_{4_{LP}} \cdot k_{3_{LP}}}, \quad (7)$$

$$NuNO_3_{LP} = \frac{k_{4_{LP}} \cdot NO_3}{k_{4_{LP}} \cdot NO_3 + k_{3_{LP}} \cdot NH_4}, \quad (8)$$

$$NuNH_4_{LP} = \frac{k_{3_{LP}} \cdot NH_4}{k_{4_{LP}} \cdot NO_3 + k_{3_{LP}} \cdot NH_4}, \quad (9)$$

where  $NuNO_3_{LP}$  and  $NuNH_4_{LP}$  are the nitrate and ammonium uptake fractions, respectively. Half-saturation constants for nitrate uptake are the same for both size classes. Nonetheless, ammonium is set to be the preferred inorganic nitrogen source [Dorch, 1990; Levasseur *et al.*, 1990] with a higher affinity for the small phytoplankton [Tremblay *et al.*, 2000]. This is expressed in the model by half-saturation constants for ammonium uptake significantly lower than for nitrate that, when used with the substitutable model of O'Neill *et al.* [1989], allow an inhibitory effect of ammonium on nitrate uptake as often observed [e.g., Dorch, 1990]. Phytoplankton losses include non-grazing mortality, grazing, and

sinking only for large algae. Non-grazing mortality in phytoplankton being poorly quantified, we set it to  $0.02 \text{ d}^{-1}$  for both size classes.

Formulations and parameters related to the mesozooplankton dynamics were chosen to reflect copepods since they widely dominate in abundance in the GSL [*de Lafontaine et al.*, 1991]. The mesozooplankton grazing is described by a modified Ivlev function [*Franks et al.*, 1986]:

$$gz_{MEZ} = gmax_{MEZ} \cdot iv_{MEZ} \cdot (LP + MIZ) \cdot [1 - \exp^{-iv_{MEZ} \cdot (LP + MIZ)}], \quad (10)$$

In contrast to the classical Ivlev function, this formulation shows a non-saturating response of the grazing rate for high prey levels. Its use permits to dampen predator/prey oscillations [e.g., *Franks et al.*, 1986], and thus, can provide stability to the planktonic ecosystem model forced by a highly changing physical environment. The mesozooplankton grazes on large phytoplankton and microzooplankton in the model, as it occurs in the GSL [*Ohman and Runge*, 1994], with a prey-specific grazing rate assumed to be proportional to the relative biomass of the prey. Because of their high variability ( $gmax_{MEZ} = 0.16-1.5 \text{ d}^{-1}$  and  $iv_{MEZ} = 0.1-2 \text{ (mmol N m}^{-3}\text{)}^{-1}$ ; e.g., *Franks et al.*, [1986]), parameters of the grazing function were chosen to generate a peak of mesozooplankton biomass that follows the peak of large phytoplankton biomass with a time lag of about two weeks, i.e., half a generation time. Losses in mesozooplankton biomass are due to ammonium release, fecal pellets production (non-assimilated food) and mortality. Mortality is assumed to be mainly due to predation [e.g., *Eiane et al.*, 2002] and is described by a density-dependant quadratic function. As opposed to the linear form, the use of a quadratic function may limit the occurrence of oscillations generated in such non-linear systems [*Edward and Brindley*,

1999; *Edwards and Yool, 2000; Edwards and Bees, 2001*]. The constant was set to 0.05 ( $\text{mmol N m}^{-3})^{-1}$  to produce mortality rates in the range of reported estimates [e.g., *Kiorbøe, 1998; Ohman et al., 2004*].

The grazing of the microzooplankton on small phytoplankton is formulated by a sigmoidal “Holling-type-III” function:

$$g_{Z_{MIZ}} = g_{\max_{MIZ}} \left( \frac{SP^2}{SP^2 + k_{MIZ}^2} \right), \quad (11)$$

This formulation provides a threshold-like limit for low biomass of prey which brings stability to the system [e.g., *Steele and Henderson, 1992*]. Its use is supported by the study of *Lancelot et al. [1997]* that shows that the protozooplankton exerts a control on the biomass of autotrophic flagellates only beyond a certain threshold. The microzooplankton is known to be a major component of nitrogen recycling in marine systems [*Caron and Goldman, 1990*]. Following the study of *Riegman et al. [1993]*, we set to 30 % the fraction of food ingested by the microzooplankton becoming biomass. *Lehrter et al. [1999]* reported that 26-27 % of the total nitrogen release of microzooplankton can be in the dissolved organic form. Assuming a value of 30 % in the model, it results that 21 % of the food ingested is released as DON. The remaining 49 % is lost as ammonium [e.g., *Anderson, 1992*]. Other loss terms of the microzooplankton component are senescence and grazing by mesozooplankton. Similarly to phytoplankton, non-grazing mortality was set to  $0.02 \text{ d}^{-1}$ .

Fecal pellets production, and mesozooplankton and large phytoplankton mortality increase the PON concentration. The PON equation allows for its sedimentation and includes a fragmentation term into DON [e.g., *Gowing and Silver, 1983; Grossart and*

*Ploug, 2001*]. The sinking material that leaves the last active layer in the model is assumed to be definitely trapped into the sediment. Finally, the ammonification of DON, considered here as the labile fraction, contributes to fuel the regenerated primary production [e.g., *Berman et al., 1999*]. In the GSL, the dissolved organic carbon (DOC) remineralization rates have been reported to vary between 0.01 and 0.4 d<sup>-1</sup> [*Packard et al., 2001*]. Assuming a faster overturning of DON vs DOC, we set its decay rate to 0.4 d<sup>-1</sup>.

**III. APPLICATION OF REMOTELY SENSED SEA COLOR AND  
TEMPERATURE DATA FOR MESOSCALE AND REGIONAL  
VALIDATION OF A 3-D HIGH-RESOLUTION PHYSICAL-  
BIOLOGICAL COUPLED MODEL OF THE GULF OF ST.  
LAWRENCE (CANADA): THE CHALLENGE OF INLAND WATERS**

## ABSTRACT

We present here a first attempt to validate a regional three-dimensional (3-D) physical-biological coupled model of the Gulf of St. Lawrence with coincident advanced very high resolution radiometer (AVHRR)-derived sea surface temperature (SST) and Sea-viewing Wide Field-of-View Sensor (SeaWiFS)-derived chlorophyll *a* (Chl-*a*) data. The analysis focuses on comparisons between remotely sensed data and simulated sea temperature, Chl-*a*, and freshwater-associated turbidity. The results show that the simulated and AVHRR-derived fields of SST are qualitatively and quantitatively in agreement and close to space and time coincident *in situ* measurements. By contrast, marked differences are found between the simulated and SeaWiFS-derived fields of Chl-*a*, the latter comparing better with the freshwater-associated turbidity simulated by the model. Since the sea temperature, salinity, nitrate, and Chl-*a* simulated by the coupled model compare well with space and time coincident *in situ* measurements, it is then suggested that freshwater-associated turbidity related to the river discharges largely contributes to the Chl-*a* retrievals by SeaWiFS in the gulf's waters when using the standard OC4v.4 algorithm and atmospheric correction. Nevertheless, we show that SeaWiFS-derived ocean colour data can be used to track the regional estuarine circulation and associated mesoscale variability. This result brings support to the model's ability to produce realistic physical and biogeochemical fields in the Gulf of St. Lawrence.

## INTRODUCTION

The Gulf of St. Lawrence (hereafter GSL) is a highly dynamic sub-arctic marginal sea characterized by a marked synoptic wind forcing, a freshwater runoff of  $350 \text{ km}^3 \text{ yr}^{-1}$  from the St. Lawrence watersheds, and an intense tidal mixing [e.g., *Koutitonsky and Bugden*, 1991]. The large variability of atmospheric, hydrologic, and oceanic forcings leads to the formation of eddies, upwellings and density fronts that superimpose on the mean estuarine-like circulation induced by the freshwater runoff from the St. Lawrence River and other tributaries [e.g., *Koutitonsky and Bugden*, 1991; *Saucier et al.*, 2003]. The chief importance of hydrographic processes on the planktonic ecosystem's dynamics has long been established [e.g., *Steven*, 1974; *Therriault and Levasseur*, 1985; *de Lafontaine et al.*, 1991] and recently more precisely apprehended using a 3-D high-resolution physical-biological coupled model [*Le Fouest et al.*, 2003, 2005]. Simulated and *in situ* nitrate and chlorophyll *a* (Chl *a*) concentrations were successfully compared for 1997, providing a detailed quantitative demonstration of the model's ability to generate a consistent seasonal cycle of primary production. Furthermore, the model revealed that the intense mesoscale variability prevailing in the GSL should be as important as the seasonal variability for the annual primary production [*Le Fouest et al.*, 2005].

Inferring this mesoscale variability and its impact on phytoplankton distribution and dynamics is a difficult if not an unreachable task with ship-based field experiments alone. Polar-orbiting satellites may help to fill the gap by allowing a synoptic view of sea surface temperature (SST) and pigments with a resolution both in space (up to 1 km) and time

(daily) and are now routinely used to quantify and characterize the mesoscale variability in open ocean waters [e.g., *McGillicuddy et al.*, 2001; *Doney et al.*, 2003; *Metz Uz and Yoder*, 2004]. Previous studies of *Fuentes-Yaco et al.* [1997ab], using Coastal Zone Color Scanner (CZCS)-derived Chl *a* data, as well as *Tang* [1980b] and *Gratton et al.* [1988], using Advanced Very High Resolution Radiometer (AVHRR)-derived SST, have shown the prime importance of the mesoscale to synoptic variability of the oceanographic conditions in the GSL. An exhaustive analysis of monthly-composited Sea-viewing Wide Field-of-View Sensor (SeaWiFS)-derived Chl *a* data between 1997 and 2001 [*Gower*, 2004] also revealed the occurrence of peculiar phytoplankton production events in the GSL. Such events may be related to the mesoscale variability of the circulation but the monthly time-averaging applied to produce composite images such as in *Gower* [2004] precludes a detailed validation of the mesoscale variability. Moreover, the complex optical properties of coastal waters limit the ability of the standard SeaWiFS algorithm (OC4v.4) to adequately retrieve Chl *a* concentrations due to the presence of terrestrial CDOM [e.g., *Carder et al.*, 1989; *Darecki and Stramski*, 2004; *Gohin et al.*, 2002; *Wang and Cota*, 2003, *Berthon and Zibordi*, 2004; *Harding et al.*, 2005] and suspended sediments [e.g., *Toole and Siegel*, 2001; *Wozniak and Stramski*, 2004]. Regional empirical algorithms based on *in situ* data have been developed to improve the remotely sensed Chl *a* retrieval in these so-called Case 2 waters [e.g., *Tassan*, 1994; *Kahru and Mitchell*, 2001; *Binding et al.*, 2003; *Magnuson et al.*, 2004] but none is yet operational for the GSL waters. However, confidence can be addressed to the spatial gradients of SeaWiFS-derived Chl *a* to infer

qualitatively the physical-biological coupling in coastal and shelf seas [e.g., *Oguz et al.*, 2002; *Pegau et al.*, 2002; *Stegmann and Ulman*, 2004].

We present here a first attempt to validate solutions of the regional 3-D physical-biological coupled model of the GSL using AVHRR-derived SST and SeaWiFS-derived Chl *a* data. A model simulation for the year 1998, following the initial calibration made for the previous year in *Le Fouest et al.* [2005], now accounts for freshwater-associated turbidity known to affect the optical properties of the Gulf's waters [*Nieke et al.*, 1997] through chromophoric dissolved organic matter (CDOM) drained by the freshwater runoff. The analysis is made by comparing 5 synoptic short-term composites (one in spring, three in summer, and one in fall) of remotely sensed SST and Chl *a* with the corresponding simulated fields of SST, Chl *a* concentration, and freshwater-associated turbidity. Both remotely sensed and simulated fields are evaluated in reference to independent *in situ* observations made the same year in the framework of current monitoring and research programs in the GSL. The accuracy of the 3-D physical-biological coupled model in predicting the mesoscale variability and the contribution of the freshwater-associated turbidity on the simulated and remotely sensed Chl *a* distribution are investigated in this study.

## METHODS

### 1. *The 3-D physical-planktonic ecosystem model*

For a detailed description of the sea ice-ocean coupled model, the readers are referred to *Saucier et al.* [2003], whereas the latest improvements in the turbulent mixing and sea ice dynamics modelling are described in *Saucier et al.* [2004]. We will review here the main model characteristics with a focus on the high-resolution forcings upon which mesoscale activity strongly depends. The numerical domain extends from Cabot Strait and Strait of Belle-Isle to the upper limit of the tidal influence near Montreal with a lateral resolution of 5 x 5 km (Figure III-1). The cell thickness is 5 m from the surface to 300 m depth and 10 to 20 m below, with free surface and bottom layers adjusted to sea level and topography, respectively. The shallow water and tracer conserving ocean model is hydrostatic and complemented with a level 2.5 turbulent kinetic energy equation [see *Saucier et al.*, 2004]. It is coupled to a dynamic and thermodynamic two-layer sea ice and one-layer snow cover model [*Thorndike et al.*, 1975, *Semtner*, 1976; *Hunke and Dukowicz*, 1997]. Bulk aerodynamic exchange formulas govern the heat fluxes between the ocean, sea ice and lower atmosphere. Three-hourly atmospheric forcings are provided by the Canadian Operational Weather Forecast Model and include surface air temperature, dew point depression, surface winds, cloudiness, precipitation and surface pressure. The model is also driven by monthly and daily runoff data of the St. Lawrence River and 28 main tributaries, respectively, and hourly water levels (co-oscillating tides) and monthly mean temperature and salinity prescribed at the Cabot Strait and Strait of Belle-Isle.



The planktonic ecosystem model coupled to the sea ice-ocean model is described in detail in *Le Fouest et al.* [2005] and can be schematized as follow: the export at depth of the biogenic matter is mediated by the herbivorous food web (nitrate; large phytoplankton [ $> 5 \mu\text{m}$ ]; mesozooplankton [200-2000  $\mu\text{m}$ ]; particulate organic matter) while the microbial food web (ammonium; small phytoplankton [ $< 5 \mu\text{m}$ ]; microzooplankton [20-200  $\mu\text{m}$ ]; dissolved organic matter) is mainly responsible for nutrient recycling in the euphotic zone. This size-fractionated approach for planktonic trophic pathways has implications in the carbon export [e.g., *Legendre and Le Fèvre*, 1995; *Legendre and Michaud*, 1998; *Legendre and Rivkin*, 2002]. Biological transfer functions (e.g., phytoplankton growth rate, grazing and remineralization) were derived from generic formulations and using mean parameters found in the literature [see *Le Fouest et al.*, 2005]. Biological variables are calculated in  $\text{mmol N m}^{-3}$  and algal biomass is converted in Chl *a* units using a molar C/N ratio of 106/16 [*Redfield et al.*, 1963] and a C/Chl *a* mass ratio of 55 [*Sinclair*, 1978; *Rivkin et al.*, 1996]. *In situ* nitrate and Chl *a* fields of fall 1997 from the Atlantic Zone Monitoring Program [AZMP; *Therriault et al.*, 1998] database were used to set the initial and boundary conditions of the model. Monthly climatological means of *in situ* nitrate and Chl *a* concentration (Chifflet M, unpublished results) were prescribed at Cabot Strait and the Strait of Belle-Isle.

The model of light attenuation in the water column follows the Beer-Lambert's law and includes the diffuse attenuation by pure sea water, Chl *a*, and nonchlorophyllous matter. Freshwater-associated turbidity is accounted for through the diffuse attenuation coefficient for nonchlorophyllous matter ( $k_p$ ) that is set to vary with salinity. This

formulation finds support in the inverse linear relationship that links CDOM absorption coefficient to salinity in the GSL [Nieke *et al.*, 1997] and other coastal waters [e.g., Ferrari and Dowell, 1998; Kowalczyk, 1999; Siddorne *et al.*, 2001; Keith *et al.*, 2002; D'Sa and Miller, 2003]. This simulated bulk turbidity is then assumed to be mainly associated to CDOM of terrestrial origin without *in situ* degradation. The linear equation between  $k_p$  and salinity (Figure III-2) was derived from *in situ* data (salinity, Chl *a*, and total attenuation coefficient) obtained from four SeaWiFS validation cruises conducted in fall 1997-1998, summer 1999, and spring 2001 for a total of 63 stations covering the whole Estuary and Gulf. The values of  $k_p$  are calculated by subtracting the attenuation coefficient due to Chl *a* (see eq. 6 in Le Fouest *et al.*, 2005) and the attenuation coefficient for pure seawater (set to  $0.04 \text{ m}^{-1}$ ; Morel, 1988) from the measured total attenuation coefficient. The linear equation ( $k_p = -0.0364 \text{ Salinity} + 1.1942$ ), is closed in the model by two salinity thresholds at 26 ( $k_p = 0.25 \text{ m}^{-1}$ ) and 32 ( $k_p = 0.03 \text{ m}^{-1}$ ).

## 2. Remotely sensed and *in situ* data

The SeaWiFS High-Resolution Picture Transmission (HRPT) and Merged Local Area Coverage (MLAC) level-1 raw data used in this study are distributed by the Goddard Space Flight Center (NASA). Level-2 sea surface Chl *a* concentrations were computed from level-1 data using the OC4v.4 algorithm [O'Reilly *et al.*, 1998] provided by the SeaWiFS Data Analysis Software (SeaDAS) version 4.5. The composites were constructed with the two following constraints: a full Gulf coverage over a short time (less than one week, except in autumn due to greater cloud cover) and marked mesoscale patterns in SST

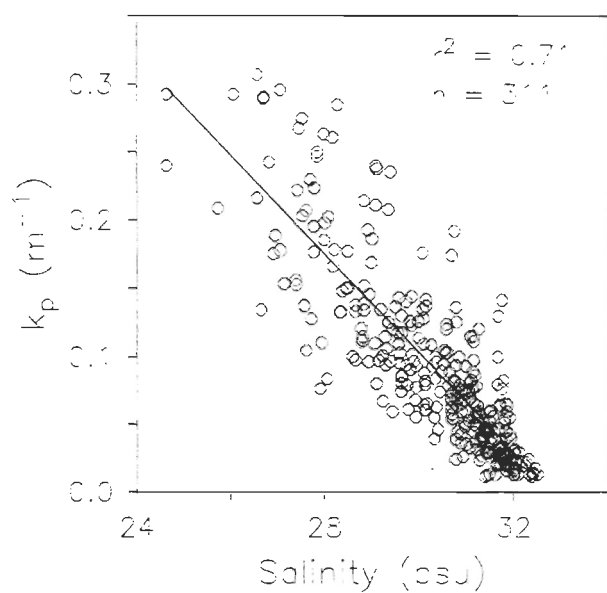


Figure III-2. Scatter plot showing the linear relationship between salinity and the attenuation coefficient due to nonchlorophyllous matter ( $k_p$ ) derived from *in situ* measurements. The linear regression gives the equation  $k_p = -0.0364 \text{ Salinity} + 1.1942$  with a correlation coefficient of  $r^2 = 0.71$ .

and Chl *a* fields. Given these constraints, we obtain five composite datasets (Table III-1) covering spring (1), summer (3) and fall (1) of 1998. Level-2 data were binned to obtain level-3 composites mapped on 4 x 4 km Mercator grids, each spanning 4 to 9 days. High resolution (1 x 1 km) SST images were provided by the Maurice-Lamontagne Institute (Fisheries and Oceans, Mont-Joli, Quebec, Canada). A TeraScan direct downlink station (48.38N, 68.09W) acquires the infrared imagery data from AVHRR instruments aboard polar-orbiting NOAA satellites. The raw images are processed using the SeaSpace package and the SST calculated using the multi-channel sea surface temperature algorithm [MCSST, *Bernstein*, 1982; *McClain et al.*, 1985]. The individual passes (up to 7 per day) were processed to produce SST composites corresponding to the SeaWIFS level-3 data by way of a simple averaging. Satellite-derived 2D fields were finally interpolated (Gaussian interpolation) on the ocean model grid cells of 5 x 5 km for the comparisons.

The model solutions and satellite-derived data are both compared with independent *in situ* datasets including SST measured by permanently moored instruments, temperature, salinity and nitrate and Chl *a* bottles measurements from the AZMP database for the June 12<sup>nd</sup>-18<sup>th</sup> and November 4<sup>th</sup>-13<sup>rd</sup>, 1998 cruises and three bimonthly monitored stations, as well as Chl *a* bottles measurements from the October 25<sup>th</sup>-November 2<sup>nd</sup>, 1998 SeaWIFS validation cruise (Figure III-3). Simulated temperature, Chl *a*, and nitrate were sampled for the yearlong prognostic simulation at the same time and location as the field measurements and, when needed, were interpolated to the bottle depths. Over a total of 162 locations sampled during the 1998 cruises, only 35 time and space match-up points with the SeaWIFS data were reported. Mean ratio, root mean square (RMS) error and the mean

Table III-1. Time periods and number of images used to build the AVHRR and SeaWIFS composites.

Composite time periods	Number of images	
	SeaWIFS	AVHRR
June 7 <sup>th</sup> -11 <sup>st</sup> , 1998	5	14
July 2 <sup>nd</sup> -8 <sup>th</sup> , 1998	6	24
August 3 <sup>th</sup> -6 <sup>th</sup> , 1998	4	15
August 28 <sup>th</sup> -September 2 <sup>nd</sup> , 1998	6	14
October 6 <sup>th</sup> -14 <sup>th</sup> , 1998	9	11

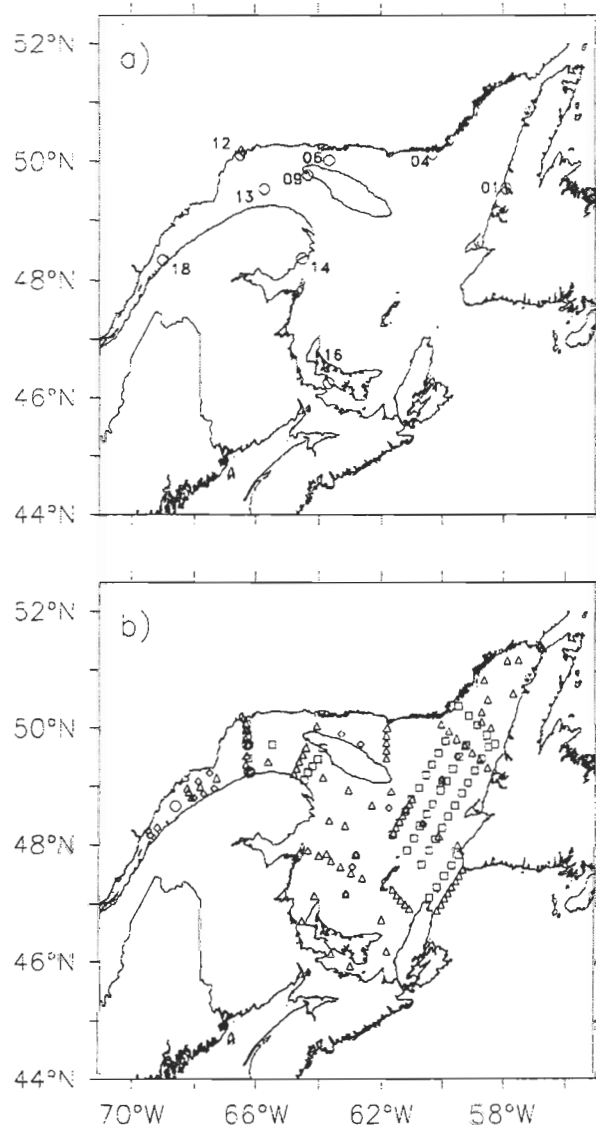


Figure III-3. Positions of the (a) permanently moored thermometers, (b) sampling stations visited in 1998: AZMP cruises in June (squares) and November (triangles), the fixed AZMP stations (circles), and the SeaWIFS validation cruise in October-November (rhombuses).

relative difference (MRD) were used to quantify the differences between *in situ*, remotely sensed, and simulated data. The mean ratio was calculated as the arithmetic mean of the  $n$  individual simulated to observed (either remotely sensed or *in situ*) values. The MRD and RMS error were calculated as following:

$$\text{MRD} = \sum[(X_{\text{obs}} - X_{\text{mod}})/X_{\text{obs}}]/n \quad (1)$$

$$\text{RMS} = [(\sum(X_{\text{obs}} - X_{\text{mod}})^2)/n]^{0.5} \quad (2)$$

where  $X_{\text{obs}}$  and  $X_{\text{mod}}$  are observed (*in situ* or remotely sensed) and simulated values, respectively. The RMS error reflects the deviation between the two data sets while the relative difference indicates an overestimation or an underestimation of the observed values. For comparisons between *in situ* and remotely sensed values, we assume the former to be the observed value.

## RESULTS AND DISCUSSION

### 1. *Simulated and AVHRR-derived SST*

Surface temperature gradients produced by the model and AVHRR-derived are overall qualitatively and quantitatively in agreement (Figures III-4-8). The main regional pattern evidenced by both the model and the AVHRR-derived data is the vernal warming of the Magdalen Shallow (hereafter MS, 75 m deep in average) surface waters that contrasts with the colder northeastern GSL (hereafter NEG) and Lower St. Lawrence Estuary (LSLE). While more marked in summer, this pattern remains conspicuous on both simulated and remotely sensed SST fields in all composites. Surface simulated ( $SST_{sim}$ ) and AVHRR-derived temperatures ( $SST_{sat}$ ) are close throughout the year with a mean ratio of 1.15 (Figure III-9a) except in summer on the MS and the Northumberland Strait when the  $SST_{sat}$  can be substantially higher than the  $SST_{sim}$ . The autumn cooling of the surface waters is well illustrated by the  $SST_{sat}$  and  $SST_{sim}$  that reach levels comparable to those reported for the spring season (Figures III-4 and III-8). The model also captures periodic and episodic events retrieved by the AVHRR instrument. One of these is the tidally-induced upwelling at the head of the Laurentian Channel which is a characteristic feature of the LSLÉ [e.g., Gratton *et al.*, 1988]. It is illustrated on both simulated and remotely sensed SST fields by a permanent cold spot in the upper LSLÉ, downstream of the mouth of the Saguenay River, contrasting with the warmer surface waters downstream. The model also reproduces wind-induced upwelling events along the south coast of the Anticosti Island and

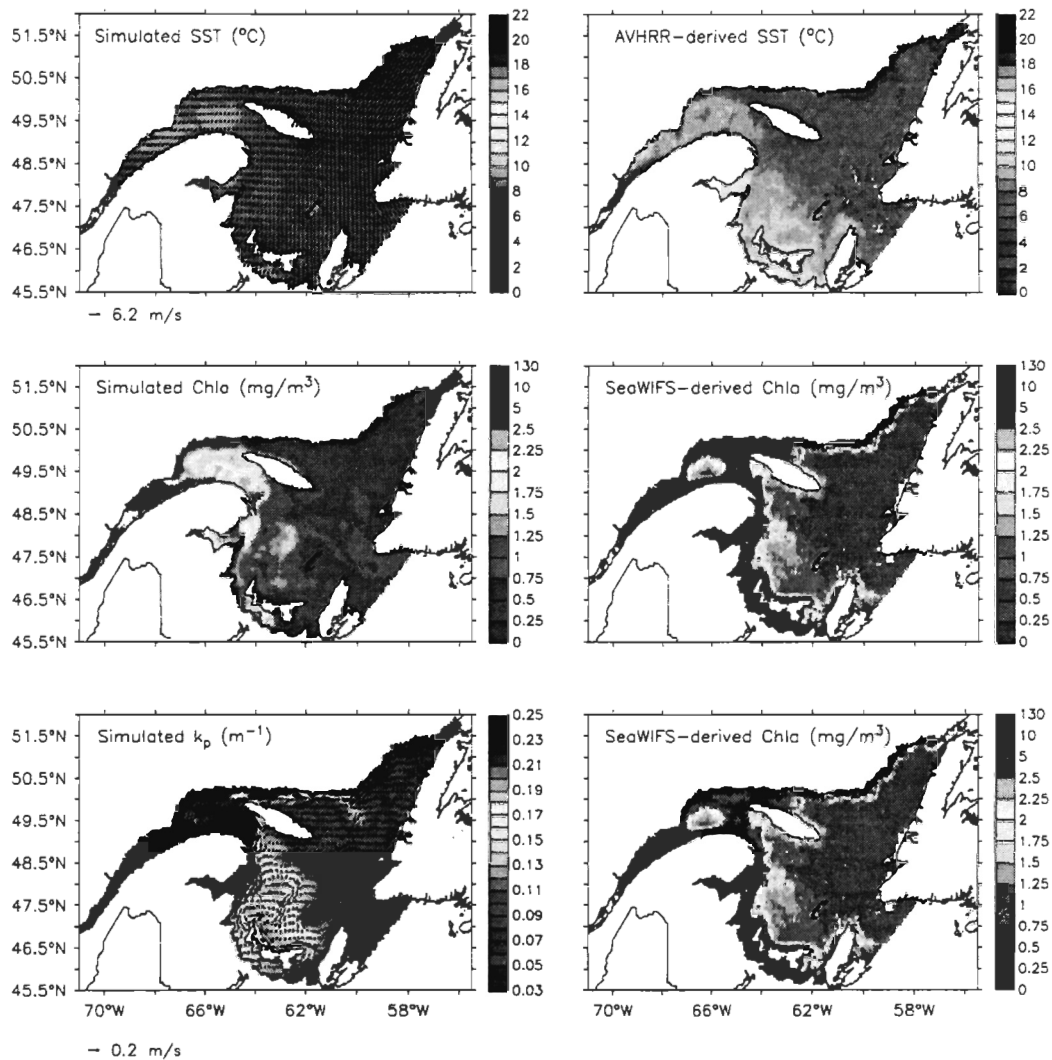


Figure III-4. Comparisons of satellite-derived fields of SST and surface Chl *a* to simulated SST (5 m), Chl *a* (depth-averaged 0-10 m), and attenuation coefficient due to nonchlorophyllous matter ( $k_p$ ) for the June 7<sup>th</sup>-11<sup>st</sup> period. The mean simulated fields of surface wind and depth-averaged (0-10 m) current are overlaid on the mean simulated SST and Chl *a* fields, respectively.

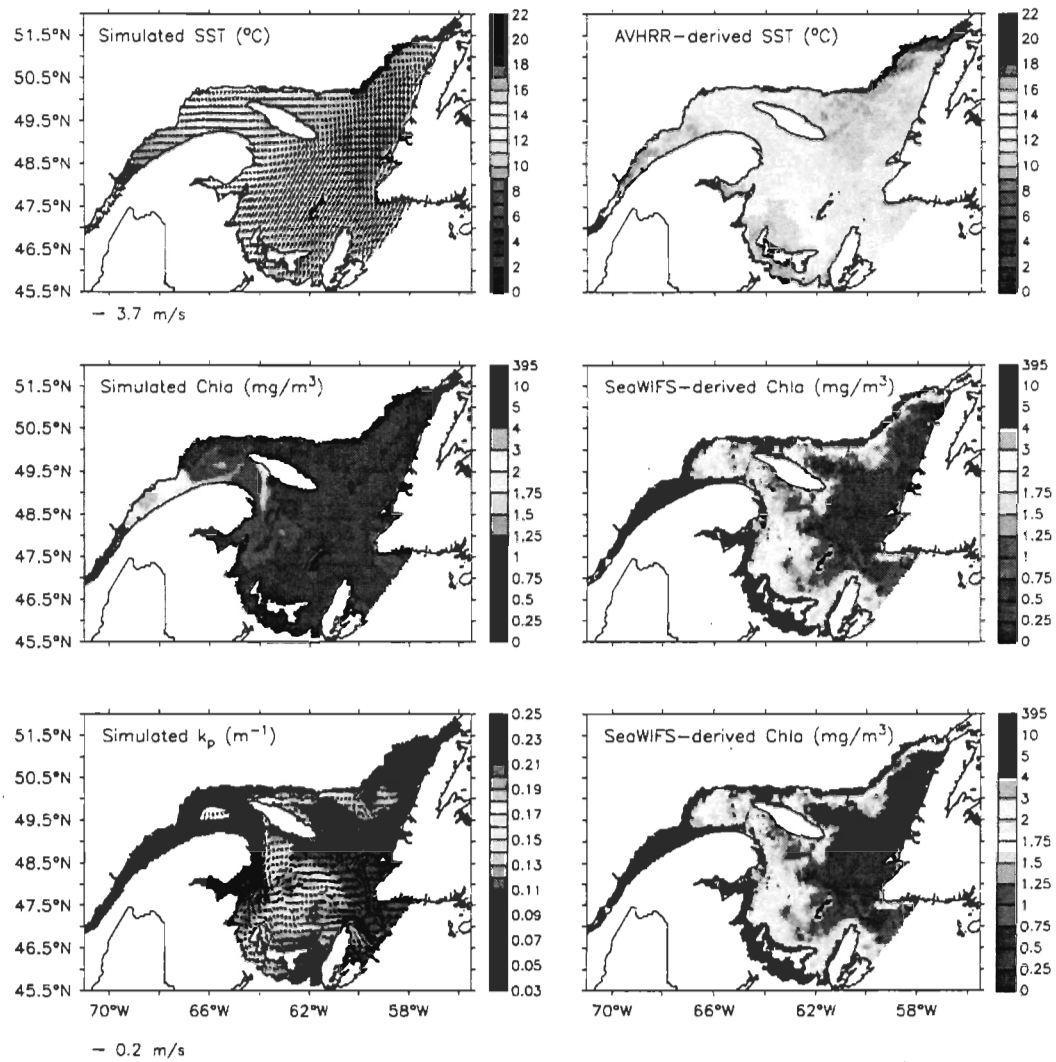


Figure III-5. Same as Figure III-4 for the July 2<sup>nd</sup>-8<sup>th</sup> period.

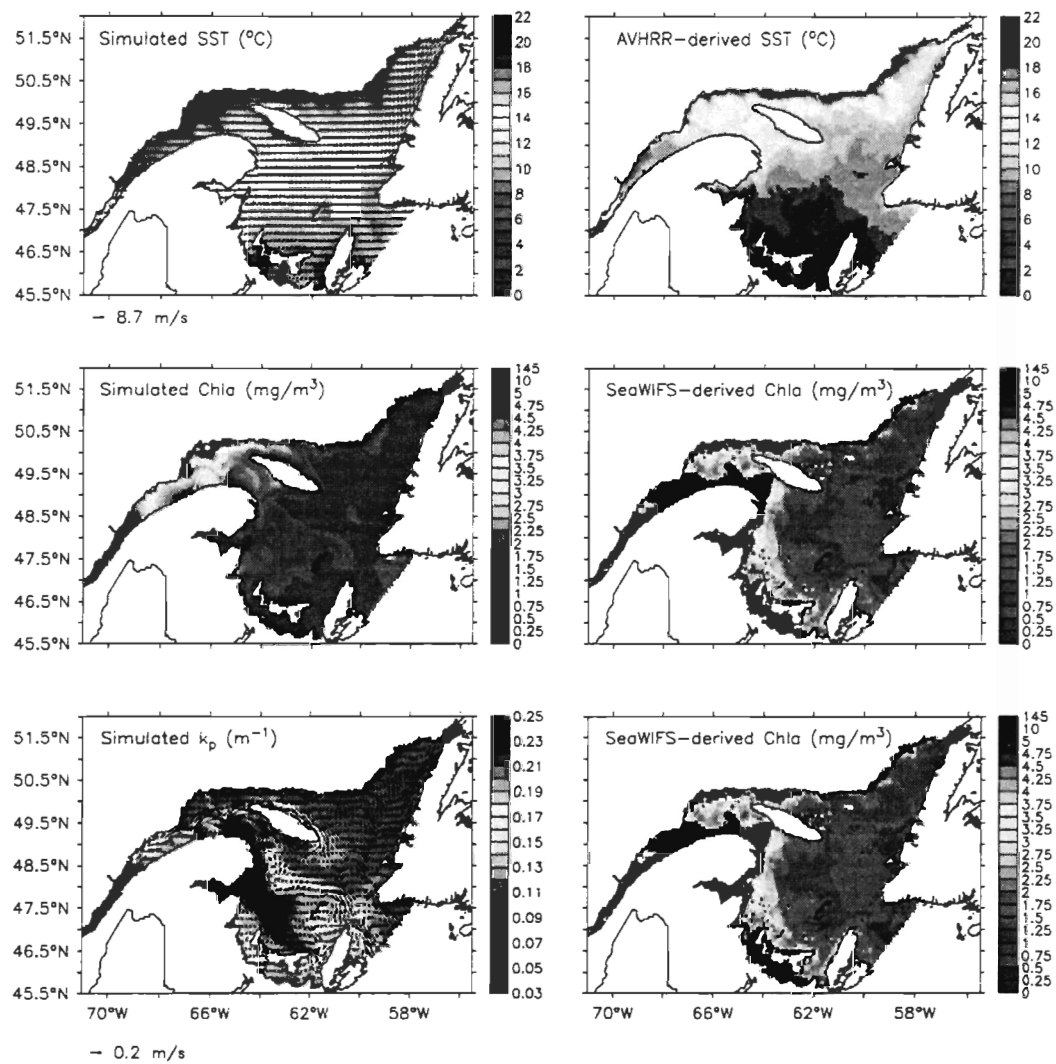


Figure III-6. Same as Figure III-5 for the August 3<sup>rd</sup>-6<sup>th</sup> period.

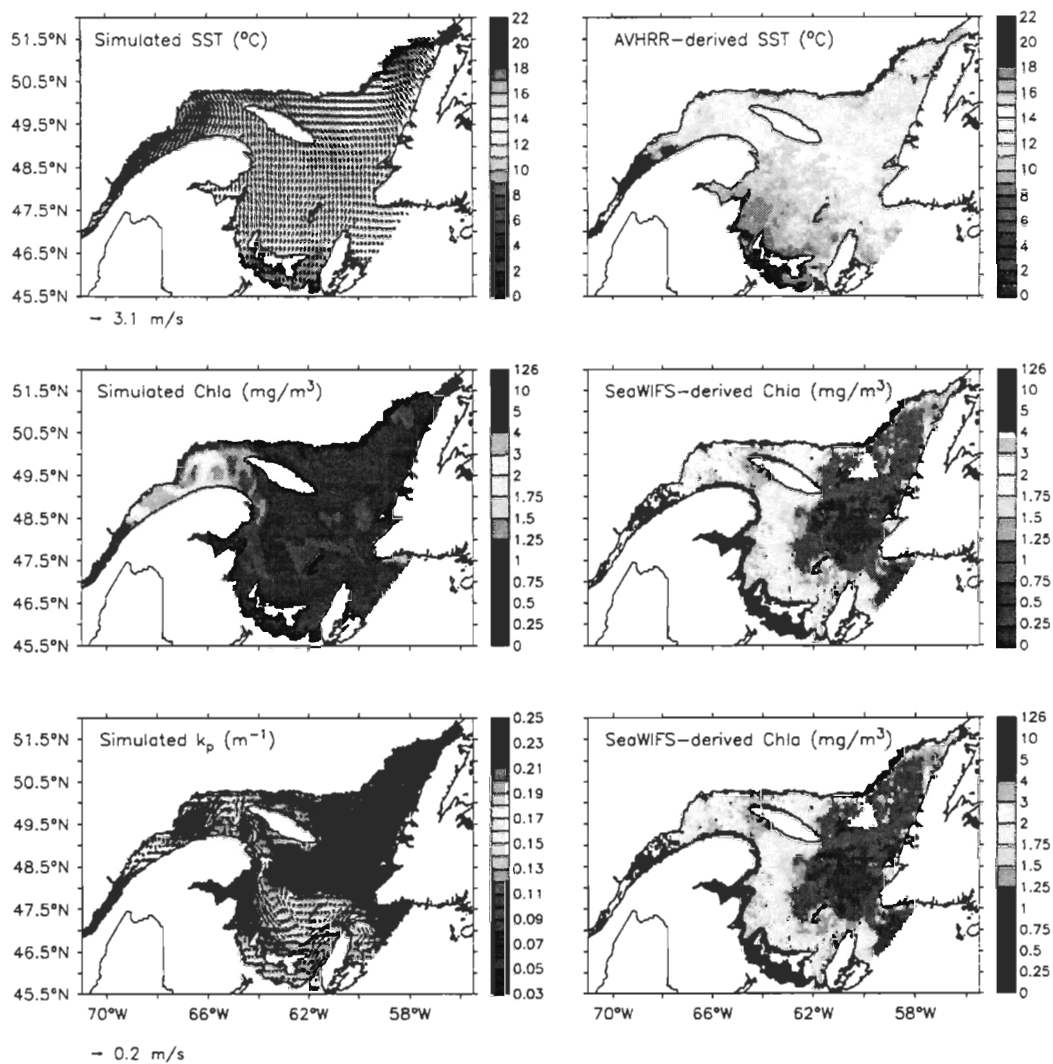


Figure III-7. Same as Figure III-6 for the August 28<sup>th</sup>-September 2<sup>nd</sup> period.

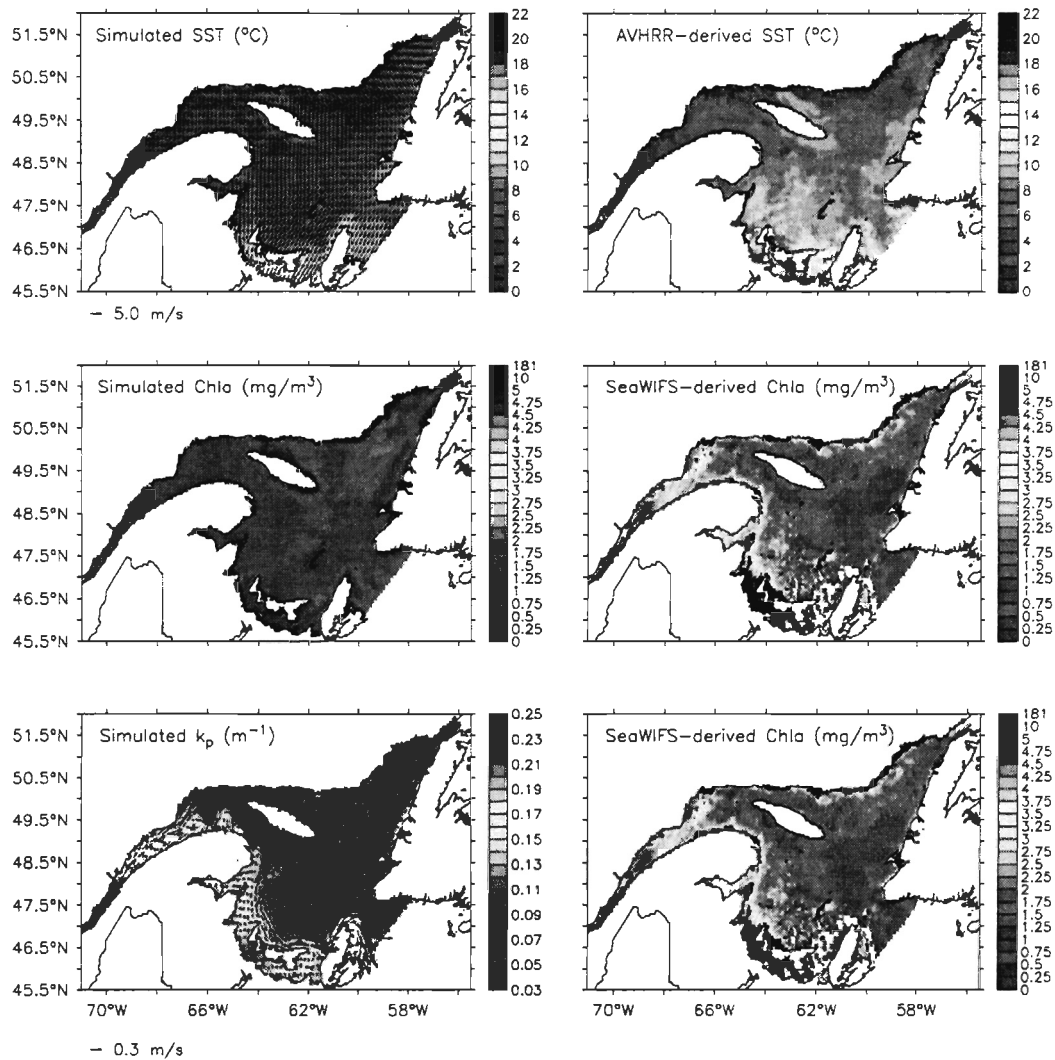


Figure III-8. Same as Figure III-7 for the October 6<sup>th</sup>-14<sup>th</sup> period.

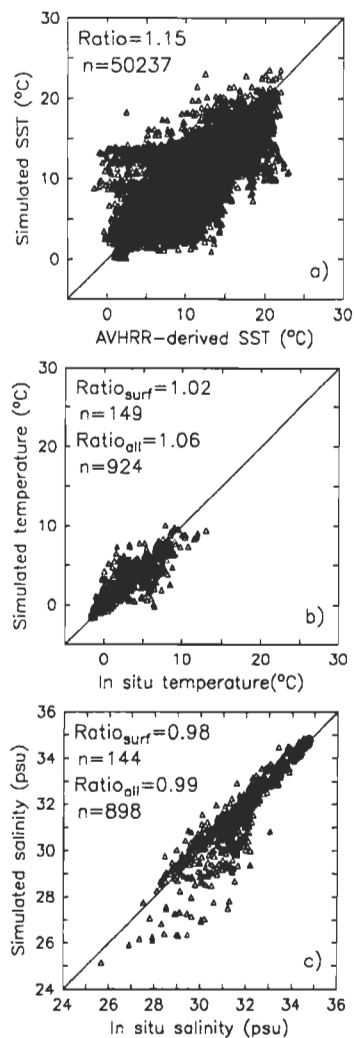


Figure III-9. Comparison of simulated SST with (a) AVHRR-derived SST and (b) *in situ* SST, and (c) comparison of *in situ* and simulated salinity. *In situ* data include measurements made in 1998 from the AZMP June and November cruises and three fixed stations (see text). In panels (b) and (c), surface values are in red whereas deeper values are in black (the whole water column).

the north shore (hereafter NS) in August 3<sup>rd</sup>-6<sup>th</sup>, such as evidenced by strong SST gradients on both the simulated and remotely sensed fields (Figure III-6). In October 6<sup>th</sup>-14<sup>th</sup>, the persistent fringe of cold water (2-5°C) along the NS coincides with upwelling-favourable winds of 15 to 20 m s<sup>-1</sup> prevailing over the two previous days (October 3<sup>rd</sup>-5<sup>th</sup>). The tongue of cold surface water produced by the model in the Unguedo Strait (hereafter USt) (Figure III-8) is associated to a strong current shear between the Gaspé Current and the wind-induced circulation along the south shore of the Anticosti Island. This frequently occurring pattern, already described in *Le Fouest et al.* [2005], is remarkably similar to the SST<sub>sat</sub> field.

All periods accounted, the RMS error between SST<sub>sat</sub> and SST<sub>sim</sub> is 2.45°C, and the MRD is 5.71 % indicating lower SST<sub>sim</sub> than SST<sub>sat</sub> (Table III-2). For the August 3<sup>rd</sup>-6<sup>th</sup> composite, the RMS error and MRD are 3.56°C and 18.55 %, respectively, being the highest of all composites (Table III-2). By contrast with the spring and summer periods, the negative MRD reported in October (-10.56 %) indicates higher SST<sub>sim</sub> than SST<sub>sat</sub> (Table III-2). The comparisons of the simulated temperature and salinity with *in situ* data provided better results with mean ratios close to 1 (Figure III-9bc) and lower RMS and MRD (Table III-3). The RMS errors are lower for salinity than for temperature (0.7-1.05 PSU and 1.31-1.41°C, respectively) while the MRD suggest a slight overestimation (-0.54 % to -4.14 %) for both variables. But both the MRD and the RMS error for temperature are significantly lower than the values calculated between the AVHRR-derived SST and simulated SST.

Table III-2. Root mean square (RMS, °C) error and mean relative difference (MRD, %) calculated between the AVHRR-derived and simulated SST (n=50237). Coincident points for each time period are shown in parentheses.

	All time periods	June 7 <sup>th</sup> -11 <sup>st</sup> (9995)	July 2 <sup>nd</sup> -8 <sup>th</sup> (10090)	August 3 <sup>rd</sup> -6 <sup>th</sup> (10109)	August 28 <sup>th</sup> - September 2 <sup>nd</sup> (10097)	October 6 <sup>th</sup> -14 <sup>th</sup> (9946)
RMS	2.45	1.58	1.64	3.56	2.56	2.37
MRD	5.71	7.19	4.1	18.55	9.04	-10.57

Table III-3. Root mean square (RMS) error and mean relative difference (MRD, %) calculated between the *in situ* (bottle measurements) and simulated temperature, salinity, nitrate and Chl *a*. Numbers of sampling are shown in parentheses.

	Temperature (°C)		Salinity (PSU)		Nitrate (mmol m <sup>-3</sup> )		Chl <i>a</i> (mg m <sup>-3</sup> )	
	Surface (149)	All depths (924)	Surface (144)	All depths (898)	Surface (140)	All depths (817)	Surface (183)	All depths (817)
RMS	1.31	1.41	1.05	0.7	2.09	2.94	1.62	1.61
MRD	-4.14	-2.85	-1.85	-0.54	-2.39	-41.62	-86.43	-206.3

In order to complete the analysis,  $SST_{sat}$  and  $SST_{sim}$  were plotted against *in situ* SST records from permanently moored instruments (Figure III-10). Data were sampled at the position of each thermometer whose temperature records were averaged over time periods corresponding to the composite images. Both mean ratios are near the 1:1 line but the  $SST_{sat}$  are closer (0.96) to the observations than the  $SST_{sim}$  (0.85). The RMS error indicates that both  $SST_{sim}$  and  $SST_{sat}$  show comparable dispersion in reference to *in situ* temperature (2.56°C and 2.40°C, respectively, Table III-4). The MRD of 14.42 % and 3.72 % associated to the  $SST_{sim}$  and  $SST_{sat}$ , respectively, suggest a greater underestimation of the *in situ* SST records by the model. For the early August composite (3<sup>rd</sup>-6<sup>th</sup>), the MRD indicates a higher underestimation by the model (27.4 %) and a minor overestimation by the satellite (-4.7 %). In late summer, the overestimation of the *in situ* SST by the satellite is the highest (-13.3 %; Table III-4) while in autumn the MRD suggests an underestimation by the satellite substantially higher (39 %) than for the model (10.5 %). Overall, the results show an overall good agreement of the simulated temperature with both *in situ* (all depth) and remotely sensed surface temperature. The differences found in the comparison criterias (RMS, MRD and ratios), showing a better agreement with *in situ* data, suggest the importance of the aliasing effects between synoptic events and the sampling scheme used in producing the composite satellite solutions. In addition, high-frequency (hourly) comparisons between  $SST_{sim}$  and *in situ* SST recorded by the same thermometers (Figure III-11) bring support to the ability of the model to capture both the seasonal and synoptic variability of the heat cycle in surface waters.

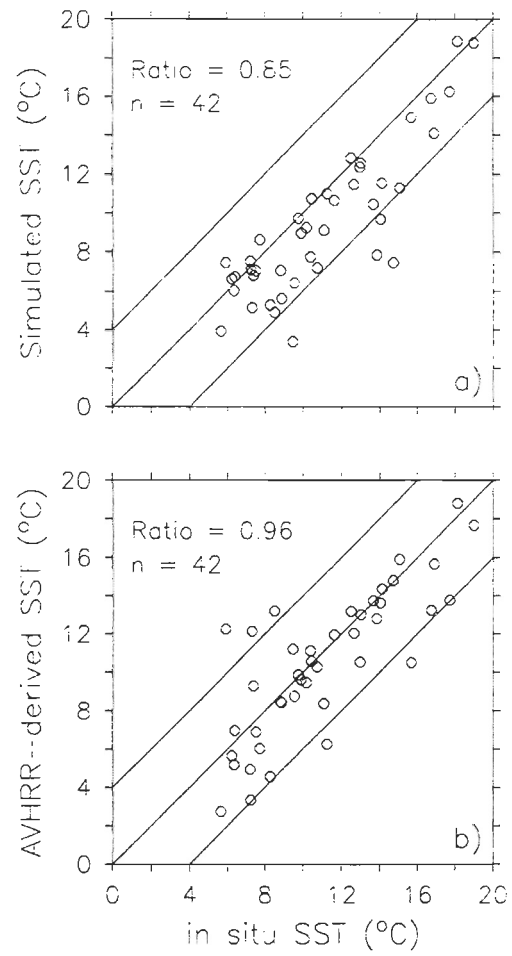


Figure III-10. Comparisons of *in situ* SST to (a) simulated SST and (b) AVHRR-derived SST.

Table III-4. Root mean square (RMS, °C) error and mean relative difference (MRD, %) calculated between the *in situ* (moored thermometers) and simulated or AVHRR-derived SST (n = 42). Coincident points for each time period are shown in parentheses.

		All time periods	June 7 <sup>th</sup> -11 <sup>st</sup> (8)	July 2 <sup>nd</sup> -8 <sup>th</sup> (9)	August 3 <sup>rd</sup> -6 <sup>th</sup> (9)	August 28 <sup>th</sup> September 2 <sup>nd</sup> (9)	October 6 <sup>th</sup> -14 <sup>th</sup> (7)
RMS	AVHRR	2.4	0.91	1.51	2.24	3.19	3.34
	Model	2.56	1.36	2.13	3.63	3.05	1.55
MRD	AVHRR	3.72	0.8	4.4	-4.7	-13.3	39
	Model	14.42	9.8	12.7	27.4	10.2	10.5

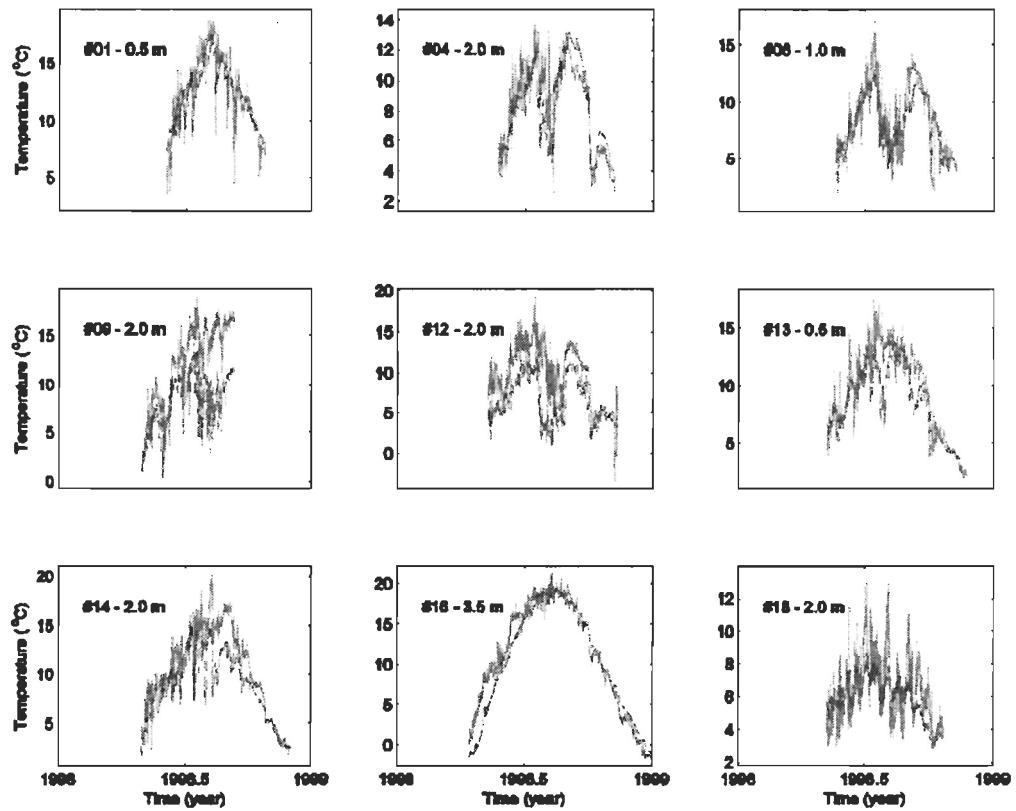


Figure III-11. Time series of hourly temperature records from permanently moored thermometers (in blue) compared to simulated temperature at the corresponding layer (in red). The number of the instrument (see Figure III-3a) and the record depth appear on each panel.

## 2. Turbidity, simulated and SeaWIFS-derived surface Chl *a*

Both simulated and remotely sensed fields of Chl *a* exhibit a regional East-West gradient, with higher values in the LSLE and northwestern GSL (hereafter NWG) (Figures III-4-8), known to be more productive subregions than the eastern GSL [e.g., *de Lafontaine et al.*, 1991]. However, they show striking differences in their spatial patterns and ranges of values, especially in the western GSL, along the Gaspé Peninsula, and on the western MS where SeaWIFS-derived Chl *a* (hereafter Chl<sub>sat</sub>) estimates can be two orders of magnitude higher than the simulated Chl *a* (hereafter Chl<sub>sim</sub>) concentrations (Figure III-12a). Averaging errors over the all available observations, the mean difference between the two fields is nearly half the Chl<sub>sat</sub> estimate (MRD of 47 %, Table III-5). The dispersion is substantial reaching a bloom-like value (4.8 mg Chl *a* m<sup>-3</sup>) close to reported *in situ* values. Although the RMS error tends to decrease seasonally, its value reaches a maximum of 6.03 mg Chl *a* m<sup>-3</sup> in August 3<sup>rd</sup>-6<sup>th</sup> while the highest MRD are reported in summer. This clear discrepancy between simulated and remotely sensed fields of Chl *a* is, at least in the model, associated with less saline and more turbid waters transported towards the southwestern GSL through the estuarine circulation. Indeed, the front between the more turbid estuarine and clearer oceanic waters south of the Anticosti Island, and the plume of estuarine waters on the MS, superimpose quite well with the SeaWIFS spatial patterns in all composites (Figures III-4-8). Similarly, several important rivers flow into the GSL along the NS and their signature is also well resolved in the model through higher  $k_p$  values. These patterns are also coincident with those retrieved by SeaWIFS in spring (June 7<sup>th</sup>-11<sup>st</sup>, Figure III-4), early summer (July 2<sup>nd</sup>-8<sup>th</sup>, Figure III-5), and, to a lesser extent, in late summer (August

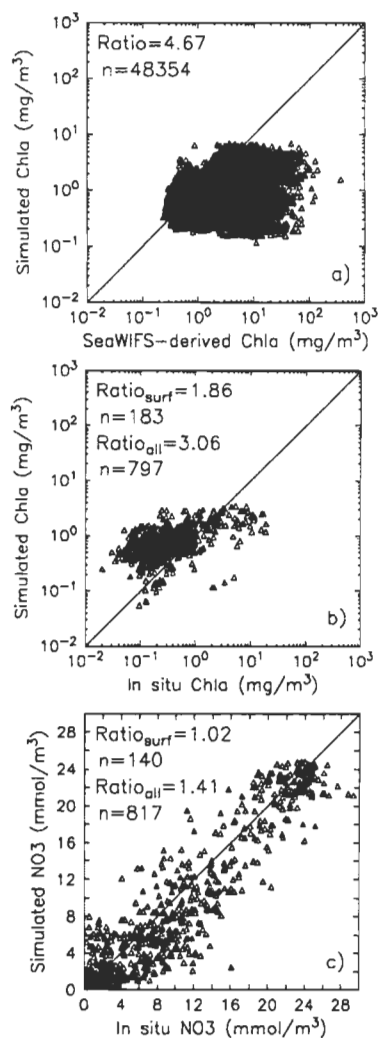


Figure III-12. Comparison of simulated Chl *a* with (a) SeaWiFS-derived Chl *a* and (b) *in situ* Chl *a*, and (c) comparison of *in situ* and simulated nitrate. *In situ* data include the whole set of available measurements made in 1998 (AZMP June and November cruises and fixed stations, SeaWiFS validation cruise of October-November, see text). In panels (b) and (c), surface values are in red whereas deeper values are in black (above 50 m for Chl *a*, the whole water column for nitrate).

Table III-5. Root mean square (RMS, mg Chl *a* m<sup>-3</sup>) error and mean relative difference (MRD, %) calculated between the SeaWiFS-derived and simulated Chl *a* concentrations (n=48361). Coincident points for each time period are shown in parentheses.

	All time periods	June 7 <sup>th</sup> -11 <sup>st</sup> (9654)	July 2 <sup>nd</sup> -8 <sup>th</sup> (9753)	August 3 <sup>rd</sup> -6 <sup>th</sup> (9827)	August 28 <sup>th</sup> - September 2 <sup>nd</sup> (9540)	October 6 <sup>th</sup> -14 <sup>th</sup> (9587)
RMS	4.84	6.37	4.09	6.03	3.81	2.9
MRD	47	24.79	61.29	51.51	56.51	40.75

28<sup>th</sup>-September 2<sup>nd</sup>, Figure III-7). The MRD and RMS error are higher in the western GSL (53% and 6.58 mg Chl *a* m<sup>-3</sup>, respectively), largely influenced by the St. Lawrence runoff, than in the eastern GSL (37.7 % and 2.15 mg Chl *a* m<sup>-3</sup>, respectively), where freshwater inputs are more limited. This suggests that the discrepancy between simulated and remotely sensed Chl *a* may be due to the weakness of the OC4v.4 algorithm in fresh and turbid estuarine waters.

The comparison of the simulated Chl *a* and nitrate with bottle measurements from the AZMP dataset (Figure III-12) showed results similar to those reported in *Le Fouest et al.* [2005], that is an overestimation of simulated Chl *a* (mean ratio of 1.84 and 3.05 for surface and all depth values, respectively) and a quasi-linear relationship with a slope close to 1 for nitrate (mean ratio of 1.02 to 1.4 for surface and all depths, respectively). The RMS error for Chl *a* is one order of magnitude lower than the RMS error calculated with SeaWiFS-derived Chl *a* and the MRD tends to be higher when all depths are considered instead of surface values only (Table III-3). This result confirms that the Chl *a* overestimation by the model occurs mainly at depth [*Le Fouest et al.*, 2005]. Most of the surface values (in red on Figure III-12b) are closer to the 1:1 line and the overestimation is limited to values below 0.5 mg m<sup>-3</sup>. The use of fixed C/N and C/Chl *a* ratio in the model, known to vary depending of light and nutrient levels [*Falkowski and LaRoche*, 1991; *Daly et al.*, 1999], as well as a low mortality rate of sinking diatoms at depth explain a large part of the discrepancy between the model and *in situ* data [see *Le Fouest et al.*, 2005]. The quasi-linear relationship between simulated and *in situ* nitrate concentrations (Figure III-12c), supported

by consistent simulated physical fields (Figure III-9bc, Table III-3), strengthens the model's ability to produce realistic levels of phytoplankton biomass at the regional scale.

When compared with a common subset of *in situ* observations, both the model and SeaWiFS Chl *a* concentrations are overestimated (Figure III-13). The mean SeaWiFS to *in situ* ratio is 3.53, higher than the value reported for SeaWiFS standard Chl *a* estimates in Chesapeake Bay and the Mid-Atlantic Bight (1.97 and 2.44, respectively; *Harding et al.*, 2005), while the mean  $Chl_{a_{sim}}$  to *in situ* ratio gives a lower value (2.45). The model's solutions are less dispersed (mean RMS error of 2.76 vs 4.52 mg Chl *a* m<sup>-3</sup>) and less biased (mean RMD of -145 % vs -253 %) than the  $Chl_{a_{sat}}$  estimates (Table III-6). The central northeastern GSL, less impacted by the land runoff, is characterized by higher MRD and RMS error for the model than for SeaWiFS (Table III-6), in contrast with the more coastal areas, namely the NS, the Jacques Cartier Strait (hereafter JCS), and the southern MS, where both the MRD and the RMS error associated to the SeaWiFS comparison are higher. Moreover, *in situ* surface Chl *a* concentrations higher than 5 mg m<sup>-3</sup> were seldom reported, even in June, and when so mainly in the LSLE. But such values are however generally limited in space and time in this subregion. By contrast,  $Chl_{a_{sat}}$  estimates higher than 10 mg m<sup>-3</sup> were systematically retrieved in spring and summer in the LSLE and NWG (Figures III-4-8, Figure III-9a, see also *Gower*, 2004). This also brings support to the hypothesis of a critical Chl *a* overestimation by the OC4v.4 algorithm in the Gulf's waters impacted by freshwater runoff.

The two early and late August composites and the LSLE are particular situations

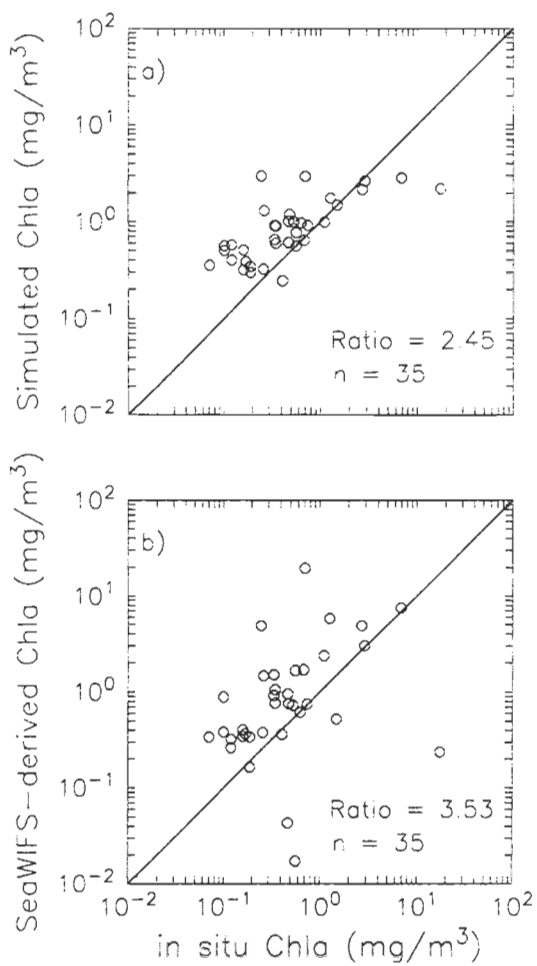


Figure III-13. Comparison of (a) simulated Chl *a* and (b) SeaWiFS-derived Chl *a* to *in situ* Chl *a* for the limited set of match-up points between SeaWiFS and *in situ* data.

Table III-6. Root mean square (RMS, mg Chl *a* m<sup>-3</sup>) error and mean relative difference (MRD, %) calculated between the *in situ* and simulated or SeaWIFS-derived Chl *a* concentrations for the GSL subregions (n=35). The number of match-up points for each subregion is displayed in parentheses.

		All time periods	LSLE (6)	NWG (4)	MS (5)	NEG (11)	NS (4)	JCS (5)
RMS	SeaWIFS	4.52	10.68	2.4	0.72	0.19	0.57	0.87
	Model	2.76	6.61	0.58	0.27	0.27	0.31	0.53
MRD	SeaWIFS	-253.4	-760.6	-185.2	-57.45	-132.8	-247.9	-165.1
	Model	-145	-206.3	-97.48	-34.67	-185.9	-162.8	-115.7

suggesting that both freshwater-associated turbidity and local increases of the Chl *a* concentrations may explain the remotely sensed spatial patterns. The mixed contribution of  $Chl a_{sim}$  and  $k_p$  is particularly obvious in early August (Figure III-6) when wind-induced upwelling along the north shore of the NWG brings cold, more saline, and clearer (lower  $k_p$  values) waters to the surface. The resulting nutrient replenishment of the surface waters is associated to high  $Chl a_{sim}$  concentrations (5-10  $mg\ m^{-3}$ ) coincident with  $Chl a_{sat}$  in the same range of values. By contrast, high  $k_p$  values mainly contribute to explain the SeaWiFS spatial patterns along the Gaspé Peninsula at the same date. For all the studied periods, the LSLE exhibits substantial levels of  $Chl a_{sim}$  at the surface coincident with turbid waters downstream of the tidally-induced upwelling area. This latter area contrasts with high nitrate concentrations (up to 13  $mmol\ m^{-3}$  at the surface) but low  $Chl a_{sim}$ , and high  $k_p$  values (Figures III-4-8) associated to the St. Lawrence discharge. This typical feature of the LSLE is due to the rapid advection of the phytoplankton biomass and has been previously described by *Therriault and Levasseur* [1985, 1986] and *Zakardjian et al.* [2000]. The transport of the phytoplankton biomass towards the NWG through the Gaspé Current simulated by the model is obvious in all periods, except in October. Concurrently to this transport of Chl *a* from the LSLE, increased primary production associated to the mesoscale variability of the Gaspé Current is particularly marked between August 28<sup>th</sup> and September 2<sup>nd</sup> (Figure III-7). The large contribution of the freshwater-associated turbidity to the SeaWiFS-derived Chl *a* hides the validation of this mesoscale-induced higher primary production.

### 3. *The CDOM hypothesis*

The  $\text{Chl}a_{\text{sim}}$  solutions in the LSLE, the western GSL and on the MS cannot account for the  $\text{Chl}a_{\text{sat}}$  estimates which are unrealistically high as compared with the range of natural variability generally observed. The marked coincidence between the SeaWiFS spatial patterns and the simulated turbidity plume associated to the freshwater influence suggests that the optical properties of the Case 2 estuarine waters [Babin *et al.*, 1993; Nieke *et al.*, 1997; Jacques *et al.*, 1998] affect the Chl *a* retrieval in the LSLE, NWG and MS. Erroneous atmospheric correction and auxiliary optically active water constituents are thought to explain the poor covariance between *in situ* and Chl *a* concentrations given by OC4v.4 in the GSL [Gregg and Casey, 2004; Gower, 2004; Yayla *et al.*, in prep.], as in many other coastal and shelf seas [e.g., Carder *et al.*, 1989; 1991; Darecki and Stramski, 2004; Toole and Siegel, 2001; Gohin *et al.*, 2002; Wang and Cota, 2003, Berthon and Zibordi, 2004; Kopelevich *et al.*, 2004; Harding *et al.*, 2005]. Sediment resuspension, not considered in the model, is an important process that probably interferes with the Chl *a* retrieval in the shallow waters of the JCS and Northumberland Strait [Fuentes-Yaco *et al.*, 1997a; Larouche, 2000] where intense tidal mixing occurs [Koutitonsky and Budgen, 1991; Saucier *et al.*, 2003]. The Northumberland Strait is generally characterized by high  $\text{Chl}a_{\text{sat}}$  levels but low  $\text{Chl}a_{\text{sim}}$  and  $k_p$  values. Low levels of  $\text{Chl}a_{\text{sim}}$  are due to a strong nutrient limitation in these shallow waters, where the strong stratification in summer limits the nitrate replenishment of the euphotic zone from depth [Hargrave *et al.*, 1985; e.g., Le Fouest *et al.*, 2005]. Except in autumn (Figure III-8) when more turbid waters are trapped in the narrow strait (< 20 km wide), the simulated transport of freshwater driven by the

seaward estuarine circulation toward the strait is limited. It can be attributed to the lateral resolution of the circulation model (5 x 5 km) that may reduce the model's ability to resolve circulation in this area. Nevertheless, sediments should not be a major constituent accounting for turbidity in the open waters of the western GSL where high remotely sensed Chl *a* are retrieved.

CDOM, which has been shown to significantly impact the optical properties of the St. Lawrence estuarine waters with a decreasing spatial gradient from the LSLE toward the GSL [Nieke *et al.*, 1997], is a more likely factor to explain the overestimation of the OC4v.4 Chl *a* retrieval in the estuarine waters of the GSL. CDOM has been also reported to contribute to the light attenuation in the MS [Larouche, 1998; 2000] showing an inverse correlation with salinity. While not shown here, CDOM absorption values derived from the Garver-Siegel-Maritorena (GSM) semi-analytical model [Maritorena *et al.*, 2002] provided by SeaDAS v4.5 were found to superimpose quite well with the OC4v.4-derived spatial patterns, especially along the coasts and in areas impacted by the estuarine waters. However, the remotely sensed CDOM absorption generally reached unrealistically high values concomitantly with high  $Chl_{a_{sat}}$  and simulated  $k_p$  values. While Nieke *et al.* [1997] report CDOM absorption coefficients up to  $1.3 \text{ m}^{-1}$ , remotely sensed estimates greater than  $2 \text{ m}^{-1}$  represented up to 11 % of the SeaWiFS data. The GSM model being tuned from a specific and global scale dataset and optimized for non-polar Case 1 waters, as the OC4v.4 algorithm, it is also inappropriate for the Gulf's turbid waters which are rather of Case 2. Negative and non-zero water-leaving radiances ( $L_w$ ) are reported in our SeaWiFS data in the blue domain (412 nm and 443 nm) and in the near infrared (765 nm and 865 nm),

respectively, especially in areas impacted by freshwater. Erroneous reflectance at 412 nm and 443 nm, where CDOM absorption is at its maximum, lead to unrealistic CDOM absorption coefficients retrieved by the GSM model and may be caused by a wrong atmospheric correction. Atmospheric corrections thus appear as a key stage in the SeaWiFS data processing for the Gulf's waters. Their improvement has been shown to allow a better determination of  $L_w$  in Case 2 waters, such as limiting the number of negative values in the blue part of the spectrum [Lavender *et al.*, 2005]. However, erroneous atmospheric corrections are unlikely to affect the consistency of the mesoscale spatial patterns produced by SeaWiFS. Absorption by allochthonous CDOM drained by land runoff and transported by the regional estuarine circulation is then the most probable explanation for the discrepancy between the simulated and SeaWiFS-derived Chl *a*.

#### 4. *Tracking the estuarine circulation and the associated mesoscale activity*

In coastal waters, CDOM originating from land runoff is mainly composed of refractory compounds [Blough and Del Vecchio, 2002]. It has been suggested that the remotely sensed CDOM signature could be used to track freshwater flows in coastal waters [e.g., Nieke *et al.*, 1997; Siddorn *et al.*, 2001; Coble *et al.*, 2004] or even infer salinity fields in shelf seas under freshwater influence [Binding and Bowers, 2003]. Considering the hypothesis of a strong imprint of allochthonous CDOM on the SeaWiFS Chl *a* retrievals, the SeaWiFS composites may be used to validate the simulated estuarine circulation. Coincident with high simulated turbidity, the SeaWiFS estimates are particularly high in the LSLE and NWG in spring and early summer (Figures III-4 and III-5), following the

freshwater runoff maximum in May. A similar situation also occurs along the Gaspé Peninsula showing the spreading of the estuarine waters that extends far onto the MS. Relatively high freshwater-associated turbidity is also encountered in the Baie des Chaleurs which receives the freshwater discharge of 4 rivers located along its shores and the surface waters of the seaward estuarine flow [Gan *et al.*, 2004]. In early August, the high simulated turbidity on the MS (Figure III-6) shows the advection of the main estuarine plume from the NWG toward the MS in summer, while the turbid estuarine waters are now restricted to the LSLE and the southern NWG due to the seasonal decrease of the St. Lawrence runoff. Overall, both simulated turbidity and SeaWiFS spatial patterns superimpose at this time but the remotely sensed signature does not follow the intensity of the simulated turbidity plume. Long exposure in the well illuminated surface layer can lead to CDOM photodegradation [e.g., Moran *et al.*, 2000; Whitehead *et al.*, 2000], a process which is not considered in the model. Hence, the high-simulated turbidity of the main estuarine plume on the MS in early August (Figure III-6) may be overestimated. Later in summer, both simulated turbidity and remotely sensed Chl *a* fields exhibit similar spatial patterns around the Cap Breton (Figure III-7) and show the preferential outflow of the estuarine waters in the southwestern part of Cabot Strait, as generally observed [e.g., Koutitonsky and Bugden, 1991].

At finer scale, the circulation is strongly impacted by mesoscale instabilities of the buoyancy-driven Gaspé Current which is the preferential way for the outflow of the estuarine waters towards the GSL [El-Sabh, 1976; Tang, 1980a; Benoit *et al.*, 1985; Mertz *et al.*, 1988; Koutitonsky and Bugden, 1991; Mertz *et al.*, 1991]. During spring and early

summer (Figures III-4 and III-6), the Gaspé Current interacts with a prominent cyclonic gyre in the NWG [El-Sabh, 1976, Sévigny *et al.*, 1979, Tang, 1980b]. The simulated fields of surface currents and  $k_p$  show a partial recirculation of the estuarine waters in the gyre and a marked offshore displacement of the jet associated to an anticyclonic eddy in the northwestern USt. The offshore circulation of the jet and the associated frontal structures in the USt are well known features [El-Sabh, 1976; Lacroix, 1987; Mertz *et al.*, 1988, 1989; Sheng, 2001]. High  $Chl_{a_{sat}}$  values are found in the anticyclonic eddy, where the turbid estuarine waters simulated by the model are trapped. In summer and fall, the model produces smaller wave-like instabilities (Figures III-6-8) also reported in the literature [Tang, 1980a; Mertz *et al.*, 1988]. The smaller anticyclonic eddies associated to these structures retain the estuarine turbid waters along the Gaspé Peninsula. While not strictly coincident in space, spatial patterns similar in shape and size are generally evidenced in the SeaWiFS composites by high  $Chl_{a_{sat}}$  values, especially in early August (Figure III-6). These patterns are less obvious in the SeaWiFS composite of late August (Figure III-7) probably because of a mixed contribution of  $Chl\ a$  and CDOM in the retrievals (see section III.2). In October (Figure III-8), both the model and SeaWiFS suggest a lower mesoscale activity with smaller and more spaced instabilities.

The main estuarine circulation being driven by salinity gradients, the mesoscale patterns are not systematically evidenced by the  $SST_{sat}$  or the  $SST_{sim}$ . At mesoscale, the response time of SST to heat fluxes is longer than the time scale associated to the phytoplankton uptake [Mahadevan and Campbell, 2002]. The temperature gradients are generally weak, except in October (Figure III-8) when  $SST_{sat}$ ,  $SST_{sim}$ , simulated  $k_p$ , and

SeaWiFS retrievals show coherent spatial patterns in the NWG and USt. At the same date in the NEG, substantial  $\text{Chl}a_{\text{sim}}$  concentrations ( $2.25 \text{ mg m}^{-3}$ ) contrasting with poorer adjacent waters ( $< 1 \text{ mg m}^{-3}$ ) are associated to low ( $< 6^\circ\text{C}$ )  $\text{SST}_{\text{sim}}$  and  $\text{SST}_{\text{sat}}$ . A pattern similar in shape is evidenced by the SeaWiFS Chl *a* retrievals but in continuity with a nearshore fringe of high values extending farther westward. This fringe that extends along the NS cannot be explained by the simulated turbidity nor a simulated upwelling-induced increased production for reasons still not elucidated at this time. Nevertheless, a similar event of increased primary production in the NEG during fall has already been described in *Le Fouest et al.* [2005]. This situation, also supported by a SeaWiFS Chl *a* composite, has been shown to be related to pulsed inflows of Labrador Sea water spreading along the NS.

## CONCLUSIONS

Faced with the challenges of climate change and sustainable development, modern oceanography has favoured the emergence of new observation and predictive tools. Remote sensing and numerical modelling have considerably evolved in the last two decades to infer the oceanic variability with a high spatial and temporal resolution hard to achieve with field surveys. The joint use of remote sensing and numerical modelling has recently allowed the development of operational oceanography systems, following the path taken in operational meteorology over the past few decades. Data assimilation from a variety of platforms, both *in situ* (e.g., the ARGO program) and remote (aircraft and space sensors), increases the short-time scale predictive ability of numerical models [see for recent examples *Kamachi et al.*, 2004; *Masina et al.*, 2004; *Molcard et al.*, 2005; *Belyaev et al.*, 2005] and is not limited anymore to physical variables but also biological ones like algal pigments [e.g., *Friedrichs*, 2002; *Hoteit et al.*, 2003; *Natvik and Evensen*, 2003; *Ibrahim et al.*, 2004]. Because of the need to estimate carbon fluxes at global scale, the improvement of the numerical models performances using satellite-derived data have primarily focused on the global ocean while the more complex physics and optics of the coastal ocean have long been limiting for the same applications. Nevertheless, projects specifically devoted to the coastal environment, such as the HyCODE program [e.g., *Dickey*, 2004; *Chang et al.*, 2004], are now emerging following recent advances in optical instrumentation and coastal modelling [e.g., *Garcia-Gorriz et al.*, 2003; *Barron et al.*, 2004; *Di Lorenzo et al.*, 2004, *Kurapov et al.*, 2005]. This

trend will strengthen in the near future given the key role of continental margins in the global carbon cycle [e.g., *Muller-Karger et al.*, 2005].

As a contribution to this general framework, we presented a study using synoptic AVHRR-derived SST and SeaWiFS ocean color data to validate the regional 3-D high-resolution physical-biological coupled model of the Gulf of St. Lawrence. The simulated and remotely sensed SST both provided a good estimate of *in situ* records and are strikingly in agreement in their spatial patterns, both at the mesoscale and regional scale. The comparison of the simulated and remotely sensed Chl *a* with *in situ* measurements revealed an overestimation by SeaWiFS in the estuarine waters, suggesting that the satellite Chl *a* retrieval is contaminated by auxiliary optically active water constituents (mainly CDOM), thus impeding the quantitative validation of the simulated surface Chl *a* concentrations. Nevertheless, the SeaWiFS spatial patterns have been shown to superimpose quite well with the freshwater-associated turbidity simulated by the model and have been used to validate the mesoscale to seasonal variability of the regional estuarine circulation. To fully exploit the SeaWiFS information, Case 2-adapted data processing for an accurate Chl *a* and CDOM absorption retrieval in the GSL waters is required before these fields can be assimilated in 3-D coupled physical-biological models. SeaWiFS and other recently launched sea color instruments (MODIS and MERIS) provide daily and high spatial resolution data which, complemented with the Gulf monitoring database (AZMP), would allow a more accurate validation of the model results both in space and time. The improvement of a robust tool associating remote sensing, real-time monitoring, and 3-D physical-biological modelling is necessary in a perspective of operational biological

oceanography. A finer validation of the physical-biological links from the mesoscale to regional and seasonal scales would also increase the ability of the model to respond with some confidence to climate change scenarios.

**IV. IMPACT OF FRESHWATER-ASSOCIATED TURBIDITY  
ON PHYTOPLANKTON IN A HIGHLY DYNAMIC SHELF SEA: A  
MODELLING STUDY IN THE GULF OF ST. LAWRENCE (CANADA)**

## ABSTRACT

The Gulf of St. Lawrence (GSL) is a highly dynamic sub-arctic inland sea that receives a substantial freshwater runoff from the St. Lawrence River. Its outflow forms an estuarine plume that flushes the western GSL before reaching the Scotian Shelf. The plume presents distinct optical characteristics than the clearer Gulf's waters but little is known about its effects on phytoplankton dynamics. In this study, we used a 3-D high-resolution physical-biological model to investigate the impact of freshwater-associated turbidity on phytoplankton dynamics in the GSL. The use in the model of a salinity-dependant diffuse attenuation coefficient associated to nonchlorophyllous matter allowed to simulate the influence of water turbidity on plankton dynamics. By delaying the spring bloom timing, it led to its improved representation in the Lower St. Lawrence Estuary whose dynamics is strongly influenced by the seasonal freshwater runoff. Moreover, simulated nitrate concentrations were increased and found to be in better accordance with space and time coincident *in situ* measurements at two fixed stations located within the seaward estuarine outflow. Increased lateral nitrate fluxes in the surface layer were also more consistent with those reported in the literature. However, because of the lower nutrient uptake associated to a stronger light limitation, primary production resulted highly suppressed in the estuarine plume reaching unrealistic rates in reference to previous studies. This apparent paradox highlights the need for an improved modelling of the phytoplankton response to the turbid and highly dynamic environments that characterize the St. Lawrence, a prerequisite in a perspective of operational biological oceanography.

## INTRODUCTION

The Gulf of St. Lawrence (hereafter GSL) is a highly dynamic sub-arctic inland sea that receives a substantial freshwater runoff ( $350 \text{ km}^3 \text{ yr}^{-1}$ ) from the St. Lawrence River. This runoff contributes significantly to the freshwater input into the North-Atlantic Ocean. The estuarine waters control the intensity of the buoyancy-driven circulation of the northwestern Gulf characterized by a coastal jet, the Gaspé Current. This circulation feature is of major importance for planktonic production in this part of the GSL [Levasseur *et al.*, 1992; Fortier *et al.*, 1992] but also in conterminous subregions [Le Fouest *et al.*, 2005]. The seasonal freshwater discharge influences the zooplankton distribution in the Magdalen Shallow [de Lafontaine *et al.*, 1984; Runge and Simard, 1990] and was shown to correlate with crustacean and fish landings in this subregion [Drinkwater *et al.*, 1991]. The Gaspé Current is also considered as the main route for nutrient transport from the productive northwestern subregions toward the more stratified and nitrate-poor Magdalen Shallow [Savenkoff *et al.*, 2001].

An aspect less investigated concerns the impact of the turbidity of the St. Lawrence estuarine waters on plankton production. However, substantial concentrations of auxiliary optically active constituents, i.e., mineral and organic sediments and coloured dissolved organic matter, are drained from the continent toward the GSL to make optical properties there more complex than in the open ocean. They constrain the light field experienced by phytoplankton by reducing the penetration of the photosynthetically available radiation needed for growth. Indeed, the estuarine optical signature can extend far into the western

GSL, as shown by substantial light attenuation in the Magdalen Shallow associated to lower salinity and higher CDOM levels [Larouche, 1998]. In the previous study of *Le Fouest et al.* [2005], the use of a constant attenuation coefficient related to nonchlorophyllous matter fitted for more oceanic waters (e.g., the eastern GSL) failed in reproducing the phytoplankton seasonal cycle in the Lower St. Lawrence Estuary (LSLE) presenting Case 2 optical characteristics [Babin *et al.*, 1993; Nieke *et al.*, 1997; Jacques *et al.*, 1998]. This result brought some evidence that the simulated light field was determinant for the bloom timing in the freshwater-influenced subregions of the GSL.

Tridimensional coupled physical-biological models are widely used to quantify nutrient budgets and primary production in shelf seas [e.g., Neumann, 2000; Skogen and Moll, 2000; Grégoire and Becker, 2004]. While eutrophication scenarios have been extensively simulated using 3-D regional models [e.g., Barreta *et al.*, 1994; Lancelot *et al.*, 2002; Korpinen *et al.*, 2004; Neumann and Schernewski, 2004; Skogen *et al.*, 2004], only few studies have specifically focused on the influence of the freshwater-associated turbidity on marine coastal phytoplankton dynamics [e.g., Walsh *et al.*, 2003; Huret *et al.*, 2005]. In the GSL, however, turbidity has been shown to be of major importance as evidenced by the good agreement between SeaWiFS sea color data and simulated turbidity fields in spring, summer and fall [*Le Fouest et al.*, in revision, 2005]. In this modelling study, the impact of freshwater-associated turbidity on phytoplankton dynamics in the GSL is examined. We attempt to quantify the influence of the estuarine plume on seasonal phytoplankton dynamics, primary production and nitrogen fluxes in the GSL through the comparison of two runs that distinguish by the formulation of the diffuse attenuation coefficient associated

to nonchlorophyllous matter (fixed *vs* salinity-dependant). In regard to these results, the performances of the two model configurations are evaluated and the development perspectives discussed.

## THE COUPLED MODEL

A detailed description of the planktonic ecosystem model and its coupling to the primitive equation physical model of the GSL [Saucier *et al.*, 2003; 2004] can be found in Le Fouest *et al.* [2005; in revision]. Briefly, the physical model consists in a shallow water and tracer conserving hydrostatic ocean model complemented with a level 2.5 turbulent kinetic energy equation [Mellor and Yamada, 1974, 1982]. It is coupled to a dynamic and thermodynamic two-layers sea ice and one-layer snow cover model [Semtner, 1976; Hunke and Dukowicz, 1997]. The heat fluxes between the ocean, sea ice and the lower atmosphere are governed by bulk aerodynamic exchange formulas. The Canadian Operational Weather Forecast Model provides three-hourly atmospheric forcings including air temperature, dew point, surface winds, light, cloudiness, precipitation and surface pressure. Monthly and daily runoff data of the St. Lawrence River and 28 main tributaries, respectively, and hourly water levels (co-oscillating tides) and monthly mean temperature and salinity prescribed at the oceanic boundaries (Cabot Strait and Strait of Belle-Isle) provide the hydrologic and oceanic forcings of the model. The  $1/22^\circ$  resolution 3-D model extends from Cabot Strait and Strait of Belle-Isle to the upper limit of the tidal influence near Quebec. From the surface to 300 m depth, the cell thickness is 5 m and 10 to 20 m below, with free surface and bottom layers adjusted to sea level and topography, respectively.

The planktonic ecosystem model coupled to the sea ice-ocean model includes the herbivorous (nitrate; large phytoplankton [ $> 5 \mu\text{m}$ ]; mesozooplankton [200-2000  $\mu\text{m}$ ]; particulate organic matter) and microbial food webs (ammonium; small phytoplankton [ $< 5$

$\mu\text{m}$ ]; microzooplankton [20-200  $\mu\text{m}$ ]; dissolved organic matter). Generic formulations using mean parameters found in the literature [see *Le Fouest et al.*, 2005] drive the nitrogen fluxes between the compartments. Biological variables are calculated in  $\text{mmol N m}^{-3}$  and algal biomass is converted in chlorophyll *a* (Chl *a*) units using a molar C/N ratio of 106/16 [Redfield *et al.*, 1963] and a C/Chl *a* mass ratio of 55 [Sinclair, 1978; Rivkin *et al.*, 1996]. The initial and boundary conditions of nitrate and Chl *a* of the model are derived from *in situ* data from fall 1997 through the Atlantic Zone Monitoring Program [AZMP; Therriault *et al.*, 1998] database. For the remaining biological compartments, initial and boundary conditions are the same than those used in *Le Fouest et al.* [2005]. Monthly climatological means of *in situ* nitrate and Chl *a* concentrations (Chifflet M, unpublished results) were prescribed at Cabot Strait and the Strait of Belle-Isle.

The model of light propagation in the water column follows the Beer-Lambert's law and takes into account the diffuse attenuation by pure seawater, Chl *a*, and nonchlorophyllous matter. The model is run with two configurations of the attenuation by nonchlorophyllous matter (hereafter  $k_p$ ). The first one implies the use of a fixed coefficient ( $0.04 \text{ m}^{-1}$ ) that was fitted to obtain a simulated euphotic zone consistent with the observations in the GSL [see *Le Fouest et al.*, 2005]. In the second one,  $k_p$  is set to vary with the model salinity. This formulation finds support in the inverse linear relationship that links the CDOM absorption to salinity in the GSL [Nieke *et al.*, 1997] and other coastal waters [e.g., Ferrari and Dowell, 1998; Kowalczyk, 1999; Siddorne *et al.*, 2001; Keith *et al.*, 2002; D'Sa and Miller, 2003]. This simulated bulk turbidity is then assumed to be mainly associated to terrestrial CDOM without *in situ* degradation. The linear equation

between  $k_p$  and salinity (see Figure III-2 in *Le Fouest et al.*, in revision, 2005) was derived from *in situ* data (salinity, Chl *a*, and total attenuation coefficient) obtained from four SeaWiFS validation cruises conducted in fall 1997-1998, summer 1999, and spring 2001 for a total of 63 stations covering the whole Estuary and Gulf. The values of  $k_p$  are calculated by subtracting the attenuation coefficient due to Chl *a* (see eq. 6 in *Le Fouest et al.*, 2005) and the attenuation coefficient for pure seawater (set to  $0.04 \text{ m}^{-1}$ ; *Morel*, 1988) from the measured total attenuation coefficient. The linear equation ( $k_p = -0.0364 \text{ Salinity} + 1.1942$ ,  $r^2=0.71$ ), is closed in the model by two salinity thresholds at 26 ( $k_p=0.25 \text{ m}^{-1}$ ) and 32 ( $k_p=0.03 \text{ m}^{-1}$ ).

## RESULTS

The yearly- and depth-averaged (0-10 m) simulated currents, salinity and  $k_p$  (Figure IV-1) illustrate the mean surface circulation of the estuarine waters in the GSL. Fresh and turbid waters from the St. Lawrence, Saguenay and Manicouagan-aux Outardes rivers are flushed from the Estuary toward the northwestern GSL (hereafter NWG), where they drive the Gaspé Current, a coastal jet known to be the preferential way for the outflow of the estuarine waters. When leaving the Unguedo Strait (hereafter USt), the plume spreads in the Magdalen Shallow (hereafter MS) or flows seaward through the southern Laurentian Channel (hereafter SLC). At Cabot Strait, the surface waters leaving the southern MS near Cape Breton join the seaward circulation over the deep Laurentian Channel to reach the Scotian Shelf. The mean distribution of the simulated salinity-dependant  $k_p$  shows values increased by up to half an order of magnitude ( $0.22 \text{ m}^{-1}$ ) in the LSLE, when compared to the fixed  $k_p$  used in the control run ( $0.04 \text{ m}^{-1}$ ). Mixing between the estuarine and saltier waters leads to a decreasing North-South gradient in the estuarine plume but values remain two to four times higher ( $0.08\text{-}0.16 \text{ m}^{-1}$ ) in the MS and increase inshore. Consequently, the depth of the euphotic zone ( $Z_e$ ) shows greater spatial variations than when using a fixed  $k_p$  (Figure IV-2). In this case, slight variations in  $Z_e$  ( $Z_e \sim 30\text{-}40 \text{ m}$ ) in the western Gulf are mainly due to phytoplankton self-shading, the strong decrease inshore being due to depth limitation (depth lower than  $Z_e$ ). Using a salinity-dependant turbidity highly reduces  $Z_e$  in the freshwater impacted areas with values that are now 10-20 m in the LSLE, the Gaspé Current and on the western MS but always close to 30 m in the NEG.

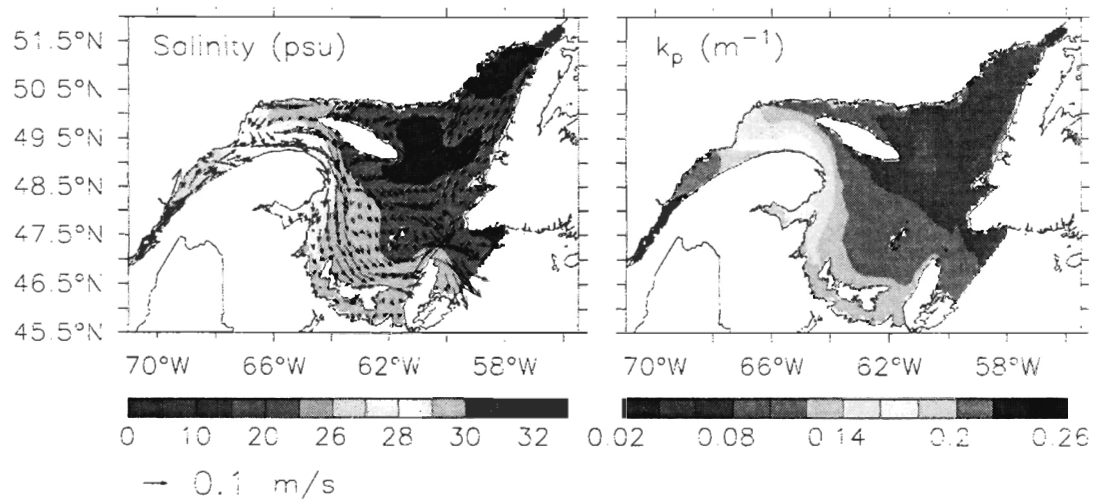


Figure IV-1. Annual mean of the depth-averaged (0-10 m) salinity (with currents overlaid) and  $k_p$  for the run using a variable  $k_p$ .

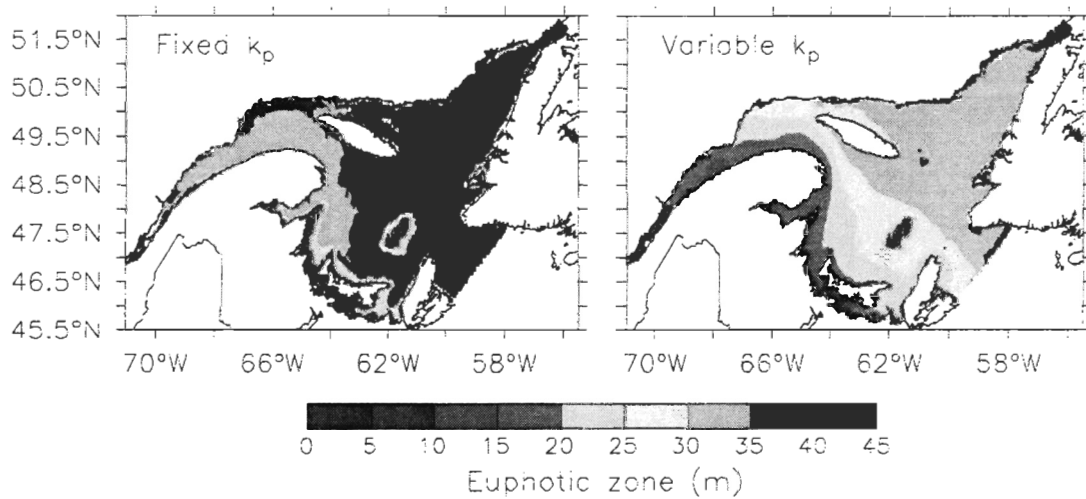


Figure IV-2. Annual mean of the depth of the euphotic zone for the run using a fixed or a variable  $k_p$ .

This change in the simulated light conditions has a strong impact on the simulated phytoplankton production especially in the estuarine plume where light limitation is more pronounced. Both new and regenerated productions are impacted, especially in the LSLE where they are the most suppressed (Figure IV-3). By contrast, comparable  $Z_e$  in the eastern GSL translate into a limited effect on primary production. Phytoplankton growth rate being set as the lowest of the light- and nutrient-based estimate (Liebig's law), this marked light limitation decreases nutrient assimilation in the more turbid plume that is associated to higher ammonium and nitrate concentrations (Figure IV-4) near twice those simulated using a fixed  $k_p$ . The ammonium concentrations are near  $1 \text{ mmol m}^{-3}$ , close to the imposed initial conditions [see *Le Fouest et al.*, 2005]. The highest nitrate concentrations are simulated in the LSLE and NWG in both runs as a consequence of tidal upwelling of cold nutrient-rich intermediate waters occurring at the head of the Laurentian Channel [*Steven*, 1974; *Greisman and Ingram*, 1977; *Gratton et al.*, 1988; *Saucier and Chassé*, 2000]. Decreasing nutrient assimilation due to turbidity in the LSLE leads to a higher nutrient concentrations in the outflowing estuarine waters that can be seen downward on the western MS. As a result, all the western part of the GSL shifts from a nutrient-limited to a light-limited mean state (Figure IV-5). Comparatively, changes are of lesser extent in the NEG, the whole subregion being still in a nutrient-limited mean state, and are limited to a thin fringe near the north coast and in the Jacques Cartier Strait (hereafter JCS) due to freshwater inputs from numerous tributaries. Sea ice melt may also affect the surface salinities and then the  $k_p$  values in these two areas where the seasonal sea ice coverage is the highest of the NEG. Regarding surface (0-10 m) integrated Chl  $a$ , concentrations in the

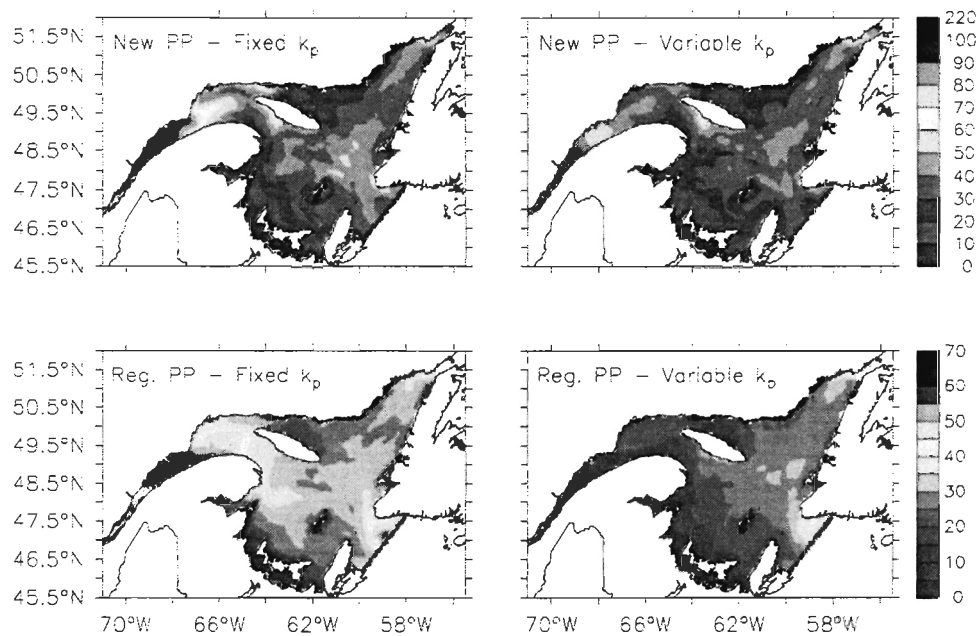


Figure IV-3. Yearly- and depth-integrated (0-45 m) new and regenerated primary production (PP;  $\text{g C m}^{-2} \text{yr}^{-1}$ ) for the run using a fixed or a variable  $k_p$ .

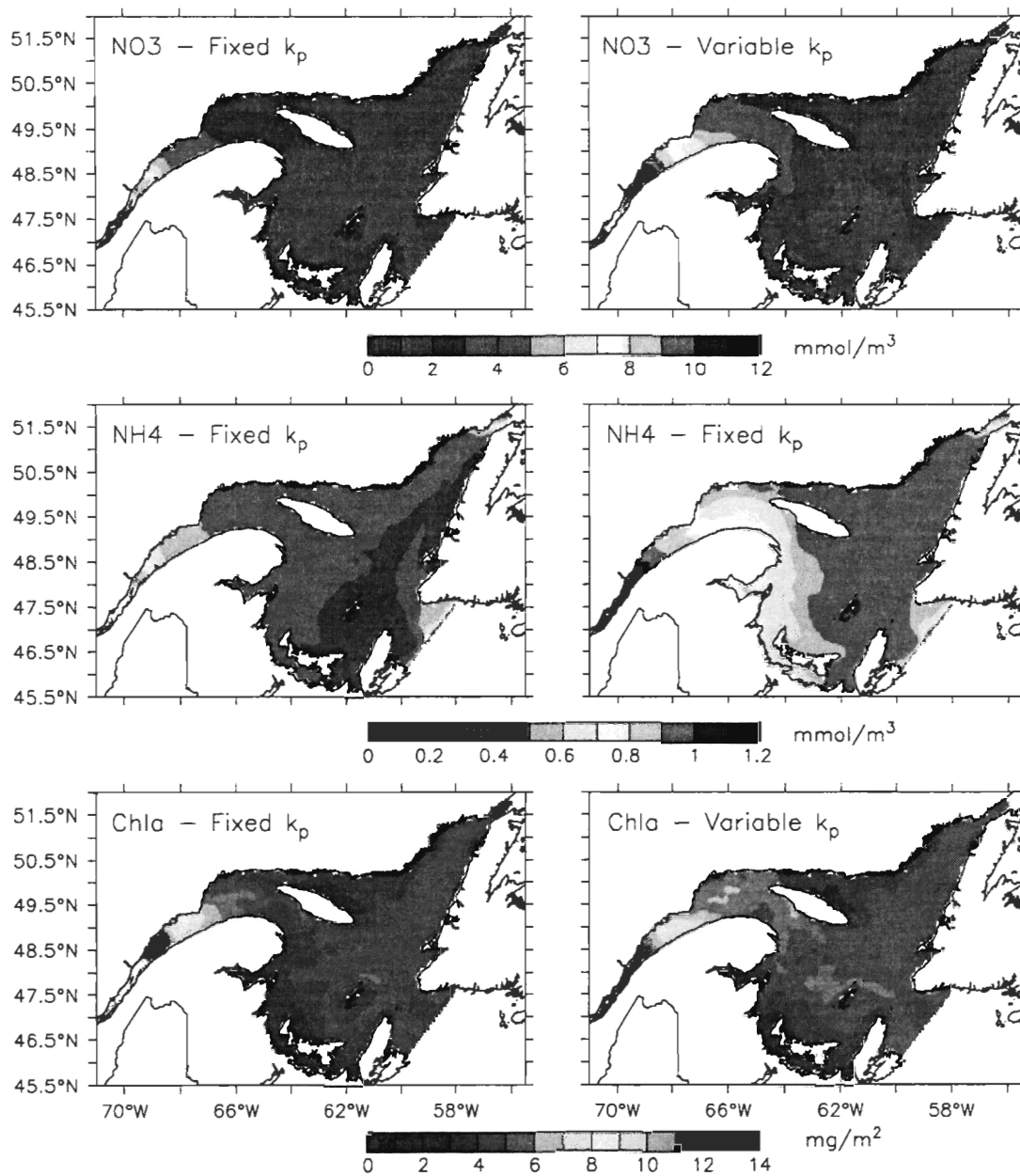


Figure IV-4. Annual mean of the depth-averaged (0-10 m) nitrate and ammonium, and depth-integrated (0-10 m) Chl *a* for the run using a fixed or a variable  $k_p$ .

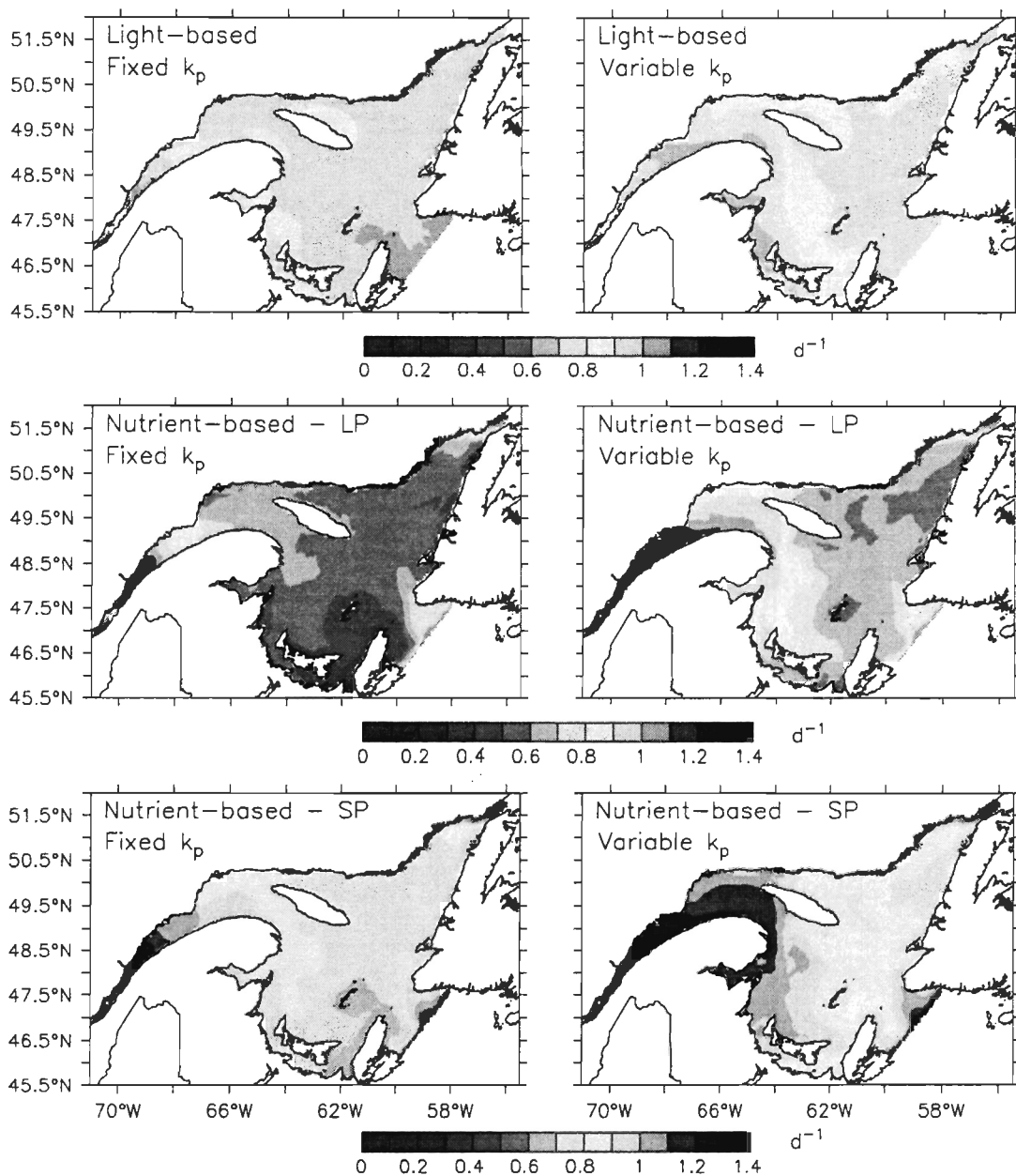


Figure IV-5. Annual mean of the depth-averaged (0-10 m) growth rates of large and small phytoplankton (LP and SP, respectively) for the run using a fixed or a variable  $k_p$ . Because the two phytoplankton groups show the same response to light, only one panel is presented for both size classes.

LSLE are reduced by a factor two in average while they are slightly higher in the NWG and on the MS probably due to the advection of algal biomass.

These changes in nutrient and light conditions have major implications on the seasonal cycle of phytoplankton. Figure IV-6 shows that turbidity adds to sea ice in controlling the timing of the spring bloom. In the estuarine turbid waters, the bloom onsets up to two months later in the LSLE and the delay shortens as the estuarine influence decreases from the LSLE to the MS. By contrast, the bloom shows a similar timing in the USt in both runs. Lower Chl *a* levels in the Gaspé Current, impacted by higher  $k_p$  values, are compensated by higher biomass along the Anticosti Island. The spring bloom that occurs three weeks later in the SLC is associated to the offshore branch of the estuarine outflow. Freshwater inputs from numerous tributaries along the north coast also affect the spring bloom timing which is delayed from few days to one week in the NEG and JCS, respectively. As noted above, sea ice melt may also contribute to this effect. In summer, changes in phytoplankton dynamics mainly occur in the subregions most freshwater-influenced, such as the LSLE, the northwestern GSL (hereafter NWG) and the JCS. In the JCS, phytoplankton biomass is suppressed by 62 % in July as a result of an increased river discharge in the area. Because of the freshwater-associated turbidity and its impact on the spring bloom timing, two peaks of phytoplankton biomass of comparable intensity occur in the LSLE and NWG in late spring and August. The summer peak coincides with the seasonal minimum of the St. Lawrence and NWG rivers discharge. Indeed, in the LSLE, the monthly- and spatially (laterally and from the surface to 45 m)-averaged  $k_p$  value falls

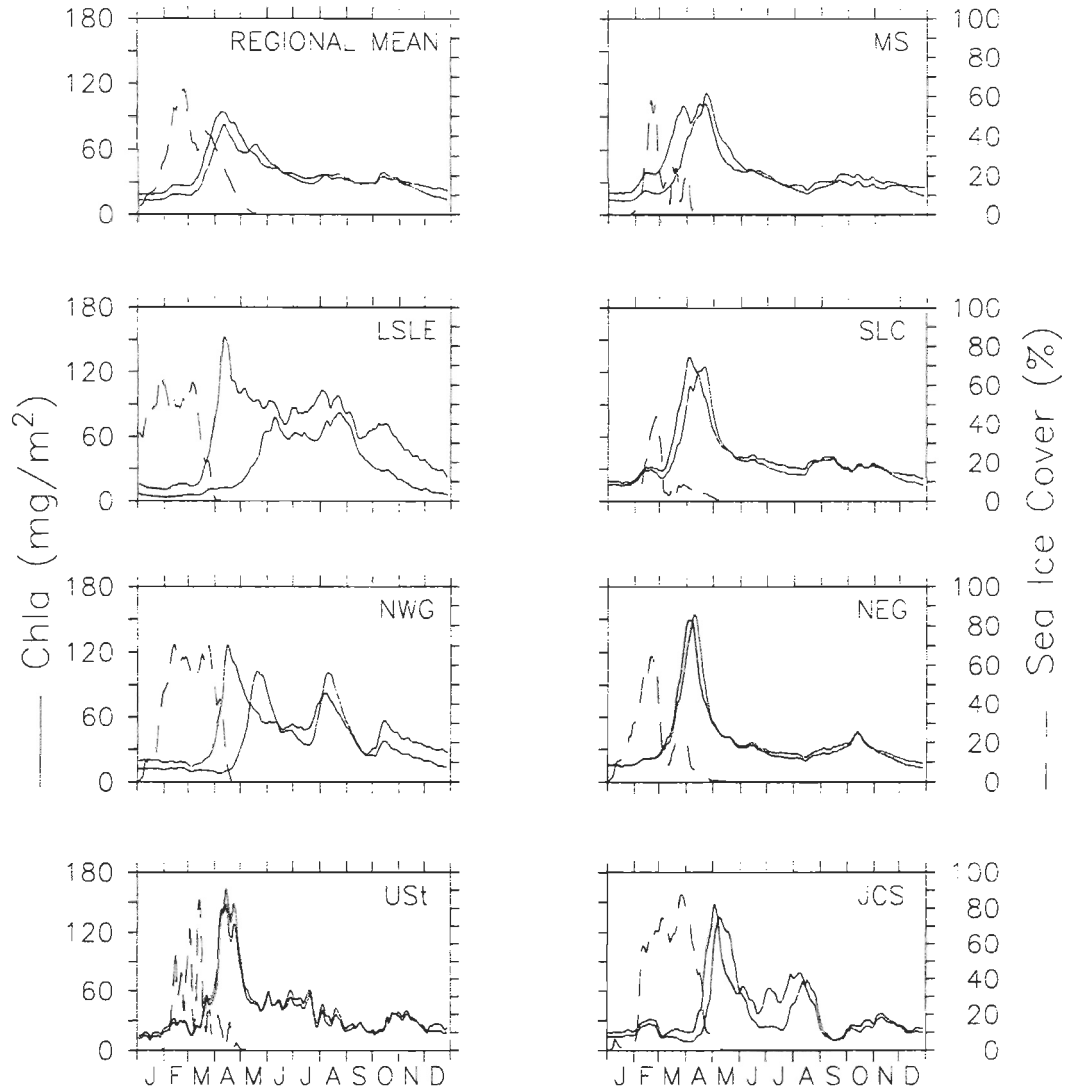


Figure IV-6. Mean seasonal cycle of total Chl *a* (integrated between 0-45 m) and sea ice concentration for the numerical domain as a whole and subregions of the GSL cited in the text. The black and red lines correspond to the run using a fixed and variable  $k_p$ , respectively.

from  $0.17 \text{ m}^{-1}$  in July to its seasonal minimum in August ( $0.12 \text{ m}^{-1}$ ). Similarly, the peak of biomass simulated in the JCS in August coincides with the seasonal minimum discharge from the neighbouring rivers. A fall bloom of relatively small intensity ( $\sim 30 \text{ mg Chl } a \text{ m}^{-2}$ ) occurs in October in all subregions following a strong wind event, except in the LSLE where turbidity remains sufficiently high to limit phytoplankton growth. Indeed, averaged over the LSLE, the mean  $k_p$  value in October reaches  $0.18 \text{ m}^{-1}$  at the surface and  $0.14 \text{ m}^{-1}$  when averaged over 45 m. By contrast, in the NWG, where a still marked fall bloom occurs, the mean  $k_p$  value is  $0.11 \text{ m}^{-1}$  at the surface and  $0.08 \text{ m}^{-1}$  when averaged over 45 m.

In all subregions, the shallowing of the productive layer depth translates into lower simulated primary production (Table IV-1). The LSLE and the NWG are the most impacted subregions exhibiting a 70 % and 38.4 % decrease of the primary production, respectively, and the highest shallowing of the mean productive layer (47.1 % and 33.6 %, respectively). In the LSLE, tidal and wind mixing of the fresher and more turbid surface waters with the deeper layers leads to the occurrence of high  $k_p$  values at depth, e.g., episodically up to  $0.13 \text{ m}^{-1}$  at 45 m (Figure IV-7). Figure IV-7 also shows the marked shallowing (more than 20 m of amplitude in June) of the nutricline occurring in spring and summer when the  $k_p$  values are close to their maximum in the first 10 m of the water column. Hence, while not nutrient-limited, phytoplankton growth is impacted by lower light levels penetrating in the upper layer. In the JCS, where tidal mixing is also a major process for primary production, primary production shows a higher decrease (27.1 %) than in the MS (15.4 %). By contrast to the MS, where nutrient replenishment from depth is precluded due to its shallow bathymetry, subsurface increases of primary production associated to the shoaling of the

Table IV-1. Mean annual primary production of the GSL and its subregions ( $\text{g C m}^{-2} \text{ yr}^{-1}$ ).

	All grid	LSLE	NWG	USt	MS	SLC	NEG	JCS
Fixed $k_p$	72.4	192.7	94.7	75.7	66.8	75.6	67.4	80.3
Variable $k_p$	54.8 (-24.3 %)	57.8 (-70 %)	58.2 (-38.5 %)	72 (-4.9 %)	56.5 (-15.4 %)	66.7 (-11.8 %)	62.1 (-7.8 %)	58.5 (-27.1 %)

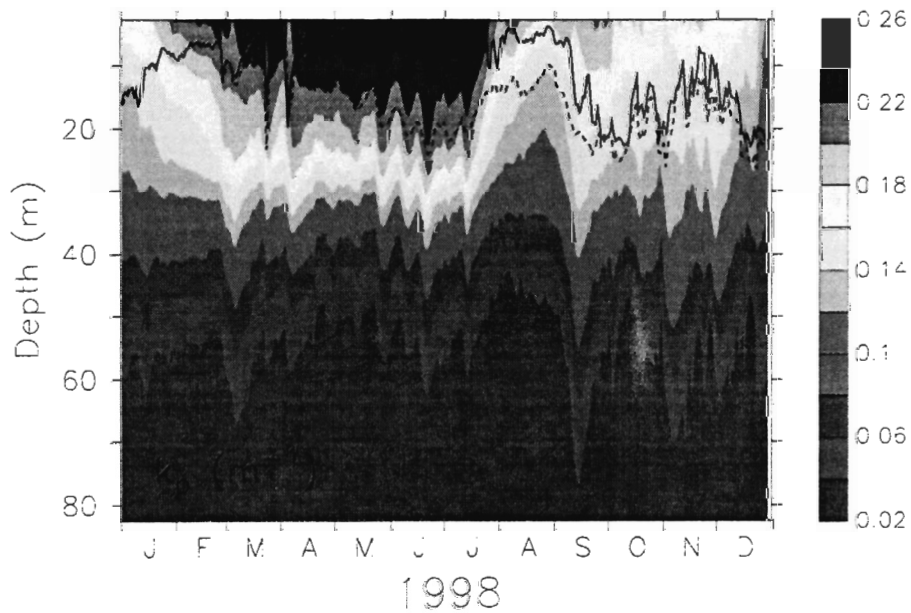


Figure IV-7. Time series of the vertical distribution  $k_p$  ( $\text{m}^{-1}$ ). The nutricline from the run using a fixed  $k_p$  (black dashed line) and a variable  $k_p$  (black line) are overlaid.

nitracline substantially contribute to the annual primary production of the JCS [see *Le Fouest et al.*, 2005]. The main difference between the two runs occurs in summer in the narrower (30 km) and shallower (< 100 m) part of the strait (not shown here). Similarly to the LSLE, the fresher and more turbid waters poured out by rivers are mixed with the deeper layers reducing thus light penetration and preventing the formation of a deep Chl *a* maximum.

As a consequence of lower light availability for phytoplankton growth, the new primary production simulated by the model shows a reduction of 20.4 %, impacting especially the large size fraction of phytoplankton (-21.3 % vs -14.3 % for the small fraction). Indeed, large phytoplankton dynamics is mainly controlled by nitrate availability whereas the non-sinking small phytoplankton rather grows on recycled ammonium. Interestingly, the simulated regenerated primary production is more suppressed with a reduction of 28.8 %. This result can be explained by the lower ammonium production (-24.7 %) that depends of the food webs' activity and, similarly to nitrate, the lower ammonium uptake due to increased light limitation (Figure IV-5). Because of its distribution more at the surface of the water column, where  $k_p$  values are the highest, small phytoplankton exhibits a higher reduction of the regenerated primary production (-31.7 %) than large phytoplankton (-25.7 %). In addition to modify phytoplankton seasonal dynamics, water turbidity involves changes in the seasonal nitrogen fluxes between the subregions influenced by the estuarine plume. For both runs, ratios of the yearly- and depth-integrated (0–30 m) nitrate vs organic nitrogen flux along transects within the estuarine plume (see Figure IV-8 for the location of the transects) were calculated. In the

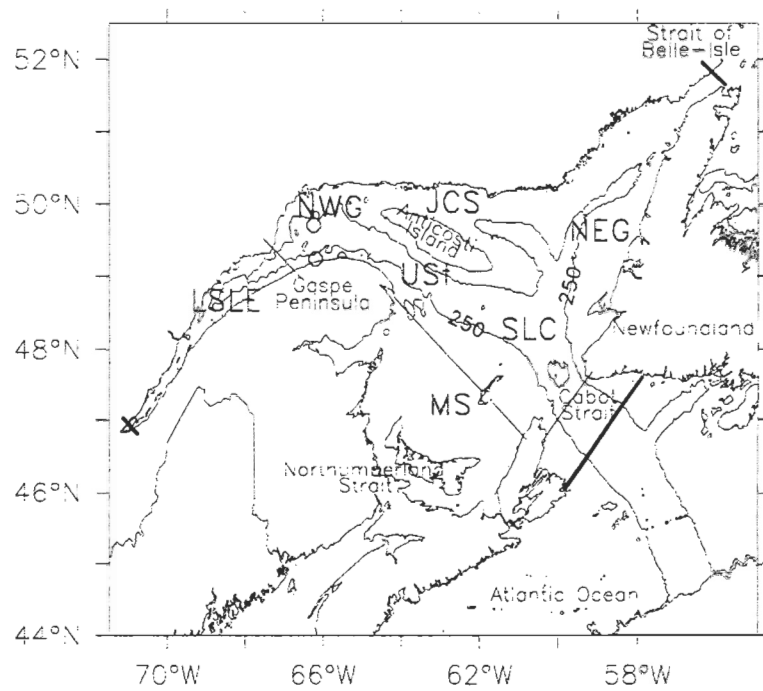


Figure IV-8. Map of the Estuary and Gulf of St. Lawrence. Acronyms indicate the subregions cited in the text. The bold lines are the open boundaries of the coupled model. The thin lines indicate the transects used for nitrogen fluxes estimations. Circles show the location of the Gaspé (nearshore) and Anticosti (offshore) stations.

run using a fixed  $k_p$ , nitrate fluxes are overall higher than organic nitrogen fluxes, up to two-times in the downstream boundary of the LSLE (Table IV-2). The exception concerns the southern MS where organic nitrogen fluxes overpass those of nitrate. This result may be explained by the higher nitrate consumption by phytoplankton in the northern plateau. With  $k_p$  salinity-dependant, the lower nutrient uptake by phytoplankton leads to increased nitrate fluxes along all the transect that translate into higher ratios. The simulated nitrate concentrations were compared with *in situ* measurements coincident in space and time at two fixed stations located in the NWG, one offshore (Anticosti station) and another located along the Gaspé Peninsula (Gaspé station). The location of the stations is shown in Figure IV-8. The ratio between the integrated (0-30 m) simulated and *in situ* nitrate concentrations was used to evaluate the performance of the two model configurations (Figure IV-9ab). Simulated nitrate remain lower than *in situ* concentrations in both the Anticosti and Gaspé stations throughout the sampled dates when using a fixed  $k_p$ . In winter, when phytoplankton production is light limited, nitrate levels are comparable in both runs. During this season, the nitrate flux from the estuary is comparable in both runs. The model provides a fair estimate of *in situ* nitrate concentrations (ratio > 0.7) at both stations, except at the Gaspé station in January when initial conditions may affect solutions. In November, nitrate concentrations are closer to observations with a variable  $k_p$ . Similarly, nitrate concentrations in late June are in better agreement with the observations at both stations. However, at the Gaspé station, nitrate are strikingly overestimated (up to 5-folds) on June 3<sup>rd</sup> and September 16<sup>th</sup>. A similar pattern is encountered, but to a lesser extent, at the Anticosti station because of the clockwise circulation of the estuarine waters in this area

Table IV-2. Ratio of the yearly- and depth-integrated (0–30 m) nitrate flux over the yearly- and depth-integrated (0–30 m) organic nitrogen flux.

	LSLE	Northern MS	Southern MS	Cabot Strait
Fixed $k_p$	2.33	1.26	0.32	1.27
Variable $k_p$	7.57	3.10	1.44	2.11

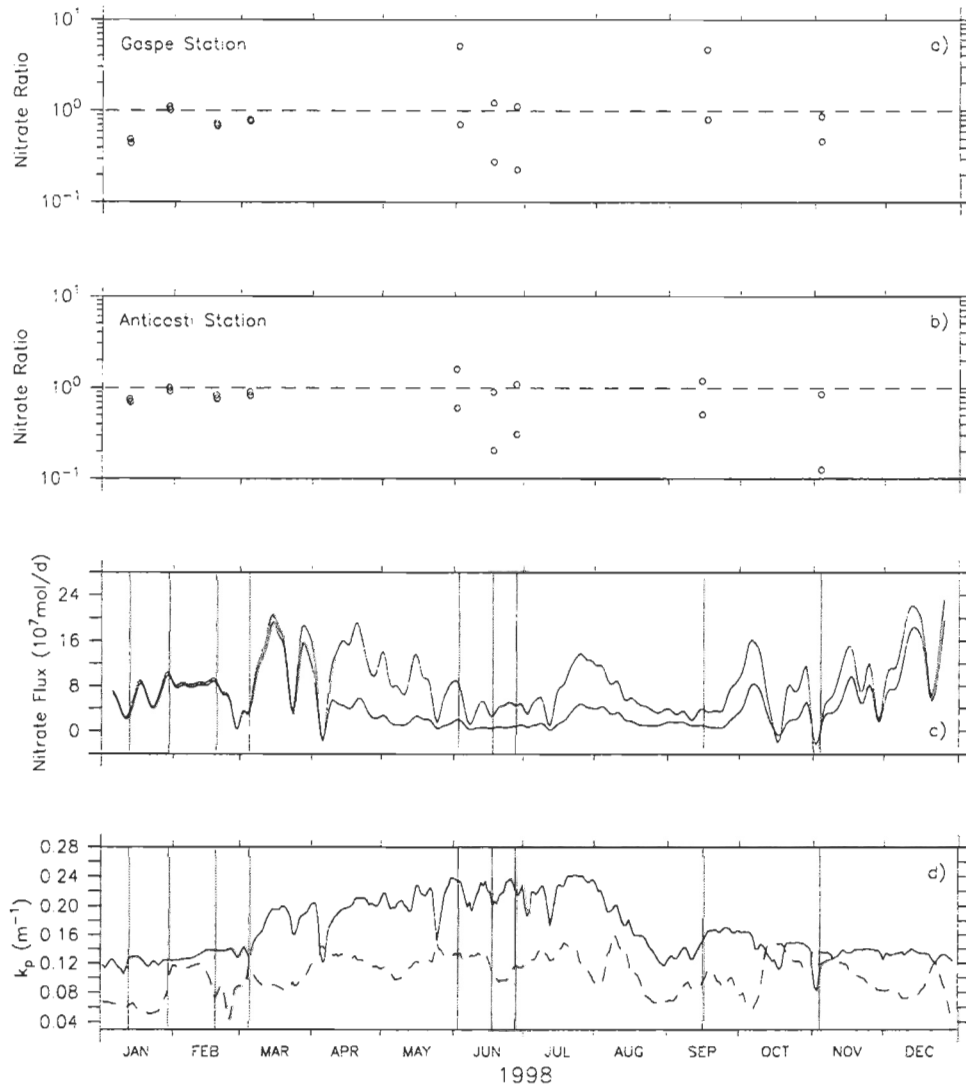


Figure IV-9. Ratios between simulated depth-integrated (0-30 m) vs *in situ* depth-integrated (0-30 m) nitrate concentrations at the a) Gaspé and b) Anticosti stations. The black and red circles correspond to the run using a fixed and variable  $k_p$ , respectively; time series of the c) depth-integrated (0-30 m) nitrate flux from the LSLE with a fixed  $k_p$  (in black) and variable  $k_p$  (in red) and d) depth-averaged (0-30 m)  $k_p$  at the Gaspé (black line) and Anticosti (black dashed line) stations.

(Figure IV-1). The larger discrepancies at the Gaspé station result in the fact the Gaspé Current is the preferential way for the outflow of the estuarine waters, as evidenced by the mean currents, salinity and  $k_p$  fields (see Figure IV-1). On June 3<sup>rd</sup>, the nitrate flux from the LSLE is 4-times higher with  $k_p$  salinity-dependant while it is only 2-times higher on September 16<sup>th</sup> (Figure IV-9c). However, the nitrate overestimation is comparable at both dates. This suggests that local circulation processes in this particularly highly dynamic area are probably involved on September 16<sup>th</sup>.

## DISCUSSION

As shown in Figure IV-6, light is a determining factor for the timing of the bloom in subregions impacted by the freshwater. In the LSLE, the bloom onset is thought to depend of both the freshwater-associated turbidity and runoff intensity [Therriault and Levasseur, 1985; Zakardjian *et al.*, 2000]. In 1998, the spring bloom in the LSLE is reported to occur in late May-early June [Starr *et al.*, 2002]. While a bloom is produced early in April when using a fixed value of  $k_p$ , due to a too much earlier exposure to favourable nutrient and light conditions, a better timing agreement is obtained with  $k_p$  salinity-dependant. The mean depth of the euphotic zone in the LSLE falls from 30 m to 15 m that is in better accordance with the reported maximum depth in the subregion [15-20 m; Therriault and Levasseur, 1985; Sime-Ngando *et al.*, 1995]. Despite the absence of sampling in May in the NWG, confidence may however be addressed to the simulated peak of Chl *a* since this region is directly under the influence of the estuarine waters.

In their modelling study, Savenkoff *et al.* [2001] have estimated mean summer (July-September) fluxes of inorganic nitrogen (0-30 m) through subregional GSL boxes. We performed similar estimations using the simulated nitrate concentrations from both runs and results are presented in Table IV-3. Since the authors used mean historical nitrate concentrations and currents fields from a 3-D diagnostic model [Han *et al.*, 1999], any direct comparison with our simulated fluxes is precluded. Nevertheless, which one of our two runs is the closest from these mean estimates can be evaluated. Overall, nitrate fluxes obtained with a variable  $k_p$  show lower differences (up to 54 %) with the values given by

Table IV-3. Mean nitrate flux (0-30 m) in summer (in  $10\text{mol s}^{-1}$ ). Percentages in parentheses indicate the bias between the fluxes simulated using a fixed or a salinity-dependant  $k_p$  and those provided by *Savenkoff et al.* [2001].

	LSLE	Upper MS	Lower MS	Cabot Strait
<i>Savenkoff et al.</i> [2001]	46	21	12	11
Fixed $k_p$	21.8 (-52.6 %)	2 (-90.4 %)	0.9 (-92.5 %)	1.6 (-85.4 %)
Variable $k_p$	70.8 (+53.9 %)	28.8 (+37.1 %)	10.6 (-11.6 %)	11 (0 %)

*Savenkoff et al.* [2001] comparatively to the run using a fixed  $k_p$  (52 % to 97 %). In this latter run, all nitrate fluxes are below those reported by *Savenkoff et al.* [2001] with the highest differences encountered in the MS and at Cabot Strait, where fluxes are approximatively one order of magnitude lower than the authors' estimates. By contrast, in the run using a variable  $k_p$ , fluxes are still lower (but closer) in the southern GSL but higher downstream in the LSLE and in the upper MS. An estimate of the mean flux of nitrate from the LSLE in June was estimated by *Sinclair et al.* [1976]. When compared to this estimate ( $39.7 \text{ } 10\text{mol s}^{-1}$ ), the simulated flux is also closer when using a variable  $k_p$  ( $50.1 \text{ } 10\text{mol s}^{-1}$  vs  $9.2 \text{ } 10\text{mol s}^{-1}$  with a fixed value of  $k_p$ ). While caution should be addressed because of the interannual variability that prevails in the GSL, particularly in the nitrate conditions [e.g., *Plourde and Therriault*, 2004], the use of a variable  $k_p$  permits however to get closer to the nitrate fluxes reported in the literature.

Higher  $k_p$  values in the estuarine plume translate into stronger light limitation, impacting thus the nitrate uptake by phytoplankton and primary production. The most impacted subregion is the LSLE, where annual primary production is reduced by 70 % ( $57.8 \text{ g C m}^{-2} \text{ yr}^{-1}$ ) between the two runs accounting only for half the estimate given by *Therriault and Levasseur* ( $103 \text{ g C m}^{-2} \text{ yr}^{-1}$ ; 1985). The underestimation of the simulated primary production finds support in the study of *Roy et al.* [1996]. While these authors report a mean primary production of about  $260 \text{ mg C m}^{-3} \text{ d}^{-1}$  between 0 and 20 m in the bloom period, simulated primary production only reaches  $34 \text{ mg C m}^{-3} \text{ d}^{-1}$  in the run using a variable  $k_p$ . In the LSLE, a strong tidal mixing greatly contributes to sustain primary production [*Le Fouest et al.*, 2005] but, when using a variable  $k_p$ , it also leads to higher

turbidity levels in deeper layers. Simulated algal biomass and primary production remain substantial but are considerably reduced (up to the half) when compared to the fixed  $k_p$  simulation. As a function of the simulated salinity, the present formulation of  $k_p$ , which mainly represents the terrestrial CDOM, involves conservativity in the turbidity. However, *Le Fouest et al.* [in revision, 2005], who compared SeaWiFS data with the corresponding simulated  $k_p$  and Chl *a* fields for the present year of simulation (1998), suggest that CDOM degradation may not be negligible in the GSL surface waters, especially in summer. Accounting for these degradation processes in the model is expected to diminish light limitation of phytoplankton but would probably not cause a substantial increase of the annual primary production.

The turbidity modelling through a function of salinity led to an apparent paradox, i.e., allowing a better bloom timing in the turbid waters and improved nitrate fluxes but strongly reducing primary production. Because of tides and freshwater runoff, the physical and bio-optical regime experienced by phytoplankton is quite different in the estuarine, coastal, and more oceanic waters of the GSL. By contrast with open ocean phytoplankton, coastal phytoplankton presents physiological abilities to photoacclimate to rapidly fluctuating light conditions [see *Strzepek and Harrisson, 2004*]. In highly dynamic and more turbid waters, algal cells are subject to hourly changes in light intensity and spectral quality that translate into short-term photosynthetic response [*McIntyre et al., 2000*]. In the Upper St. Lawrence Estuary, phytoplankton has been reported to be photoadapted to “intermittent sun” conditions maintaining high photosynthetic rates and low light limitation along a freshwater to turbid saltwater gradient [*Vincent et al., 1994*]. Despite this study has no equivalent in

the LSLE, phytoplankton is expected to be also exposed to high turbidity levels in this subregion. Hence it can be hypothesized that phytoplankton would be able to cope with such light conditions and maintain a certain photosynthetic capacity [e.g., *Roy et al.*, 1996] in nitrate-rich turbid waters. In the upper and lower estuary, phytoplankton has been suggested to be photoadapted to tidal mixing conditions [*Demers and Legendre*, 1981; *Legendre et al.*, 1985].

In order to improve the predictive ability of coupled physical-biological models in the complex coastal waters, new developments in modelling the phytoplankton response to the light field currently emerge. Growth rate formulations in biogeochemical models often use constant mean photosynthetic parameters. However, these values are known to be taxon-dependant [*McIntyre et al.*, 2000] but also to vary in space and time from diel to seasonal timescales [*Cullen et al.*, 1992]. To investigate this question, mechanistic models of cell physiology [e.g., *Flynn*, 2001] were developed. However, their relative complexity and numerical cost have to be considered before their implementation in already complex 3-D physical-biological coupled models, such as the use of simpler alternatives [e.g., *Ebenhöh et al.*, 1997]. Another approach consists to represent more accurately the underwater optical field experienced by phytoplankton through the estimation of variable attenuation coefficients. Methods employed to reach this purpose imply the assimilation in the model of remotely sensed and/or *in situ* data [*Ji et al.*, 2002; *Walsh et al.*, 2003; *Huret et al.*, 2005; *Le Fouest et al.*, in revision, 2005] or the explicit representation of optically active constituents [*Semovski*, 1999; *May et al.*, 2003]. In the GSL, it appears clearly that the phytoplankton response to variable light conditions is a key process for plankton dynamics

in the estuarine waters. Because of the large geographical extent of the turbid plume in the GSL and the need to predict as accurately as possible primary production in these waters, phytoplankton light utilization in the present coupled model would need further improvements. In regard to new developments in bio-optical and physiological modelling, a compromise supported by observations should be encountered for the St. Lawrence estuarine waters.

## CONCLUSIONS

Overall, better results were obtained with a salinity-dependant rather than with a fixed diffuse attenuation coefficient associated to nonchlorophyllous matter ( $k_p$ ). An improved representation of the spring bloom timing by the model was achieved in the Lower St. Lawrence Estuary whose dynamics is strongly influenced by the seasonal freshwater runoff. Moreover, simulated nitrate concentrations were found to be in better accordance with *in situ* measurements coincident in space and time at two fixed stations located in the passage of the seaward estuarine outflow. Nitrate fluxes in the surface layer were also more consistent with those reported in the literature.

As salinity-dependant, the  $k_p$  formulation in the model takes into account not only the effect of freshwater runoff but also that of sea ice melt and precipitations. The further use of a passive tracer would allow to avoid such a contribution of multiple factors. The suppressed primary production in the estuarine plume has highlighted the challenge that represents phytoplankton modelling in turbid and highly dynamic environments. In the estuary, a better understanding of how the system can support relatively high primary production rates in an euphotic zone generally no more than 20 m deep without impacting nitrate fluxes is required. The St. Lawrence showing a longitudinal gradient of water clarity from turbid to more oceanic, further knowledge about phytoplankton communities and their bio-optical characteristics would be helpful to go further in physical-biological modelling. Indeed, freshwater runoff and nitrate conditions being subject to a strong interannual variability, an adequate modelling of the phytoplankton response is a prerequisite in a

perspective of sea color data assimilation, operational biological oceanography and for the study of climatic change scenarios.

## V. CONCLUSION GÉNÉRALE

L'objectif général de la thèse visait à quantifier l'effet de la circulation à méso-échelle sur la dynamique de la production planctonique du Saint-Laurent à l'aide d'un modèle 3-D haute résolution couplé physique-biologique. A cette fin, trois objectifs spécifiques ont été fixés. Dans cette partie sont développées les principales conclusions qui répondent à chacun des ces objectifs spécifiques ainsi que les perspectives qui en découlent.

Le premier objectif spécifique (chapitre II) consistait à vérifier la robustesse écologique du modèle couplé physique-biologie à l'échelle régionale et à décrire qualitativement et quantitativement la variabilité sous-régionale du cycle saisonnier planctonique en réponse à des régimes hydrodynamique variés caractérisés par des méandres, des tourbillons, et des résurgences côtières. A cette fin, le premier modèle 3-D haute résolution couplé physique-biologie a été développé pour l'estuaire et le golfe du Saint-Laurent. Le choix d'un modèle modérément complexe d'écosystème planctonique a permis de simuler un cycle saisonnier canonique cohérent avec les observations rapportées dans le golfe [e.g., *Savenkoff et al.*, 2001]. En effet, le modèle produit un cycle annuel du phytoplancton caractérisé par une floraison printanière où dominent les grandes cellules algales, suivi en été par la formation d'un maximum profond de chlorophylle *a* et un régime de production primaire principalement régénérée. Plus tard dans la saison, l'apport de nitrate associé au mélange automnal mène à une augmentation de la proportion de la production nouvelle. Les rôles déterminants de la glace de mer dans le déclenchement de la floraison de printemps et de la circulation à méso-échelle sur le cycle planctonique et la

compétition entre les deux chaînes trophiques sont apparus clairement dans la simulation. Étant donné la richesse des conditions physiques et biologiques mise en évidence par le modèle couplé, le golfe du Saint-Laurent ne peut être considéré comme un système homogène. L'intensité de la floraison printanière étant similaire entre les sous-régions, la variabilité spatiale de la production primaire annuelle est due à des différences dans la production estivale associées à la variabilité à méso-échelle. Ceci suggère qu'en dehors de la période de floraison printanière, la production primaire soit localement du même ordre de grandeur que durant le printemps. En ce sens, la variabilité synoptique se compare en importance à la variabilité saisonnière. Ce premier chapitre a permis de mettre en évidence la capacité du modèle à reproduire un cycle saisonnier du plancton qualitativement et quantitativement cohérent mais aussi ses limites. Ces dernières incluent la formulation du champ de lumière, qui est apparue peu adaptée pour reproduire le cycle saisonnier du phytoplancton dans les eaux estuariennes plus turbides, ainsi que des processus impliqués dans la reminéralisation de l'azote organique dans la colonne d'eau et, finalement, l'utilisation de conditions stationnaires de nitrate et chlorophylle *a* aux frontières du domaine, principalement au détroits de Cabot et Belle-Isle.

Les concentrations de nitrate et de chlorophylle *a* simulées par le modèle ont été comparées avec succès avec des mesures *in situ* coïncidentes dans le temps et l'espace obtenues dans le cadre du Programme de Monitoring Zonal Atlantique (PMZA). Le modèle produit des valeurs proches des mesures *in situ* avec une variabilité comparable à celle des observations. Cependant, à la lumière de la variabilité synoptique générée par le modèle, il est apparu nécessaire de valider ces structures de méso-échelle. En effet, les mesures *in situ*

seules peuvent difficilement rendre compte de l'effet de la variabilité à méso-échelle sur la dynamique du phytoplancton, ce en quoi les données satellites contribuent par la haute résolution de leur couverture temporelle (jusqu'à quelques heures) et spatiale (jusqu'à un kilomètre). Le second objectif spécifique (chapitre III) était donc de valider les solutions du modèle couplé à l'échelle régionale et synoptique à l'aide de données satellites de température de surface (AVHRR) et de couleur de l'eau (SeaWiFS). Au regard des limites du modèle citées plus haut, une formulation empirique reliant le coefficient d'atténuation diffuse due au matériel non-chlorophyllien et la salinité du modèle a été incorporée afin d'améliorer le champ de lumière simulé. Cette relation permet ainsi de considérer l'effet de la turbidité associée aux eaux douces sur la dynamique planctonique. De plus, une climatologie saisonnière des champs de nitrate a été imposée aux détroits de Cabot et Belle-Isle. Concernant la température de surface, le modèle couplé et le radiomètre AVHRR ont tous deux donné une estimation comparable de la température *in situ* et montré des patrons spatiaux comparable à l'échelle régionale et sous-régionale. La comparaison des valeurs de chlorophylle *a* simulées et dérivées des mesures du senseur SeaWiFS avec des valeurs mesurées *in situ* coincidentes dans le temps et l'espace a révélé une surestimation substantielle par le senseur dans le panache estuarien, suggérant une contamination de ces valeurs par des composés optiques actifs (principalement de la matière organique colorée) présents dans l'eau. Toutefois, les patrons spatiaux dérivés du senseur SeaWiFS ont montré une bonne correspondance avec les champs simulés de turbidité (i.e., le coefficient d'atténuation diffuse due au matériel non-chlorophyllien) et ont ainsi permis de valider la variabilité saisonnière et synoptique de la circulation estuarienne.

Le chapitre III a permis de mettre en lumière l'étendue de la signature des eaux continentales, estuariennes en particulier, dans le golfe du Saint-Laurent. De ce résultat découle le troisième et dernier objectif spécifique qui visait à quantifier l'impact de la turbidité associée au panache estuarien sur la dynamique planctonique de l'estuaire et du golfe (chapitre IV). Comparativement à l'utilisation d'un coefficient constant d'atténuation diffuse due au matériel non-chlorophyllien, la fonction reliant ce coefficient à la salinité du modèle a permis de mieux simuler le déclenchement de la floraison printanière dans l'estuaire, où l'influence de l'écoulement des eaux douces est la plus marquée. De plus, les concentrations de nitrate simulées ont montré un meilleur accord avec les mesures *in situ* à deux stations fixes du nord-ouest du golfe fortement affectées par l'écoulement des eaux estuariennes. Les flux latéraux de nitrate dans la couche de surface ont été augmentés dans tout l'ouest du golfe pour se rapprocher des estimations rapportées dans la littérature. Toutefois, la réduction de la production primaire dans les sous-régions influencées par le panache estuarien a mis en évidence la nécessité d'améliorer la modélisation de la réponse du phytoplancton à des conditions fortement variables de lumière, processus clé dans la dynamique planctonique des eaux sous l'influence des eaux continentales. Au regard de flux latéraux de nitrate plus cohérents, un compromis devra être trouvé pour augmenter la production primaire sans réduire les flux de nitrate. Du fait de l'étendue du panache estuarien et de son influence sur la dynamique phytoplanctonique, la modélisation de la croissance du phytoplancton basée sur l'utilisation de la lumière devra être explorée. Dans le cas de l'estuaire maritime du Saint-Laurent, la question serait de comprendre comment une production primaire substantielle peut être assurée dans un milieu présentant une zone

euphotique dépassant rarement 15 m et soumis à un fort mélange sans réduire des flux latéraux de nitrate plus cohérents avec les observations. Au regard des nouveaux développements en modélisation bio-optique et physiologique, un compromis appuyé par des observations devra être trouvé pour les eaux du Saint-Laurent. Le runoff et les conditions de nitrate étant sujets à la variabilité inter-annuelle, une modélisation adéquate de la réponse du phytoplancton est un pré-requis pour l'étude des variations inter-annuelles et de scénarios de changements climatiques.

Cette étude de modélisation 3-D haute résolution du couplage physique-biologie a permis de mettre en évidence la richesse des processus de méso-échelle et l'importance de cette activité sur la dynamique planctonique en milieu côtier. Dans la Mer Baltique, le couplage d'un modèle d'écosystème planctonique simple (quatre compartiments) à un modèle de circulation haute résolution (1,8 km) a révélé le rôle clé de la circulation à méso-échelle sur la distribution du plancton [*Fennel et Neumann, 1996*] et a permis d'étudier les processus physiques impliqués [*Fennel, 2001*]. Dans ces deux cas, le choix d'une représentation simplifiée du modèle d'écosystème planctonique visait à faciliter l'interprétation de l'effet des processus physiques sur la dynamique planctonique. Le couplage réalisé durant cette thèse d'un modèle d'écosystème planctonique modérément complexe à un modèle de circulation haute résolution vient compléter cette approche en intégrant l'effet différentiel des processus de méso-échelle sur la dynamique des chaînes trophique. Il a été montré dans le chapitre II que l'enrichissement de la zone photique en nitrate associé à la circulation de méso-échelle favorisait la chaîne herbivore, résultat dont

les implications sont majeures pour les flux de carbone biogènes dans le Saint-Laurent. Cette thèse se place également en continuité de travaux récents menés en milieu côtier qui visent à coupler des modèles de circulation résolvant les processus à méso-échelle à des modèles d'écosystème planctonique incorporant différentes chaînes trophiques afin d'appréhender pleinement l'effet de cette circulation sur la production primaire [Holt *et al.*, 2004].

La forte variabilité mise en lumière par le modèle dans le Saint-Laurent devrait faire l'objet d'une attention particulière dans une perspective de prédire et d'évaluer les effets des changements climatiques sur la productivité des mers côtières des hautes latitudes. La circulation de densité dans le nord-ouest du golfe est influencée par les conditions hydrologiques et le régime des vents, et ainsi sujette aux variations inter-annuelles. Les résurgences d'eau côtière sont liées à la variabilité synoptique des vents (typiquement 3 à 9 jours dans l'est du Canada), mais leur fréquence et durée peuvent varier d'année en année. Considérant leur impact sur la productivité planctonique à l'échelle sous-régionale, la variabilité inter-annuelle des conditions hydrologiques et du régime des vents peut jouer un rôle significatif dans la variabilité inter-annuelle de la productivité planctonique dans le golfe. Les scénarios produits par les modèles atmosphériques suggèrent que les hautes et moyennes latitudes devraient être les plus affectées par le réchauffement global [Holland *et Bitz*, 2003]. Déjà, l'analyse de séries temporelles a révélé le lien étroit entre les variations du forçage climatique, la circulation des courants et les écosystèmes côtiers de l'océan Atlantique Nord-Ouest [Pershing *et al.*, 2001]. Les changements attendus du climat, en réponse à l'augmentation des concentrations atmosphériques des gaz à effet de serre,

devraient influencer la dynamique des écoulements océaniques de surface qui sont couplés avec les conditions atmosphériques. Ces changements hydrodynamiques sont susceptibles de modifier la productivité biologique de l'écosystème marin, en agissant sur les conditions physico-chimiques de la colonne d'eau (température, stratification, profondeur de la couche de mélange, apport en sels nutritifs). Cette thèse de doctorat s'intègre ainsi dans une stratégie à moyen terme qui vise à concevoir des outils numériques qui permettront d'examiner les effets des changements climatiques attendus sur la productivité marine à partir des scénarios définis par les modèles atmosphériques et océaniques. Connaissant la réponse de ces processus physiques de méso-échelle aux changements climatiques attendus, il sera alors possible d'évaluer les effets de ces changements sur la productivité des écosystèmes marins pélagiques [Eckman, 1994]. Ce modèle couplé physique-biologie pourra également être utilisé pour comprendre et prévoir les liens entre le climat, l'océan et la productivité planctonique de l'estuaire et du golfe du Saint-Laurent.

Ceci vient appuyer le besoin d'un programme intensif d'observation comme le Programme de Monitoring Zonal Atlantique (PMZA) qui, conjointement au modèle couplé, pourra permettre une meilleure compréhension de la variabilité inter-annuelle de la productivité planctonique. L'évaluation des performances des modèles 3-D couplés physique-biologie est une étape clé dans cette perspective d'études des variations inter-annuelles et de scénarios de changements climatiques. Au-delà de l'approche semi-quantitative, la plus couramment utilisée, le processus de validation tend vers une approche plus robuste qui vise à quantifier les différences entre les données simulées et observées, approche systématique des études de télédétection. Dans la Mer du Nord, Moll [2000] et

*Sjøiland et Skogen* [2000] ont usé de critères quantitatifs afin d'évaluer les résultats de deux modèles couplés à l'aide de bases de données (ICES et ERSEM). Toutefois, limités par la couverture spatiale et temporelle des observations, ces auteurs ont été contraints de comparer des climatologies mensuelles sur 10 ans et moyennées sur deux niveaux de profondeur. Dans l'océan ouvert, *Lima et Doney* [2004] ont quantifié les différences entre les patrons de distribution de climatologies mensuelles de chlorophylle *a* produits par un modèle global couplé physique-biologie et un set de données SeaWiFS pluri-annuel. Contrairement à l'étude de *Moll* [2000] et *Sjøiland et Skogen* [2000], le set de données SeaWiFS utilisé était plus complet mais non coïncidant avec la période simulée. Le Programme de Monitoring Zonal Atlantique, en couvrant la période 1997 à ce jour, offre une couverture spatiale et saisonnière inter-annuelle exceptionnelle de l'estuaire et du golfe du Saint-Laurent. Dans cette thèse, une partie de ces mesures *in situ* biogéochimiques et physiques ont été exploitées dans le but d'évaluer les performances de prédiction du modèle couplé pour 1997 et 1998. Les variables simulées ont été comparées systématiquement aux variables mesurées et dérivées de senseurs satellites coïncidentes dans le temps et l'espace et les différences entre le modèle et ces observations quantifiées. Le développement de l'outil de modélisation et la mise en place de procédures de validation systématique représenteraient une contribution majeure à l'océanographie biologique opérationnelle du Saint-Laurent.

L'information dérivée des mesures satellites s'est également avérée précieuse pour valider les champs simulés par le modèle couplé. Le senseur SeaWiFS, mais aussi de plus récents comme les senseurs MERIS et MODIS, fournit une information journalière à haute

résolution spatiale qui, complétée avec les mesures *in situ* du Programme de Monirotagage de Zonal Atlantique, pourrait permettre une validation plus précise des solutions du modèle dans le temps et dans l'espace. Afin d'exploiter pleinement cette information, une procédure de traitement des données de couleur de l'eau du senseur SeaWIFS adaptée aux eaux turbides de l'estuaire et du golfe du Saint-Laurent serait souhaitable pour une estimation précise de la concentration de chlorophylle *a* et de l'absorption de la matière organique dissoute colorée. Ces développements permettraient d'envisager l'assimilation de données de couleur de l'eau dans le modèle couplé pour améliorer sa capacité de prédiction en terme de production primaire. La mise au point d'un outil robuste associant télédétection, mesures *in situ* et modélisation 3-D couplée physique-biologie est nécessaire dans une perspective d'océanographie biologique opérationnelle dans le Saint-Laurent. Une validation plus fine des liens physique-biologie aux échelles synoptiques et saisonnières pourrait améliorer la fiabilité de la réponse du modèle aux scénarios de changements climatiques.

## VI. RÉFÉRENCES

- Anderson, T. R., Modelling the influence of food C:N ratio and respiration on growth and nitrogen excretion in marine zooplankton and bacteria, *J. Plankton. Res.*, *14*, 1645-1671, 1992.
- Babin, M., J.-C. Therriault, L. Legendre, and A. Condal, Variations in the specific absorption coefficient for natural phytoplankton assemblages: impact on estimates of primary production, *Limnol. Oceanogr.*, *38*, 154-177, 1993.
- Barreta, J. W., P. Ruardij, H. J. Vested, and J. G. Baretta-Bekker, Eutrophication modelling of the North Sea: two different approaches, *Ecol. Model.*, *75-76*, 471-483, 1994.
- Barron, C. N., A. B. Kara, H. E. Hurlburt, C. Rowley, and L. F. Smedstad, Sea surface height predictions from the global Navy Coastal Ocean Model during 1998-2001, *J. Atmos. Ocean. Technol.*, *21*, 1876-1893, 2004.
- Belyaev, K. P., D. Mueller, and C. Tanajura, Method for data assimilation in the hydrodynamical model and its application to the correction of the ocean condition, *Oceanology*, *45*, 23-36, 2005.
- Benoît, J., M. I. El-Sabh, and C. L. Tang, Structure and seasonal characteristics of the Gaspé Current, *J. Geophys. Res.*, *90*, 3225-3236, 1985.
- Berman, T., C. Bechemin, and S. Y. Maestrini, Release of ammonium and urea form dissolved organic nitrogen in aquatic ecosystems, *Aquat. Microb. Ecol.*, *16*, 295-302, 1999.

- Bernstein, R. L., Sea surface temperature estimation using the NOAA-6 advanced very high resolution radiometer, *J. Geophys. Res.*, 87, 9455-9465, 1982.
- Berthon, J. F., and G. Zibordi, Bio-optical relationships for the northern Adriatic Sea, *Int. J. Remote Sens.*, 25, 1527-1532, 2004.
- Binding, C. E., and D. G. Bowers, Measuring the salinity of the Clyde Sea from remotely sensed ocean color, *Estuar. Coast. Shelf Sci.*, 57, 605-611, 2003.
- Binding C. E., D. G. Bowers, and E. G. Mitchelson-Jacob, An algorithm for the retrieval of suspended sediment concentrations in the Irish Sea from SeaWiFS ocean colour satellite imagery, *Int. J. Remote Sens.*, 24, 3791-3806, 2003.
- Blough, N. V., and R. Del Vecchio, Chromophoric DOM in the coastal environment, in *Biogeochemistry of Marine Dissolved Organic Matter*, edited by D. A. Hansell and C. A. Carlson, Academic Press, Cambridge, MA, 509-546, 2002.
- Bourgault, D., and V. G. Koutitonsky, Real time monitoring of the freshwater discharge at the head of the St. Lawrence Estuary, *Atmos. Ocean*, 37, 203-220, 1999.
- Carder, K. L., R. G. Steward, G. R. Harvey, and P. B. Ortner, Marine humic and fulvic acids: their effects on remote sensing of ocean chlorophyll, *Limnol. Oceanogr.*, 34, 68-81, 1989.
- Carder, K. L., S. K. Hawes, K. A. Baker, R. C. Smith, R. G. Steward, and B. G. Mitchell, Reflectance model for quantifying chlorophyll *a* in the presence of productivity degradation products, *J. Geophys. Res.*, 96, 599-611, 1991.

- Caron, D. A., and J. C. Goldman, Protozoan nutrient regeneration, in *Ecology of marine protozoa*, edited by G. M. Capriulo, Oxford University Press, New York, 203-306, 1990.
- Chang, G., K. Mahoney, A. Briggs-Whitmire, D. D. R. Kohler, C. D. Mobley, M. Lewis, M. A. Moline, E. Boss, M. Kim, W. Philpot, and T. D. Dickey, The new age of hyperspectral oceanography, *Oceanogr.*, *17*, 16-23, 2004.
- Claereboudt, M. R., J. Cote, J. C. Bonardelli, and J. H. Himmelman, Seasonal variation in abundance and size structure of phytoplankton in Baie des Chaleurs, southwestern Gulf of St. Lawrence, in relation to physical oceanographic conditions, *Hydrobiol.*, *306*, 147-157, 1995.
- Claustre, H., P. Kerhervé, J. C. Marty, L. Prieur, C. Videau, and J. H. Hecq, Phytoplankton dynamics associated with a geostrophic front: ecological and biogeochemical implications, *J. Mar. Res.*, *52*, 711-742, 1994.
- Coble, P., C. Hu, R. W. Gould Jr., G. Chang, and A. M. Wood, Colored dissolved organic matter in the coastal ocean. An optical tool for coastal zone environmental assessment and management, *Oceanogr.*, *17*, 50-59, 2004.
- Crise, A., J. I. Allen, J. Baretta, G. Crispi, R. Mosetti, and C. Solidoro, The Mediterranean pelagic ecosystem response to physical forcing, *Prog. Oceanogr.*, *44*, 219-243, 1999.
- Cullen, J. J., M. R. Lewis, C. O. Davis, and R. T. Barber, Photosynthetic characteristics and estimated growth rates indicate grazing is the proximate control of primary production in the Equatorial Pacific, *J. Geophys. Res.*, *97*, 639-654, 1992.

- Daly, K. L., D. W. R. Wallace, W. O. Smith Jr., A. Skoog, R. Lara, M. Gosselin, E. Falck, and P. L. Yager, Non-Redfield carbon and nitrogen cycling in the Arctic: effects of ecosystem structure and dynamics, *J. Geophys. Res.*, *104*, 3185-3199, 1999.
- Dauchez, S., L. Legendre, L. Fortier, and M. Levasseur, Nitrate uptake by size-fractionated phytoplankton on the Scotian Shelf (Northwest Atlantic): spatial and temporal variability, *J. Plankton Res.*, *18*, 577-595, 1996.
- Darecki, M., and D. Stramski, An evaluation of MODIS and SeaWiFS bio-optical algorithms in the Baltic Sea, *Remote Sens. Env.*, *89*, 326-350, 2004.
- de Lafontaine, Y., M. I. El-Sabh, M. Sinclair, S. N. Messieh, and J.-D. Lambert, Structure océanographique et distribution spatio-temporelle d'oeufs et de larves de poissons dans l'estuaire maritime et la partie ouest du Golfe du Saint-Laurent, *Sciences et Techniques de l'Eau*, *17*, 43-50, 1984.
- de Lafontaine, Y., S. Demers, and J. A. Runge, Pelagic food-web interactions and productivity in the Gulf of St. Lawrence: a Perspective, in *The Gulf of St. Lawrence: small ocean or big estuary?*, edited by J. -C. Therriault, *Can. Spec. Publ. Fish. Aquat. Sci.*, *113*, 99-123, 1991.
- Demers, S., and L. Legendre, Mélange vertical et capacité photosynthétique du phytoplancton estuarien (estuaire du Saint-Laurent), *Mar. Biol.*, *64*, 243-250, 1981.
- Demers, S., L. Legendre, and J.-C. Therriault, Phytoplankton responses to vertical tidal mixing, in *Tidal mixing and plankton dynamics*, edited by J. Bowman, M. Yentsch, and W. T. Peterson, *Lectures notes on coastal and estuarine studies*, Springer-Verlag, Berlin Heidelberg, *17*, 1-40, 1986.

- Dickey, T. D., Studies of coastal ocean dynamics and processes using emerging optical technologies, *Oceanogr.*, *17*, 9-10, 2004.
- Di Lorenzo, E., A. J. Miller, D. J. Neilson, B. D. Cornuelle, and J. R. Moisan, Modelling observed California Current mesoscale eddies and the ecosystem response, *Int. J. Remote Sens.*, *25*, 1307-1312, 2004.
- Doney, S. C., I. Lima, K. Lindsay, K. Moore, S. Dutkiewicz, M. A. M. Friedrichs, and R. J. Matear, Marine biogeochemical modeling, *Oceanogr.*, *14*, 93-107, 2001.
- Doney, S. C., D. M. Glover, S. J. McCue, and M. Fuentes, Mesoscale variability of Sea-viewing Wide Field-of-view Sensor (SeaWiFS) satellite ocean color: global patterns and spatial scales, *J. Geophys. Res.*, *108*, Art. No. 3024, 2003.
- Dorch, Q., The interaction between ammonium and nitrate uptake in phytoplankton, *Mar. Ecol. Prog. Ser.*, *61*, 183-201, 1990.
- Doyon, P., B. Klein, R. G. Ingram, L. Legendre, J.-É Tremblay, and J.-C. Therriault, Influence of wind mixing and upper layer stratification on phytoplankton biomass in the Gulf of St. Lawrence, *Deep Sea Res., Part II*, *47*, 519-545, 2000.
- Drinkwater, K. F., G. C. Harding, W. P. Vass, and D. Gauthier, The relationship of Quebec lobster landings to freshwater runoff and wind storms, in The Gulf of St. Lawrence: small ocean or big estuary?, edited by J.- C. Therriault, *Can. Spec. Publ. Fish. Aquat. Sci.*, *113*, 179-187, 1991.
- D'Sa, E. J., and R. L. Miller, Bio-optical properties in waters influenced by the Mississippi River during low flow conditions, *Remote Sens. Env.*, *84*, 538-549, 2003.

- Dubinsky, Z., and I. Berman-Frank, Uncoupling primary production from populations growth in photosynthesizing organisms in aquatic ecosystems, *Aquat. Sci.*, *63*, 4-17, 2001.
- Ducklow, H. W., and M. J. R. Fasham, Bacteria in the greenhouse: modeling the role of oceanic plankton in the global carbon cycle, in *Environmental Microbiology*, edited by R. Mitchell, Wiley-Liss, New York, 1-31, 1992.
- Ebenhöh, W., J. Barreta-Bekker, and J. Barreta, The primary production module in the marine ecosystem model ERSEMII with emphasis on the light forcing, *J. Sea Res.*, *38*, 173-193, 1997.
- Eckman, J. E., Modelling physical-biological coupling in the ocean: the U.S. GLOBEC program, *Deep Sea Res.*, *41*, 1-5, 1994.
- Edwards, A. M., and J. Brindley, Zooplankton mortality and the dynamical behaviour of plankton population models, *Bull. Math. Biol.*, *61*, 303– 339, 1999.
- Edwards, A. M., and A. Yool, The role of higher predation in plankton population models, *J. Plankton Res.*, *22*, 1085-1112, 2000.
- Edwards, A. M., and M. A. Bees, Generic dynamics of a simple plankton population model with a non-integer exponent of closure, *Chaos, Solitons and Fractals*, *12*, 289-300, 2001.
- Eiane, K., D. L. Aksnes, M. D. Ohman, S. Wood, and M. B. Martinussen., Stage-specific mortality of *Calanus* spp. under different predation regimes, *Limnol. Oceanogr.*, *47*, 636-645, 2002.

- El-Sabh, M. I., Surface circulation patterns in the Gulf of St. Lawrence, *J. Fish. Res. Board Can.*, *33*, 124-138, 1976.
- Engel, A., S. Goldthwait, U. Passow, and A. Alldredge, Temporal decoupling of carbon and nitrogen dynamics in a mesocosm diatom bloom, *Limnol. Oceanogr.*, *47*, 753-761, 2002.
- Falkowski, P. G., and J. LaRoche, Acclimation to spectral irradiance in algae, *Limnol. Oceanogr.*, *27*, 8-14, 1991.
- Fasham, M. J. R., H. W. Ducklow, and S. M. McKenzie, A nitrogen-based model of plankton dynamics in the oceanic mixed layer, *J. Mar. Res.*, *48*, 591-639, 1990.
- Fennel, K., The generation of phytoplankton patchiness by mesoscale current patterns, *Ocean Dynam.*, *52*, 58-70, 2001.
- Fennel, W., and T. Neumann, The mesoscale variability of nutrients and plankton as seen in a coupled model, *German J. Hydrogr.*, *48*, 49-71, 1996.
- Ferrari, G. M., and M. D. Dowell, CDOM absorption characteristics with relation to fluorescence and salinity in coastal areas of the Southern Baltic Sea, *Estuar. Coast. Shelf Sci.*, *47*, 91-105, 1998.
- Flato, G. M., A particle-in-cell sea ice model, *Atmos. Ocean*, *31*, 229-358, 1993.
- Flynn, K. J., A mechanistic model for describing dynamic multi-nutrient, light, temperature interactions in phytoplankton, *J. Plankton Res.*, *23*, 977-997, 2001
- Forrester, W. D., Internal tides in the St. Lawrence Estuary, *J. Mar. Res.*, *32*, 55-66, 1974.

- Fortier, L., M. E. Levasseur, R. Drolet, and J.-C. Therriault, Export production and the distribution of fish larvae and their prey in a coastal jet frontal region, *Mar. Ecol. Prog. Ser.*, *85*, 203-218, 1992.
- Franks, P. J. S., J. S. Wroblewski, and G. R. Flierl, Behaviour of a simple plankton model with food-level acclimation by herbivores, *Mar. Biol.*, *91*, 121-129, 1986.
- Franks, P. J. S., NPZ models of plankton dynamics: their construction, coupling to physics, and application, *J. Oceanogr.*, *58*, 379-387, 2002.
- Friedrichs, M. A. M., Assimilation of JGOFS EqPac and SeaWIFS data into a marine ecosystem model of the central equatorial Pacific Ocean, *Deep Sea Res, Part II*, *49*, 289-319, 2002.
- Frost, B. W., Effects of size and concentration of food particles on the feeding behaviour of the marine planktonic copepod *Calanus pacificus*, *Limnol. Oceanogr.*, *17*, 805-815, 1972.
- Fuentes-Yaco, C., P. Larouche, A. F. Vézina, C. Vigneau, and M. Gosselin, Catalogue of phytoplankton pigment from the Gulf of St. Lawrence: Coastal Zone Color Scanner data from 1979 to 1980, *Can. Data Rep. Hydrogr. Ocean Sci.*, *135*, v + 91p., 1995.
- Fuentes-Yaco, C., A. F. Vézina, M. Gosselin, Y. Gratton, and P. Larouche, Influence of late-summer storms on the horizontal variability of phytoplankton pigment determined by Coastal Zone Color Scanner images in the Gulf of St. Lawrence, Canada, in *Ocean Optics XIII*, edited by S. G. Ackleson and R. Frouin, *Proc. SPIE*, Office of Naval Research, Arlington, VA, USA, 2963, 678-683, 1996.

- Fuentes-Yaco, C., A. F. Vézina, P. Larouche, C. Vigneau, M. Gosselin, and M. Levasseur, Phytoplankton pigment in the Gulf of St. Lawrence, Canada, as determined by the Coastal Zone Color Scanner-Part 1: spatio-temporal variability, *Cont. Shelf Res.*, *17*, 1421-1439, 1997a.
- Fuentes-Yaco, C., A. F. Vézina, P. Larouche, Y. Gratton, and M. Gosselin, Phytoplankton pigment in the Gulf of St. Lawrence, Canada, as determined by the Coastal Zone Color Scanner-Part 2: multivariate analysis, *Cont. Shelf Res.*, *17*, 1441-1459, 1997b.
- Gan, J., R. G. Ingram, R. J. Greatbatch, and T. Van der Baaren, Variability of circulation induced by the separation of the Gaspé Current in Baie des Chaleurs (Canada): observational studies, *Estuar. Coast. Shelf Sci.*, *61*, 393-402, 2004.
- Garcia-Gorrioz, E., N. Hoepffner, and M. Ouberdous, Assimilation of SeaWiFS data in a coupled physical-biological model of the Adriatic Sea. *J. Mar. Syst.*, *40-41*, 233-252, 2003.
- Garçon, V. C., A. Oschlies, S. C. Doney, D. J. McGillicuddy, and J. Waniek, The role of mesoscale variability on plankton dynamics in the North Atlantic; *Deep Sea Res., Part II*, *48*, 2199-2226, 2001.
- Gilbert, D., and B. Pettigrew, Current-meter data from Bonne-Bay, Newfoundland, during the summer of 1991, *Can. Data Rep. Hydrogr. Ocean Sci.*, *122*, v + 5pp., 1993.
- Gohin, F., J. N. Druon, and L. Lampert, A five channel chlorophyll concentration algorithm applied to SeaWiFS data processed by SeaDAS in coastal waters, *Int. J. Remote Sens.*, *23*, 1639-1661, 2002.

- Gower, J. F. R., SeaWiFS global composite images show significant features of Canadian waters for 1997–2001, *Can. J. Remote Sens.*, *30*, 26–35, 2004.
- Gowing, M. M., and M. W. Silver, Origins and microenvironments of bacteria mediating fecal pellet decomposition in the sea, *Mar. Biol.*, *73*, 7–16, 1983.
- Gratton, Y., G. Mertz, and J. A. Gagné, Satellite observations of tidal upwelling and mixing in the St. Lawrence Estuary, *J. Geophys. Res.*, *93*, 6947–6954, 1988.
- Gratton, Y., and A. F. Vézina, Variabilité des phénomènes physiques et biologiques à la méso-échelle dans l'estuaire maritime du Saint-Laurent. *Oceanis*, *20*, 45–57, 1994.
- Gregg, W. W., and N. W. Casey, Global and regional evaluation of the SeaWiFS chlorophyll data set, *Remote Sens. Env.*, *93*, 463–479, 2004.
- Grégoire, M., and J. M. Beckers, Modeling the nitrogen fluxes in the Black Sea using a 3D coupled hydrodynamical-biogeochemical model: transport versus biogeochemical processes, exchanges across the shelf break and comparison of the shelf and deep sea ecodynamics, *Biogeosciences Discussions*, *1*, 107–166, 2004.
- Greisman, P., and G. Ingram, Nutrient distribution in the St. Lawrence Estuary, *J. Fish. Res. Board Can.*, *34*, 2117:2123, 1977.
- Grossart, H.-P., and H. Ploug. Microbial degradation of organic carbon and nitrogen on diatom aggregates, *Limnol. Oceanogr.*, *46*, 267–277, 2001.
- Han, G., J. W. Loder, and P. C. Smith, Seasonal mean hydrography and circulation in the Gulf of St. Lawrence and on the Eastern Scotian and Southern Newfoundland Shelves, *J. Phys. Oceanogr.*, *29*, 1279–1301, 1999.

- Harding, L. W., A. Magnuson, and M. E. Mallonee, SeaWiFS retrievals of chlorophyll in Chesapeake Bay and the mid-Atlantic bight, *Estuar. Coast. Shelf Sci.*, 62, 75-94, 2005.
- Hargrave, B. T., G. C. Harding, K. F. Drinkwater, T. C. Lambert, and W. G. Harrison, Dynamics of the pelagic food web in St. Georges Bay, southern Gulf of St. Lawrence, *Mar. Ecol. Prog. Ser.*, 20, 221-240, 1985.
- Hitchcock, G. L., and T. J. Smayda, The importance of light in the initiation of the 1972-1973 winter-spring diatom bloom in Narragansett Bay, *Limnol. Oceanogr.*, 22, 126-131, 1977.
- Holland, M. M., and C. M. Bitz, Polar amplification of climate change in coupled models, *Clim. Dynam.*, 21, 221-232, 2003.
- Holligan, P. M., Balch, W. M., and C. M. Yentsch, The significance of subsurface chlorophyll, nitrite and ammonium maxima in relation to nitrogen for phytoplankton growth in stratified waters of the Gulf of Maine, *J. Mar. Res.*, 42, 1051-1073, 1984.
- Holt, J. T., R. Proctor, J. C. Blackford, J. I. Allen, and M. Ashworth, Advective controls on primary production in the stratified western Irish Sea: an eddy-resolving model study, *J. Geophys. Res.*, 109, 10.1029/2003JC001951, 2004.
- Hoteit, I., G. Triantafyllou, G. Petihakis, and J. I. Allen, A singular evolutive extended Kalman filter to assimilate real in situ data in a 1-D marine ecosystem model, *Ann. Geophys.*, 21, 389-397, 2003.
- Hunke, E. C., and J. K. Dukowicz, An elastic-viscous-plastic model for sea ice dynamics, *J. Phys. Oceanogr.*, 27, 1849-1867, 1997.

- Huret, M., I. Dadou, F. Dumas, P. Lazure, and V. Garçon, Coupling physical and biogeochemical processes in the Río de la Plata Plume, *Cont. Shelf Res.*, *25*, 629-653, 2005.
- Ibrahim, H., Y. George, and P. George, Towards a data assimilation system for the Cretan Sea ecosystem using a simplified Kalman filter, *J. Mar. Syst.*, *454*, 159-171, 2004.
- Ingram, R. G., and M. I. El-Sabh, Fronts and mesoscale features in the St. Lawrence Estuary, in *Oceanography of a Large-Scale Estuarine System: the St. Lawrence*, edited by M. I. El-Sabh and N. Silverberg, Springer-Verlag, New York, *39*, 71-93, 1990.
- Jacques, A., N. T. O'Neill, and J.-C. Therriault, Chlorophyll remote sensing potential in pigment-poor moderately turbid Case II waters: Lower St. Lawrence Estuary, *Can. J. Remote Sens.*, *24*, 194-199, 1998.
- Ji, R., C. Chen, J. W. Budd, D. J. Schwab, D. Beletsky, G. L. Fahnenstiel, T. H. Johegen, H. Vanderploeg, B. Eadie, J. Cotner, W. Gardner, and M. Bundy, Influences of suspended sediments on the ecosystem in Lake Michigan: a 3-D coupled bio-physical modeling experiment, *Ecol. Model.*, *152*, 169-190, 2002.
- Kahru, M., and B. G. Mitchell, Seasonal and nonseasonal variability of satellite-derived chlorophyll and colored dissolved organic matter concentrations in the California Current, *J. Geophys. Res.*, *106*, 2517-2529, 2001.
- Kamachi, M., T. Kuragano, S. Sugimoto, K. Yoshita, T. Sakurai, T. Nakano, N. Usui, and F. Uboldi, Short-range prediction experiments with operational data assimilation system for the Kuroshio south of Japan, *J. Oceanogr.*, *60*, 269-282, 2004.

- Keith, D. J., J. A. Yoder, and S. A. Freeman, Spatial and temporal distribution of coloured dissolved organic matter (CDOM) in Narragansett Bay, Rhode Island: implications for phytoplankton in coastal waters, *Estuar. Coast. Shelf Sci.*, 55, 705-717, 2002.
- Kiefer, D. A., and B. G. Mitchell, A simple steady state description of phytoplankton growth based on absorption cross section and quantum efficiency, *Limnol. Oceanogr.*, 28, 770-776, 1983.
- Kiorbøe, T., F. Mohlenberg, and K. Hamburger, Bioenergetics of the planktonic copepod *Acartia tonsa*: relation between feeding, egg production and respiration, and composition of specific dynamic action, *Mar. Ecol. Prog. Ser.*, 26, 85-97, 1985.
- Kiorbøe, T., Population regulation and role of mesozooplankton in shaping marine pelagic food webs, in *Eutrophication in Planktonic Ecosystems: Food Web Dynamics and Elemental Cycling*, edited by T. Tamminen and H. Kuosa, *Hydrobiol.*, 363, 13-27, 1998.
- Kirk, J. T. O., Light and photosynthesis in aquatic ecosystems, Cambridge University Press, Cambridge, 24-41, 1983.
- Kopelevich, O.V., V. I. Burenkov, S. V. Ershova, S. V. Sheberstov, and M. A. Evdoshenko, Application of SeaWiFS data for studying variability of bio-optical characteristics in the Barents, Black and Caspian Seas, *Deep Sea Res., Part II*, 51, 1063-1091, 2004.
- Korpinen, P., M. Kiirikki, J. Koponen, H. Peltoniemi, and J. Sarkkula, Evaluation and control of eutrophication in Helsinki sea area with the help of a nested 3D-ecohydrodynamic model, *J. Mar. Syst.*, 45, 255-265, 2004.

- Koski, M., M. Viitasalo, and H. Kuosa, Seasonal development of mesozooplankton biomass and production on the SW coast of Finland, *Ophelia*, 50, 69-91, 1999.
- Koutitonsky, V. G., and G. L. Budgen, The physical oceanography of the Gulf of St. Lawrence: a review with emphasis on the synoptic variability of the motion, in *The Gulf of St. Lawrence: small ocean or big estuary?*, edited by J.-C. Therriault, *Can. Spec. Publ. Fish. Aquat. Sci.*, 113, 57-90, 1991.
- Kowalczyk, P., Seasonal variability of yellow substances absorption in the surface layer of the Baltic Sea, *J. Geophys. Res.*, 104, 30047-30058, 1999.
- Kurapov, A. L., J. S. Allen, G. D. Egbert, R. N. Miller, P. M. Kosro, M. Devine, and T. Boyd, Distant effect of assimilation of moored currents into a model of coastal wind-driven circulation off Oregon, *J. Geophys. Res.*, 110, Art. No. C02022, 2005.
- Lacroix, J., Etude descriptive de la variabilité spatio-temporelle des phénomènes physiques de surface de l'estuaire maritime et de la partie nord-ouest du golfe du St. Laurent à l'aide d'images thermiques du satellite NOAA-7, M.Sc. Thesis, Université du Québec à Rimouski, Rimouski, Québec, 186 p., 1987.
- Lancelot, C., S. Becquevort, P. Menon, S. Mathot, and J.-M. Dandois, Ecological modelling of the planktonic microbial food-web, in *Belgian Research Program on the Antarctic. Scientific Results of Phase III (1992-1996): Marine Biogeochemistry and Ecodynamics*, edited by S. Caschetto, 1, 1-78, 1997.
- Lancelot, C., J. Staneva, D. Van Eeckhout, J. M. Beckers, and E., Stanev, Modelling the Danube-influenced northwestern continental shelf of the Black Sea: ecosystem

- response to changes in nutrient delivery by the Danube river after its damming in 1972, *Estuar. Coast. Shelf Sci.*, 54, 473-499, 2002.
- Larouche, P., SeaWIFS validation program in the St. Lawrence Estuary and Gulf, Fifth International Conference on Remote Sensing for Marine and Coastal Environments, San Diego, California, 5-7 October, 349-359, 1998.
- Larouche, P., Results from the 2<sup>nd</sup> St. Lawrence Estuary and Gulf SeaWIFS validation cruise, Sixth International Conference on Remote Sensing for Marine and Coastal Environments, Charleston, South Carolina, 1-3 May, 351-358, 2000.
- Lavender, S. J., M. H. Pinkerton, G. F. Moore, J. Aiken, and D. Blondeau-Patissier, Modification of the atmospheric correction of SeaWIFS ocean colour images over turbid waters, *Cont. Shelf Res.*, 25, 539-555, 2005.
- Lavoie, D., Y. Simard, and F. J. Saucier, Aggregation and dispersion of krill at channel heads and shelf edges: the dynamics in the Saguenay-St. Lawrence Marine Park, *Can. J. Fish. Aquat. Sci.*, 57, 1853-1869, 2000.
- Le Fouest V., M. Chifflet, M. Starr, B. Zakardjian, and F. J. Saucier, Toward prediction of the ecosystem: 3D simulations of the coupled planktonic production and hydrodynamics in the Gulf and Estuary of St. Lawrence, *AZMP Bull.*, 3, 37-41, <http://www.meds-sdmm.dfo-mpo.gc.ca/zmp/Documents/AZMP-No3.pdf>, 2003.
- Le Fouest, V., B. Zakardjian, F. J. Saucier, and M. Starr, Seasonal versus synoptic variability in planktonic production in a high-latitude marginal sea: the Gulf of St. Lawrence (Canada), *J. Geophys. Res.*, 2005, in press.

- Le Fouest, V., B. Zakardjian, F. J. Saucier, and S. A. Çizmeli, Application of remotely sensed sea color and temperature data for mesoscale and regional validation of a 3D high resolution biological-physical coupled model of the Gulf of St. Lawrence (Canada): the challenge of inland waters, *J. Mar. Syst.*, in revision, 2005.
- Legendre, L., and S. Demers, Auxiliary energy, ergoclines and aquatic biological production, *Nat. Can.*, 112, 5-14, 1985.
- Legendre, L., S. Demers, J.-C. Therriault, and C.-A. Boudreau, Tidal variations in the photosynthesis of estuarine phytoplankton isolated in a tank, *Mar. Biol.*, 88, 301-309, 1985.
- Legendre, L., and J. Le Fèvre, Microbial food webs and the export of biogenic carbon in oceans, *Aquat. Microb. Ecol.*, 9, 69-77, 1995.
- Legendre, L., and J. Michaud, Flux of biogenic carbon in oceans: size-dependent regulation by pelagic food webs, *Mar. Ecol. Prog. Ser.*, 164, 1-11, 1998.
- Legendre, L., and F. Rassoulzadegan, Stable versus unstable planktonic food webs in oceans, in *Microbial Biosystems: New Frontiers*, edited by C. R. Bell, M. Brylinsky, and P. Johnson-Green, Proceedings of the 8th International Symposium on Microbial Ecology, Atlantic Canada Society for Microbial Ecology, Halifax, Canada, 1999.
- Legendre, L., and R. B. Rivkin, Fluxes of carbon in the upper oceans: regulation by food-web control nodes, *Mar. Ecol. Prog. Ser.*, 242, 95-109, 2002.
- Lehrter, J. C., J. R. Pennock, and G. B. McManus, Microzooplankton grazing and nitrogen excretion across a surface estuarine-coastal interface, *Estuaries*, 22, 113-125, 1999.

- Le Traon, P. Y., Time scales of mesoscale variability and their relationship with spaces scales in the North Atlantic, *J. Mar. Res.*, *49*, 467-492, 1991.
- Levasseur, M., J.-C. Therriault, and L. Legendre, Hierarchical control of phytoplankton succession by physical factors, *Mar. Ecol. Prog. Ser.*, *19*, 211-222, 1984.
- Levasseur, M., and J.-C. Therriault, Phytoplankton biomass and nutrient dynamics in a tidally induced upwelling: the role of the NO<sub>3</sub>:SiO<sub>4</sub> ratio, *Mar. Ecol. Prog. Ser.*, *39*, 87-97, 1987.
- Levasseur, M., P. J. Harrison, B. R. Heimdal, and J.-C. Therriault, Simultaneous nitrogen and silicate deficiency of a phytoplankton community in a coastal jet-front, *Mar. Biol.*, *104*, 329-338, 1990.
- Levasseur, M., L. Fortier, J.-C. Therriault, and P. J. Harrison, Phytoplankton dynamics in a coastal jet frontal region, *Mar. Ecol. Prog. Ser.*, *86*, 283-295, 1992.
- Levinsen, H., and T. G. Nielsen, The trophic role of marine pelagic ciliates and heterotrophic dinoflagellates in Arctic and temperate coastal ecosystems: a cross-latitude comparison, *Limnol. Oceanogr.*, *47*, 427-439, 2002.
- Lévy, M., P. Klein, and A.-M. Treguier, Impact of sub-mesoscale physics on production and subduction of phytoplankton in an oligotrophic regime, *J. Mar. Res.*, *59*, 535-565, 2001.
- Lima, I. D., and S. C. Doney, A three-dimensional, multnutrient, and size-structured model for the North Atlantic, *Global Biogeochem. Cycles*, *18*, 10.1029/2003GB002146, 2004.

- Lohrenz, S. E., J. J. Cullen, D. A. Phinney, D. B. Olson, and C. S. Yentsch, Distribution of pigments and primary production in a Gulf Stream meander, *J. Geophys. Res.*, *98*, 14545-14560, 1993.
- Longhurst, A. R., and W. G. Harrison, The biological pump: Profiles of plankton production and consumption in the upper ocean, *Prog. Oceanogr.*, *22*, 47-123, 1989.
- Magnuson, A., L. W. Harding Jr., M. E. Mallonee, and J. E. Adolf, Bio-optical model for Chesapeake Bay and the Middle Atlantic Bight, *Estuar. Coast. Shelf Sci.*, *61*, 403-424, 2004.
- Mahadevan, A., and D. Archer, Modeling the impact of fronts and mesoscale circulation on nutrient supply and biogeochemistry of the upper ocean, *J. Geophys. Res.*, *105*, 1209-1225, 2000.
- Mahadevan, A., and J. W. Campbell, Biogeochemical patchiness at the sea surface, *Geophys. Res. Lett.*, *29*, Art. No. 1926, 2002.
- Maritorena, S., D. A. Siegel, and A. R. Peterson, Optimization of a semianalytical ocean color model for global-scale applications, *Appl. Opt.*, *41*, 2706-2714, 2002.
- Martin, A. P., and K. J. Richards, Mechanisms for vertical nutrient transport within a North Atlantic mesoscale eddy, *Deep Sea Res., Part II*, *48*, 757-773, 2001.
- Masina, S., P. Di Pietro, and A. Navarra, Interannual-to-decadal variability of the North Atlantic from an ocean data assimilation system, *Clim. Dynam.*, *23*, 531-546, 2004.

- May, C. L., J. R. Koseff, L. V. Lucas, J. E. Cloern, and D. H. Schoellhamer, Effects of spatial and temporal variability of turbidity on phytoplankton blooms, *Mar. Ecol. Progr. Ser.*, 254, 111-128, 2003.
- McClain, E. P., W. G. Pichel, and C. C. Walton, Comparative performance of AVHRR-based multichannel sea surface temperatures, *J. Geophys. Res.*, 90, 11587-11601, 1985.
- McGillicuddy, D. J., A. R. Robinson, D. A. Siegel, H. W. Jannasch, R. Johnson, T. D. Dickey, J. McNeil, A. F. Michaels, and A. H. Knap, Influence of mesoscale eddies on new production in the Sargasso Sea, *Nature*, 394, 263-266, 1998.
- McGillicuddy, D. J., The internal weather of the sea and its influences on ocean biogeochemistry, *Oceanogr.*, 14, 78-92, 2001.
- McGillicuddy, D. J., V. K. Kosnyrev, J. P. Ryan, and J. A. Yoder, Covariation of mesoscale ocean color and sea-surface temperature patterns in the Sargasso Sea, *Deep Sea Res., Part II*, 48, 1823-1836, 2001.
- McIntyre, H. L., T. M. Kana, and R. J. Geider, The effect of water motion on short-term rates of photosynthesis by marine phytoplankton, *Trends in Plant Science (Review)*, 5, 12-17, 2000.
- Mellor, G. L., and T. Yamada, A hierarchy of turbulence closure models for planetary boundary layers, *J. Atm. Sci.*, 31, 1971-1806, 1974.
- Mellor, G. L., and T. Yamada, Development of a turbulence closure model for geophysical fluid problems, *Rev. Geophys. Space Phys.*, 20, 851-875, 1982.

- Mertz, G., M. I. El-Sabh, D. Proulx, and A. R. Condal, Instability of a buoyancy-driven coastal jet: the Gaspé Current and its St. Lawrence precursor, *J. Geophys. Res.*, *93*, 6885-6894, 1988.
- Mertz G., M. I. El-Sabh, and V. G. Koutitonsky, Low-frequency variability in the lower St-Lawrence Estuary, *J. Mar. Res.*, *47*, 285-302, 1989.
- Mertz, G., and Y. Gratton, Topographic waves and topographically induced motions in the St. Lawrence Estuary, in *Oceanography of a large-scale system: the St. Lawrence*, edited by M. I. El-Sabh and N. Silverberg, Springer-Verlag, New York, *39*, 94-108, 1990.
- Mertz, G., V. G. Koutitonsky, and Y. Gratton, On the seasonal cycle of the Gaspé Current , in *The Gulf of St. Lawrence: small ocean or big estuary?*, edited by J. -C. Therriault, *Can. Spec. Publ. Fish. Aquat. Sci.*, *113*, 149-152, 1991.
- Mete Uz, B., and J. A. Yoder, High frequency and mesoscale variability in SeaWIFS chlorophyll imagery and its relation to other remotely sensed oceanographic variables, *Deep Sea Res., Part II*, *51*, 1001-1017, 2004.
- Molcard A., A. Griffa, and T. M. Ozgokmen, Lagrangian assimilation in multilayer primitive equation ocean model, *J. Atm. Ocean. Techn.*, *22*, 70-83, 2005.
- Moll, A., Assessment of three-dimensional physical-biological model ECOHAM1 simulations by quantified validation for the North Sea with ICES and ERSEM data, *ICES J. Mar. Sci.*, *57*, 1060-1068, 2000.

- Moran, M. A., W. M. Sheldon Jr., and R. G. Zepp, Carbon loss and optical property changes during long-term photochemical and biological degradation of estuarine dissolved organic matter, *Limnol. Oceanogr.*, *45*, 1254-1264, 2000.
- Morán, X. A. G., I. Taupier-Letage, E. Vázquez-Dominguez, S. Ruiz, L. Arin, P. Raimbault, and M. Estrada, Physical-biological coupling in the Algerian Basin (SW Mediterranean): Influence of mesoscale instabilities on the biomass and production of phytoplankton and bacterioplankton, *Deep Sea Res., Part I*, *48*, 405-437, 2001.
- Morel, A., Optical modeling of the upper ocean in relation to its biogenous matter content (case I waters), *J. Geophys. Res.*, *93*, 10749-10768, 1988.
- Mousseau, L., L. Legendre, and L. Fortier, Dynamics of size-fractionated phytoplankton and trophic pathways on the Scotian Shelf and at the shelf break, Northwest Atlantic, *Aquat. Microb. Ecol.*, *10*, 149-163, 1996.
- Muller-Karger, F. E., R. Varela, R. Thunell, R. Luerssen, C. Hu, and J. J. Walsh, The importance of continental margins in the global carbon cycle, *Geophys. Res. Lett.*, *32*, Art. No. L01602, 2005.
- Natvik, L.-J., and G. Evensen, Assimilation of ocean colour data into a biochemical model of the North Atlantic. Part 1. Data assimilation experiments, *J. Mar. Syst.*, *40-41*, 127-153, 2003.
- Neumann, T., Towards a 3D-ecosystem model of the Baltic Sea, *J. Mar. Syst.*, *25*, 405-419, 2000.
- Neumann, T., and G. Schernewski, An ecological model evaluation of two nutrient abatement strategies for the Baltic Sea, *J. Mar. Syst.*, *56*, 195-206, 2004.

- Nieke, B., R. Reuter, R. Heuermann, H. Wang, M. Babin, and J.-C. Therriault, Light absorption and fluorescence properties of chromophoric dissolved organic matter (CDOM) in the St. Lawrence Estuary (Case 2 waters), *Cont. Shelf Res.*, 17, 235-252, 1997.
- Oguz, T., A. G. Deshpande, and P. Malanotte-Rizzoli, The role of mesoscale processes controlling biological variability in the Black Sea coastal waters: inferences from SeaWiFS-derived surface chlorophyll field, *Cont. Shelf Res.*, 22, 1477-1492, 2002.
- Ohman, M. D., and J. A. Runge, Sustained fecundity when phytoplankton resources are in short supply: omnivory by *Calanus finmarchicus* in the Gulf of St. Lawrence, *Limnol. Oceanogr.*, 39, 21-36, 1994.
- Ohman, M. D., K. Eiane, E. G. Durbin, J. A. Runge, and H.-J. Hirche, A comparative study of *Calanus finmarchicus* mortality patterns at five localities in the North Atlantic, *ICES J. Mar. Sci.*, 61, 687-697, 2004.
- O'Neill, R. V., D. L. DeAngelis, J. J. Pastor, B. J. Jackson, and W. M. Post, Multiple nutrient limitations in ecological models, *Ecol. Model.*, 46, 147-163, 1989.
- O'Reilly, J. E., S. Maritorena, B. G. Mitchell, D. A. Siegel, K. L. Carder, S. A. Garver, M. Kahru, and C. R. McClain, Ocean color chlorophyll algorithm for SeaWiFS, *J. Geophys. Res.*, 103, 24937-24953, 1998.
- Oschlies, A., Model-derived estimates of new production: new results point towards lower values, *Deep Sea Res., Part II*, 48, 2173-2197, 2001.
- Packard, T., W. Chen, D. Blasco, C. Savenkoff, A. F. Vézina, R. C. Tian, L. St-Amand, S. Roy, C. Lovejoy, B. Klein, J.-C. Therriault, L. Legendre, and R. G. Ingram,

- Dissolved organic carbon in the Gulf of St. Lawrence, *Deep Sea Res., Part II*, 47, 435-459, 2001.
- Parsons, T. R., M. Takahashi, and B. Hargrave, Biological oceanographic processes, Pergamon Press, Oxford, 61-118, 1984.
- Pavelson, J., K. Kononen, and J. Laanemets, Chlorophyll distribution patchiness caused by hydrodynamical processes: a case study in the Baltic Sea, *ICES J. Mar. Sci.*, 56, 87-99, 1999.
- Pegau, W. S., E. Boss, and A. Martinez, Ocean color observations of eddies during the summer in the Gulf of California, *Geophys. Res. Lett.*, 29, 1295, 2002.
- Peinert, R., and J.-C. Miquel, The significance of frontal processes for vertical particle fluxes: a case study in the Alboran Sea (SW Mediterranean Sea), *J. Mar. Syst.*, 5, 377-389, 1994.
- Pershing, A. J., C. H. Greene, C. G. Hannah, D. Sameoto, E. Head, D. G. Mountain, J. W. Jossi, M. C. Benfield, P. C. Reid, and T. G. Durbin, Oceanographic responses to climate in the Northwest Atlantic, *Oceanogr.*, 14, 76-82, 2001.
- Petrie, B., B. Toulany, and C. Garrett, The transport of water, heat and salt through the Strait of Belle-Isle, *Atmos. Ocean*, 26, 234-251, 1988.
- Pingree, R. D., and D. K. Griffiths, A numerical model of the M2 tide in the Gulf of St. Lawrence, *Oceanolog. Acta*, 3, 221-225, 1980.
- Plourde, S., and J. A. Runge, Reproduction of the planktonic copepod *Calanus finmarchicus* in the Lower St. Lawrence Estuary: relation to the cycle of

- phytoplankton production and evidence for a *Calanus* pump, *Mar. Ecol. Progr. Ser.*, *102*, 217-227, 1993.
- Plourde, S., P. Joly, J. A. Runge, B. Zakardjian, and J. Dodson, Life cycle of *Calanus finmarchicus* in the Lower St. Lawrence Estuary: the imprint of circulation and late timing of the spring phytoplankton bloom, *Can. J. Fish. Aquat. Sci.*, *58*, 647-658, 2001.
- Plourde, J., and J.-C. Therriault, Climate variability and vertical advection of nitrate in the Gulf of St. Lawrence, Canada, *Mar. Ecol. Progr. Ser.*, *279*, 33-43, 2004.
- Pomeroy, L. R., and D. Deibel, Temperature regulation of bacterial activity during the spring bloom in Newfoundland coastal waters, *Science*, *233*, 359-361, 1986.
- Prieur, L., and L. Legendre, Oceanographic criteria for new phytoplankton production, in *Toward a Theory on Biological-Physical Interactions in the World Ocean*, edited by B. J. Rothschild, Kluwer Acad. Norwell, Mass., 71-112, 1988.
- Redfield, A. C., B. H. Ketchum, and F. A. Richards, The influence of organisms on the composition of sea water, in *The Sea, Ideas and Observations on Progress in the Study of the Seas*, edited by M. N. Hill, Wiley-Interscience, New York, 26-27, 1963.
- Ressler, P. H., and A. E. Jochens, Hydrographic and acoustic evidence for enhanced plankton stocks in a small cyclone in the northeastern Gulf of Mexico, *Cont. Shelf Res.*, *23*, 41-61, 2003.
- Richardson, K., J. Beardall, and J. A. Raven, Adaptation of unicellular algae to irradiance: an analysis of strategies, *New Phytol.*, *9*, 157-191, 1983.

- Riegman, R., B. R. Kuipers, A. A. M. Nooedeloos, and H. J. Witte, Size-differential control of phytoplankton and the structure of plankton communities, *Neth. J. Sea Res.*, *31*, 255-265, 1993.
- Rivkin, R. B., L. Legendre, D. Deibel, J.-É. Tremblay, B. Klein, K. Crocker, S. Roy, N. Silverberg, C. Lovejoy, F. Mesplé, N. Romero, M. R. Anderson, P. Matthews, C. Savenkoff, A. F. Vézina, J.-C. Therriault, J. Wesson, C. Bérubé, and R. G. Ingram, Vertical flux of biogenic carbon in the ocean: is there food web control?, *Science*, *272*, 1163-1166, 1996.
- Rodríguez, J., J. Tintoré, J. T. Allen, J. M. Blanco, D. Gomis, A. Reul, J. Ruiz, V. Rodríguez, F. Echevarria, and F. Jiménez-Gomez, Mesoscale vertical motion and the size structure of phytoplankton in the ocean, *Nature*, *410*, 360-363, 2001.
- Rose, G. A., and W. C. Leggett, Atmosphere-ocean coupling in the northern Gulf of St. Lawrence: frequency-dependant wind-forced variations in nearshore sea temperatures and currents, *Can. J. Fish. Aquat. Sci.*, *45*, 1222-1233, 1988.
- Roy, S., J.-P. Chanut, M. Gosselin, and T. Sime-Ngando, Characterization of phytoplankton communities in the lower St. Lawrence Estuary using HPLC-detected pigments and cell microscopy, *Mar. Ecol. Prog. Ser.*, *142*, 55-73, 1996.
- Roy, S., N. Silverberg, N. Romero, D. Deibel, B. Klein, C. Savenkoff, A. F. Vézina, J.-É. Tremblay, L. Legendre, and R. B. Rivkin, Importance of mesozooplankton feeding for the downward flux of biogenic carbon in the Gulf of St. Lawrence (Canada), *Deep Sea Res., Part II*, *47*, 519-545, 2000.

- Runge, J. A., and Y. Simard, Zooplankton of the St. Lawrence estuary: the imprint of physical processes on its composition and distribution, in *Oceanography of a large-scale system: the St. Lawrence*, edited by M. I. El-Sabh and N. Silverberg, Springer-Verlag, New York, 296-320, 1990.
- Runge, J. A., and Y. de Lafontaine, Characterization of the pelagic ecosystem in surface waters of the northern Gulf of St. Lawrence in early summer: the larval redfish-Calanus-microplankton interaction, *Fish. Oceanogr.*, 5, 21-37, 1996.
- Runge, J. A., M. Castonguay, Y. de Lafontaine, M. Ringuette, and J.-L. Beaulieu, Covariation in climate, zooplankton biomass and mackerel recruitment in the southern Gulf of St Lawrence, *Fish. Oceanogr.*, 8, 139-149, 1999.
- Runge, J. A., P. J. S. Franks, W. C. Gentleman, B. A. Megrey, K. A. Rose, F. E. Werner, and B. Zakardjian, Diagnosis and prediction in variability in secondary production and fish recruitment processes: developments in physical-biological modeling, In *The Sea*, Vol. 13, *The Global Coastal Ocean: Multi-Scale Interdisciplinary Processes*, edited by A. R. Robinson and K. Brink, Chap. 14, pp. 413-474, Harvard Univ. Press, Cambridge, Mass., 2005.
- Saíz, E., and M. Alcaraz, Enhanced excretion rates induced by small-scale turbulence in *Acartia* (Copepoda: Calanoida), *J. Plankton Res.*, 14, 681-689, 1992.
- Sambrotto, R. N., G. Savidge, C. Robinson, P. Boyd, T. Takahashi, D. M. Karl, C. Langdon, D. Chipman, J. Marra, and L. Codispoti, Elevated consumption of carbon relative to nitrogen in the surface ocean, *Nature*, 363, 248-250, 1993.

- Saucier, F. J., and J. Chassé, Tidal circulation and buoyancy effects in the St. Lawrence Estuary, *Atmos. Ocean*, *38*, 505-556, 2000.
- Saucier, F. J., F. Roy, D. Gilbert, P. Pellerin, and H. Ritchie, Modelling the formation and circulation processes of water masses and sea ice in the Gulf of St. Lawrence, Canada, *J. Geophys. Res.*, *108*, 1-20, 2003.
- Saucier, F. J., S. Senneville, S. Prinsenberg, F. Roy, P. Gachon, D. Caya, and R. Laprise, Modeling the ice-ocean seasonal cycle in Hudson Bay, Foxe Basin and Hudson Strait, Canada, *Clim. Dynam.* *23*, 303-326, 2004.
- Savenkoff, C., A. F. Vézina, Y. Gratton, D. Blasco, and J.-P. Chanut, Distribution of microplankton assemblages in relation to mesoscale variations in the Lower St. Lawrence Estuary (June-July 1990), *Can. Tech. Rep. Hydrogr. Ocean Sci.*, *197*: vii + 26 p, 1998.
- Savenkoff, C., A. F. Vézina, S. Roy, B. Klein, C. Lovejoy, J.-C. Therriault, L. Legendre, R. Rivkin, C. Bérubé, J.-É. Tremblay, and N. Silverberg, Export of biogenic carbon and structure and dynamics of the pelagic food web in the Gulf of St. Lawrence. Part 1. Seasonal Variations, *Deep Sea Res., Part II*, *47*, 585-607, 2000.
- Savenkoff, C., A. F. Vézina, P. C. Smith, and G. Han, Summer transports of nutrients in the Gulf of St. Lawrence estimated by inverse modelling, *Estuar. Coast. Shelf Sci.*, *52*, 565-587, 2001.
- Semovski, S. V., The Baltic Sea and Lake Baikal underwater bio-optical fields simulation using ecodynamical model, *Ecol. Model.*, *116*, 149-163, 1999.

- Semtner, A. J. Jr., A model for the thermodynamic growth of sea ice in numerical investigations of climate, *J. Phys. Oceanogr.*, *6*, 379-389, 1976.
- Sévigny, J. M., M. Sinclair, M. I. El-Sabh, S. Poulet, and A. Coote, Summer plankton distribution associated with the physical and nutrient properties on the northwestern Gulf of St. Lawrence, *J. Fish. Res. Board Can.*, *36*, 187-203, 1979.
- Sheng, J. Y., Dynamics of a buoyancy-driven coastal-jet: the Gaspé Current, *J. Physic. Oceanogr.*, *31*, 3146-3162, 2001.
- Siddorn, J. R., D. G. Bowers, and A. M. Hogue, Detecting the Zambezi River plume using observed optical properties, *Mar. Poll. Bul.*, *42*, 942-950, 2001.
- Siegel, D. A., D. J. McGillicuddy, and E. A. Fields, Mesoscale eddies, satellite altimetry, and new production in the Sargasso Sea, *J. Geophys. Res.*, *104*, 13359-13379, 1999.
- Simard, Y., and D. Lavoie, The rich krill aggregation of the Saguenay - St. Lawrence Marine Park: hydroacoustic and geostatistical biomass estimates, structure, variability, and significance for whales, *Can. J. Fish. Aquat. Sci.*, *56*, 1182-1197, 1999.
- Sime-Ngando, T., M. Gosselin, S. Roy, and J.-P. Chanut, Significance of planktonic ciliated protozoa in the Lower St. Lawrence Estuary: Comparison with bacterial, phytoplankton, and particulate organic carbon, *Mar. Ecol. Prog. Ser.*, *9*, 243-258, 1995.
- Sinclair, M., M. I. El-Sabh, and J.-R. Brindle, Seaward nutrient transport in the Lower St. Lawrence estuary, *J. Fish. Res. Bd. Can.*, *33*, 1271-1277, 1976.

- Sinclair, M., Summer phytoplankton variability in the lower St. Lawrence estuary, *J. Fish. Res. Board Can.*, *35*, 1171-1185, 1978.
- Skogen, M. D., and A. Moll, Interannual variability of the North Sea primary production: comparison from two model studies, *Cont. Shelf. Res.*, *20*, 129-151, 2000.
- Skogen, M. D., H. Sjøiland, and E. Svendsen, Effects of changing nutrient loads to the North Sea, *J. Mar. Syst.*, *46*, 23-38, 2004.
- Smayda, T. J., The suspension and sinking of phytoplankton in the sea, *Mar. Biol. Annu. Rev.*, *8*, 353-414, 1970.
- Sjøiland, H., and M. D. Skogen, Validation of a three-dimensional biophysical model using nutrient observations in the North Sea, *ICES J. Mar. Sci.*, *57*, 816-823, 2000.
- Spall, S. A., and K. J. Richards, A numerical model of mesoscale frontal instabilities and plankton dynamics - I. Model formulation and initial experiments, *Deep Sea Res., Part I*, *47*, 1261-1301, 2000.
- Starr, M., and M. Harvey, State of phytoplankton and zooplankton in the Estuary and northwestern Gulf of St. Lawrence during 1999, *DFO Science Stock Status Report*, C4-18, 2000.
- Starr, M., L. St-Amand, P. Joly, and J.-C. Therriault, Variations spatio-temporelles du phytoplankton dans l'estuaire maritime du Saint-Laurent, *AZMP Bull.*, *1*, 21-23, 2001.
- Starr, M., L. St-Amant, and L. Bérard-Therriault, State of phytoplankton in the Estuary and Gulf of St. Lawrence during 2001, Secretariat canadien de consultation scientifique, Document de recherche 2002/067, 2002.

- Steele, J. H., and E. W. Henderson, The role of predation in plankton models, *J. Plankton Res.*, *14*, 157-172, 1992.
- Stegmann, P. M., and D. S. Ullman, Variability in chlorophyll and sea surface temperature fronts in the Long Island Sound outflow region from satellite observations, *J. Geophys. Res.*, *109*, Art. No. C07S03, 2004.
- Steven, D. M., Primary and secondary primary production in the Gulf of St. Lawrence, McGill Univ. Mar. Sci. Centre MS Rep., 26, 116p, 1974.
- Strickland, J. D. H., Solar radiation penetrating the ocean. A review of the requirements, data and methods of measurement, with particular references to photosynthetic productivity, *J. Fish. Res. Bd. Can.*, *15*, 453-493, 1958.
- Strom, S. L., M. A. Brainard, J. L. Holmes, and M. B. Olson, Phytoplankton blooms are strongly impacted by microzooplankton grazing in coastal North Pacific waters, *Mar. Biol.*, *138*, 355-368, 2001.
- Strzepek, R. F., and P. J. Harrison, Photosynthetic architecture differs in coastal and oceanic diatoms, *Nature*, *431*, 689-692, 2004.
- Tamigneaux, E., M. Mingelbier, B. Klein, and L. Legendre, Grazing by protists and seasonal changes in the size structure of protozooplankton and phytoplankton in a temperate nearshore environment (western Gulf of St. Lawrence, Canada), *Mar. Ecol. Prog. Ser.*, *146*, 231-247, 1997.
- Tamigneaux, E., L. Legendre, B. Klein, and M. Mingelbier, Seasonal dynamics and potential fate of size-fractionated phytoplankton in a temperate nearshore

- environment (Western Gulf of St. Lawrence, Canada), *Estuar. Coast. Shelf Sci.*, *48*, 253-269, 1999.
- Tang, C. L., Mixing and circulation in the northwestern Gulf of St. Lawrence: a study of a buoyancy-driven current system, *J. Geophys. Res.*, *85*, 2787-2796, 1980a.
- Tang, C. L., Observation of wavelike motion of the Gaspé Current, *J. Phys. Oceanogr.*, *10*, 853-860, 1980b.
- Tassan, S., Local algorithms using SeaWiFS data for the retrieval of phytoplankton, pigments, suspended sediment, and yellow substances in coastal waters, *Appl. Opt.*, *33*, 2369-2378, 1994.
- Therriault, J.-C., and M. Levasseur, Control of phytoplankton production in the St. Lawrence Estuary: light and freshwater runoff, *Nat. Can.*, *112*, 77-96, 1985.
- Therriault, J.-C., and M. Levasseur, Freshwater runoff control of the spatio-temporal distribution of phytoplankton in the Lower St. Lawrence Estuary (Canada), in *The role of freshwater Outflow in Coastal marine Ecosystems*, edited by S. Skreslet, NATO ASI Ser. G7, 251-260, 1986.
- Therriault, J.-C., B. Petrie, J. Gagnon, D. Gregory, J. Helrig, A. Herman, D. Lefaivre, M. Mitchell, B. Pelchat, J. Runge, and D. Sameoto, Proposal for a Northwest Atlantic Zonal Monitoring Program, *Can. Tech. Rep. Hydrogr. Ocean Sci.*, *194*, 55 pp., 1998.
- Thibault, D., R. Gaudy, and J. Le Fèvre, Zooplankton biomass, feeding and metabolism in a geostrophic frontal area (Almeria-Oran Front, western Mediterranean). Significance to pelagic food webs, *J. Mar. Syst.*, *5*, 297-311, 1994.

- Thorndike, A. S., D. A. Rothrock, G. S. Maykut, and R. Colony, The thickness distribution of sea ice, *J. Geophys. Res.*, *80*, 4501-4513, 1975.
- Tian, R. C., A. F. Vézina, L. Legendre, R. G. Ingram, B. Klein, T. Packard, S. Roy, C. Savenkoff, N. Silverberg, J.-C. Therriault, and J.-É. Tremblay, Effects of pelagic food-web interactions and nutrient remineralization on the biogeochemical cycling of carbon: a modeling approach, *Deep Sea Res., Part II*, *47*, 637-662, 2000.
- Tian, R. C., A. F. Vézina, M. Starr, and F. J. Saucier, Seasonal dynamics of coastal ecosystems and export production at high latitudes: a modeling study, *Limnol. Oceanogr.*, *46*, 1845-1859, 2001.
- Toole, D. A., and D. A. Siegel, Modes and mechanisms of ocean color variability in the Santa Barbara Channel, *J. Geophys. Res.*, *106*, 26985-27000, 2001.
- Tremblay, J.-É., L. Legendre, and J.-C. Therriault, Size-fractionated effects of vertical stability on the biomass and production of phytoplankton in a large estuarine system, *Estuar. Coast. Shelf Sci.*, *45*, 415-431, 1997.
- Tremblay, J.-É., L. Legendre, B. Klein, and J.-C. Therriault, Size-differential uptake of nitrogen and carbon in a marginal sea (Gulf of St. Lawrence, Canada): significance of diel periodicity and urea uptake, *Deep Sea Res., Part II*, *47*, 489-518, 2000.
- Turner, J. T., Zooplankton fecal pellets, marine snow and sinking phytoplankton blooms, *Aquat. Microb. Ecol.*, *27*, 57-102, 2002.
- Vandevelde, T., L. Legendre, J.-C. Therriault, S. Demers, and A. Bah, Subsurface chlorophyll maximum and hydrodynamics of the water column, *J. Mar. Res.*, *45*, 377-396, 1987.

- Vézina, A. F., Y. Gratton, and P. Vinet, Mesoscale physical-biological variability during a summer phytoplankton bloom in the Lower St. Lawrence Estuary, *Estuar. Coast. Shelf Sci.*, *41*, 393-411, 1995.
- Vézina, A. F., C. Savenkoff, S. Roy, B. Klein, R. Rivkin, J.-C. Therriault, and L. Legendre, Export of biogenic carbon and structure and dynamics of the pelagic food web in the Gulf of St. Lawrence, Part 2. Inverse analysis, *Deep Sea Res., Part II*, *47*, 609-635, 2000.
- Vincent, W. F., N. Bertrand, and J.-J. Frenette, Photoadaptation to intermittent light across the St. Lawrence Estuary freshwater-saltwater transition zone, *Mar. Ecol. Progr. Ser.*, *110*, 283-292, 1994.
- Walsh, J. J., R. H. Weisberg, D. A. Dieterle, R. He, B. P. Darrow, J. K. Jolliff, K. M. Lester, G. A. Vargo, G. J. Kirkpatrick, K. A. Fanning, T. T. Sutton, A. E. Jochens, D. C. Biggs, B. Nababan, C. Hu, and F. E. Muller-Karger, phytoplankton response to intrusions of slope water on the West Florida Shelf: models and observations, *J. Geophys. Res.*, *108*, 10.1029/2002JC001406, 2003.
- Wang, J., and G. F. Cota, Remote-sensing reflectance in the Beaufort and Chukchi seas: observations and models, *Appl. Opt.*, *42*, 2754-276, 2003.
- Whitehead, R.F., de Mora, S., Demers, S., Gosselin, M., Monfort, P. and Mostajir, B., Interactions of ultraviolet-B radiation, mixing, and biological activity on photobleaching of natural chromophoric dissolved organic matter: a mesocosm study, *Limnol. Oceanogr.*, *45*, 278-291, 2000.

- Wiggert, J., T. Dickey, and T. Granata, The effect of temporal undersampling on primary production estimates, *J. Geophys. Res.*, *99*, 3361-3371, 1994.
- Williams, R. G., and M. J. Follows, The Ekman transfer of nutrients and maintenance of new production over the North Atlantic, *Deep Sea Res., Part I*, *45*, 461-489, 1998.
- Woods, J., Scale upwelling and primary production, in *Toward a Theory on Biological-Physical Interactions in the World Ocean*, edited by B. J. Rothschild, Kluwer Acad. Norwell, Mass., 7-38, 1988.
- Wozniak, S. B., and D. Stramski, Modeling the optical properties of mineral particles suspended in seawater and their influence on ocean reflectance and chlorophyll estimation from remote sensing algorithms, *Appl. Opt.*, *43*, 3489-3503, 2004.
- Yeats, P. A., Reactivity and transport of nutrients and metals in the St. Lawrence Estuary, in *Oceanography of a Large-scale Estuarine System: the St. Lawrence*, edited by M. I. El-Sabh and N. Silverberg, Springer-Verlag, New York, 155-165, 1990.
- Zakardjian, B., and L. Prieur, A numerical study of primary production related to vertical turbulent diffusion with special reference to vertical motions of the phytoplankton cells in nutrient and light fields, *J. Mar. Syst.*, *5*, 267-295, 1994.
- Zakardjian, B., and L. Prieur, Biological and chemical signs of upward motions in permanent geostrophic fronts of the Western Mediterranean, *J. Geophys. Res.*, *103*, 27849-27866, 1998.
- Zakardjian, B., Y. Gratton, and A. F. Vézina, Late spring phytoplankton bloom in the Lower St. Lawrence Estuary: the flushing hypothesis revisited, *Mar. Ecol. Prog. Ser.*, *192*, 31-48, 2000.

Zakardjian, B., J. Sheng, J. A. Runge, I. McLaren, S. Plourde, K. R. Thompson, and Y. Gratton, Effect of temperature and circulation on the population dynamics of *Calanus finmarchicus* in the Gulf of St. Lawrence and Scotian Shelf: study with a coupled, three-dimensional hydrodynamic, stage-based life history model, *J. Geophys. Res.*, *108*, 8016, 2003.